# MSc thesis

## Turbulent drag reduction through spanwise wall oscillation

L. Bermel

**An experimental investigation by tomographic PIV**

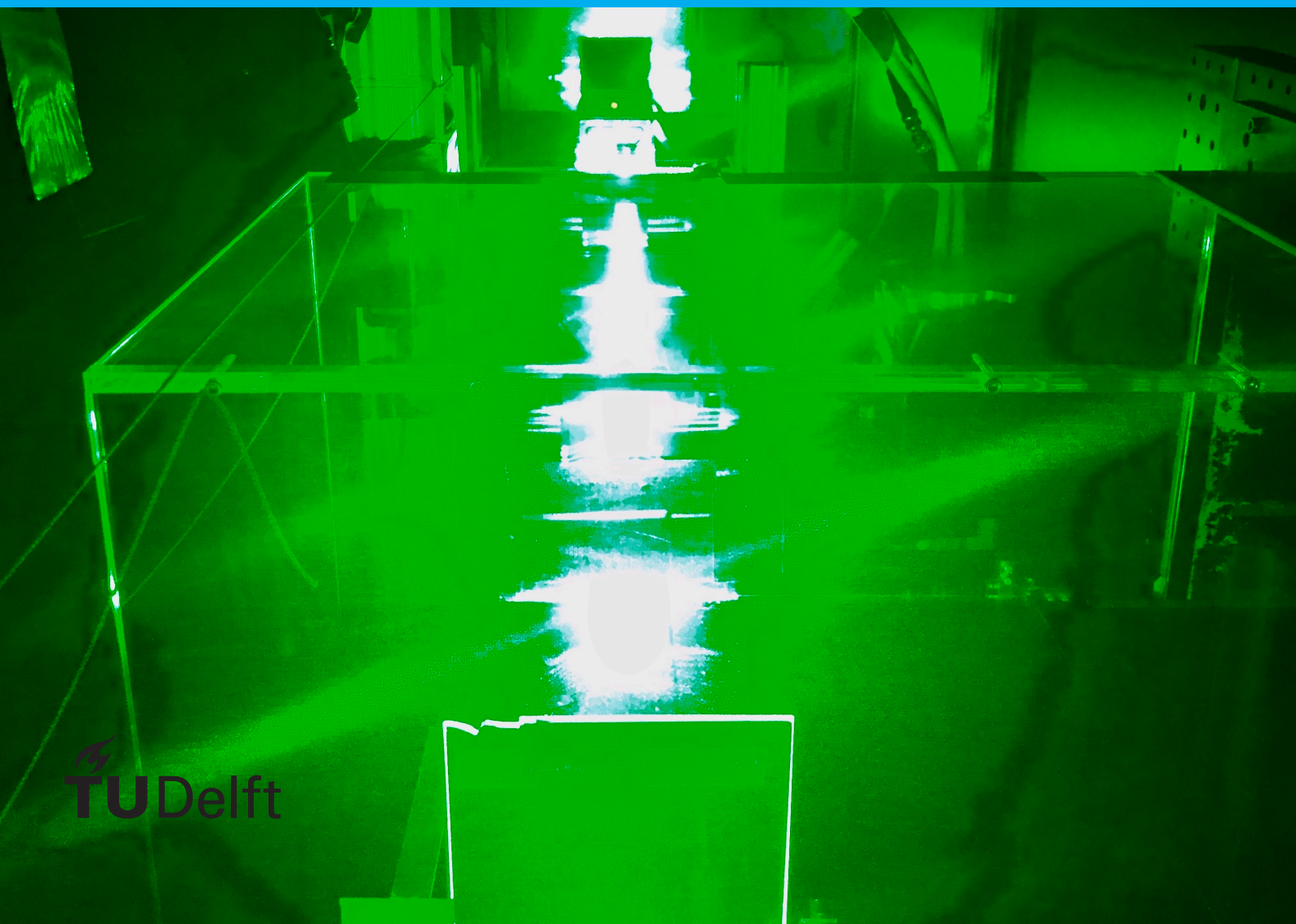

TU Delft

# MSc thesis

## Turbulent drag reduction through spanwise wall oscillation

by

L. Bermel

to obtain the degree of Master of Science
at the Delft University of Technology.
to be defended publicly on Thursday August 20, 2020 at 10:00 am.

Student number: 4278739
Supervisors: Prof. dr. F. Scarano
K. U. Kempaiah



TU Delft

# Preface

The document you are holding in your hands concludes my studies in Aerospace Engineering at TU Delft. I came across many inspiring and multicultural people in six years at TU Delft and tried to learn from everyone's skill set to improve my own. Many friends such as Thiemo Grimme, Yannick Bunk and Elias Matteo Fernandez have left Delft, others such as Carlo Alberto Socci and Lukas Mueller are still there. I am grateful for the support among each other and I am looking forward to keep up the friendships wherever our paths will lead.

Furthermore, I would like to thank Prof. F. Scarano and Kushal Kempaiah for the very interesting and exciting MSc thesis topic. Your support and commitment along the way was impressive and I felt like having true mentors. This personal commitment can not be appreciated highly enough and is not to be found everywhere in our modern society. Also in times of COVID-19 you have proven much flexibility in terms of online meetings, adapting our experiment schedule to the situation at hand and never forgot the soft and social skills in this process. At this point I would also like to thank my wonderful family which was confronted with me being full time at home again after a couple of years, posing quite a challenge for everyone. However, their support was unbroken which made completing the thesis a valuable experience even under special circumstances .

Finally, I would like to thank Lukas Mueller, Carlo Alberto Socci and Kushal Kempaiah for many feedback rounds and proof-reading, as I know its not easy to make room for voluntary aid in your full agendas. I deeply desire to stay in the network of all the people mentioned in the preface and look forward to future crossing points.

*L. Bermel*
*Delft, August 2020*

# Abstract

Turbulent boundary layers are responsible for up to 89 % of the skin friction drag of civil aircraft. This shows that in regard to the current social sensitivity towards climate friendly aviation a reduction of turbulent skin friction could have a large impact. On the one side greenhouse gas emissions by aviation could be reduced and on the other hand fuel costs could be saved, an important consideration for airlines. The research on turbulent drag reduction distinguishes between passive and active techniques. Passive techniques have the advantage that no energy input is necessary. Prominent examples are riblets and dimples which have shown turbulent drag reductions up to 10 %. Active techniques reach turbulent drag reduction percentages of up to 45 %, however it is in doubt if the energy savings are larger than the energy required to operate the control technique. One promising active technique which has proven to partially generate a positive energy effect is spanwise wall oscillation. However, researchers have opposing opinions of the mechanism which leads to the drag reduction. As turbulent boundary layers are strongly three-dimensional, the work of this thesis investigates three-dimensional flow fields of turbulent boundary layers subjected to spanwise wall oscillation by means of tomographic PIV. These are used to study the changes in pointwise statistics and coherent structures in order to derive a descriptive model of the drag reducing mechanism.

# Contents

# List of Figures

# List of Tables

# Symbols

| | |
|---|---|
| $A$ | Oscillating wave amplitude |
| $A^+$ | Dimensionless oscillating wave amplitude |
| $c_f$ | Skin friction coefficient |
| $D$ | Flat plate drag without riblets |
| $D_s$ | Flat plate drag with riblets |
| $dz$ | Focal depth of camera |
| $f_{acq}$ | Acquisition frequency of the PIV system |
| $f_{osc}$ | Oscillation frequency of the plate wave motion |
| $f^+$ | Dimensionless plate oscillation frequency |
| $f_\#$ | Camera f - stop |
| $F^d_{u'}$ | Detection function for low and high-speed streaks |
| $F^d_{u'v'}$ | Detection function for sweep and ejections |
| $h$ | Channel half width |
| $I$ | Illumination intensity |
| $k$ | Turbulent kinetic energy |
| $M$ | Magnification factor |
| $N$ | Number of samples |
| $p_e$ | External pressure |
| $P_k$ | Turbulent kinetic energy production term |
| $Q_x$ | Streamwise flow rate |
| $Re_b$ | Reynolds number based on two times the bulk velocity and $\delta_{99}$ |
| $Re_c$ | Reynolds number based on $U_e$ and LEBU chord |
| $Re_{crit}$ | Critical Reynolds number at which a laminar boundary layer becomes unstable |
| $Re_{trans}$ | Reynolds number at which a laminar boundary layer turns turbulent |
| $Re_L$ | Reynolds number based on $U_e$ and flat plate lenght |
| $Re_{\delta^*}$ | Reynolds number based on $U_e$ and $\delta^*$ |
| $Re_{\delta_{99}}$ | Reynolds number based on $U_e$ and $\delta_{99}$ |
| $Re_\theta$ | Reynolds number based on $\theta$ and $U_e$ |
| $Re_{ij}$ | Reynolds stress of component i and j |
| $s^+$ | Dimensionless riblet spacing |
| $t$ | time |
| $T$ | period of a sine function |
| $T^+$ | dimensionless period of a sine function |
| $\mathbf{U}$ | Cartesian velocity vector (u, v, w) |
| $U_e$ | External flow velocity |
| $u$ | Streamwise velocity |
| $u'$ | streamwise velocity fluctuations |
| $\overline{u}$ | mean streamwise velocity |
| $u^+$ | non-dimensional streamwise velocity |
| $u_\tau$ | Friction velocity |
| $v$ | Wall-nomral velocity |
| $v'$ | wall-normal velocity fluctuations |
| $\overline{v}$ | mean wall-normal velocity |
| $w$ | Spanwise velocity |
| $\overline{w}$ | mean spanwise velocity |
| $w'$ | spanwise velocity fluctuations |

| | |
|---|---|
| $w_{wall}$ | Oscillating wall spanwise velocity |
| $x$ | Streamwise direction |
| $y$ | Wall-nomral direction |
| $y^+$ | non-dimensional wall-normal coordinate |
| $z$ | spanwise direction |
| $\epsilon$ | error |
| $\mu$ | dynamic fluid viscosity |
| $\nu$ | kinematic fluid viscosity |
| $\omega$ | angular frequency of the plate wave motion |
| $\delta_{99}$ | boundary layer thickness |
| $\tau_w$ | wall shear stress |
| $\delta^*$ | boundary layer displacement thickness |
| $\theta$ | boundary momentum thickness |
| $\rho$ | fluid density |
| $\Theta$ | Scheimpflug angle |

# Nomenclature

| | |
|---|---|
| **DBD** | Dielectric barrier discharge |
| **DNS** | Direct numerical simulation |
| **EAP** | Electroactive polymers |
| **FIK** | Fukagata, Iwamoto & Kasagi |
| **LEBU** | Large eddy break up device |
| **PS** | Power saving |
| **RMS** | Root mean square |
| **TBL** | Turbulent boundary layer |
| **TCF** | Turbulent channel flow |
| **TDR** | Turbulent drag reduction |
| **TKE** | Turbulent kinetic energy |
| **ZPGTBL** | Zero pressure gradient turbulent boundary layer |

# 1 Introduction

As early as in 1930 the American inventor Thomas Edison (founder of General Electric) raised his voice to express concerns about the exhaustive use of fossil fuels by human beings (West, 2000). It took 67 years until these initial concerns of Thomas Edison received serious attention in international politics in form of the Kyoto Protocol. It was adopted in 1997 and contains greenhouse emission targets for developed countries which are legally binding. EU countries agreed on 20 % emission reduction with respect to 1990 until 2020 (Federal Foreign Office of Germany, 2020). In the year 2015 the Paris Agreement was initiated which aimed to keep the global warming below 2°. Participating countries represent 55 % of the global greenhouse gas emissions (European Council, 2018). As it is in doubt that the goals agreed upon in these international commitments will be met, there are groups of environmental activists forming such as the *Fridays for Future* and the *Extinction Rebellion* movement. This shows that the topic is not only of political nature but holds relevance for society as well. The development of air traffic is widely regraded as a risk for avoiding excessive climate change. Air traffic approximately tenfolded in passenger numbers and freight load as shown in fig. 1.1 from 1970 to 2018. In total, the carbon dioxide emissions of the aviation sector were 895 million tons making up 2 % of the total global emissions in 2018 (EU Council, 2012 and ATAG, 2018).

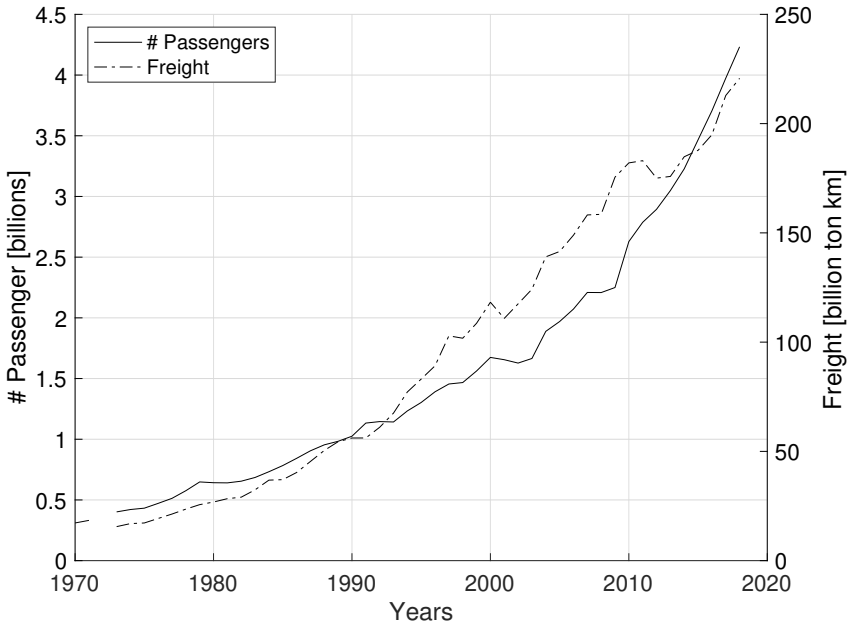


Figure 1.1: Development of air traffic from 1970 to 2018 (The World Bank, 2019)

TU Delft is leading several research activities in the field of sustainable aviation. Some of the main topics are the development of the blended wing body aeroplane (flying V) and research in the field of flow stability & control (Innovation Quarter, 2020 and TU Delft, 2020). The topic of this report is part of the flow stability & control field as it aims to control turbulent boundary layers (TBL) to reduce their skin friction. If the economic relevance of turbulent skin friction is considered, it is interesting to look at the direct operating cost of an aeroplane in fig. 1.2. It shows that fuel cost makes up 22 % of the total operating cost. Fuel consumption of an aeroplane scales with its drag as the main component of the generated thrust is to overcome aeroplane drag. Therefore, turbulent drag reduction (TDR) generates a saving potential for airlines that is pointed out here in terms of fuel costs.

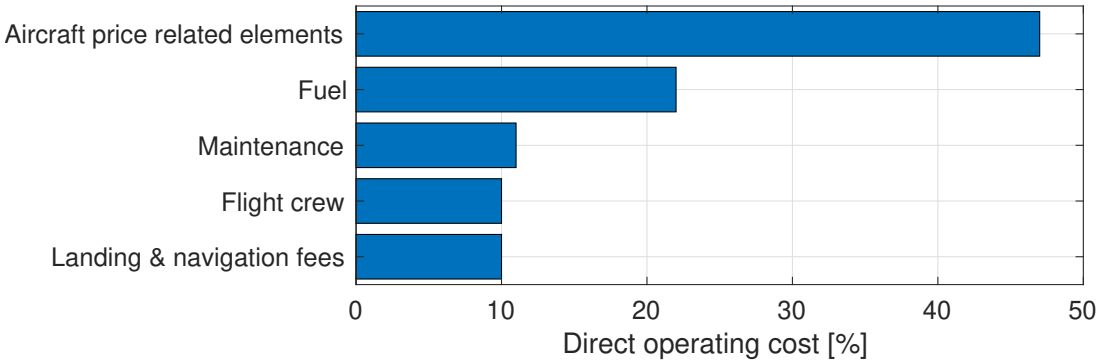


Figure 1.2: Direct operation cost of a typical civil aviation aeroplane (Marec, 2000)

To assess the TDR potential of an aeroplane by turbulent skin friction reduction, fig. 1.3 provides a drag breakdown of a typical civil aeroplane. It shows that the friction drag almost makes up 50 % of the aeroplane's total drag. One must be aware, that the skin friction arises from both, laminar and turbulent sections of boundary layers, however the turbulent contribution is predominant (Albers et al., 2017). Dimple-Technologies gives a ratio between laminar and turbulent skin friction as approximately 1:8 (Dimple Technologies (2020)). Thus, a successful installed TDR mechanism on an aeroplane can result into a total drag reduction of up to 41.8 % in the most optimistic case. The reduction potential is also indicated in fig. 1.3 in the green box.

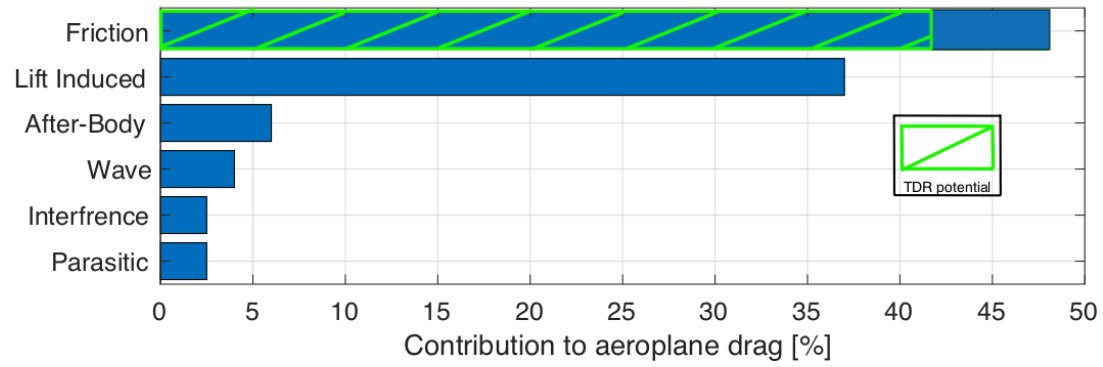


Figure 1.3: Drag breakdown of a typical civil aviation aeroplane (Marec, 2000)

The development of air traffic and fuel burn through aviation has shown to have an impact on the global environmental crisis. One lever which can contribute to attenuate this impact is TDR. A detailed study of TBLs reveals that coherent structures such as streaks, hairpins and ejections/sweeps play a vital role in the process of turbulent skin friction generation as presented in chapter 2. Many attempts have been undertaken in past research to find techniques which manipulate these structures in TBLs such that TDR is reduced. A compact overview of the most promising techniques is given in chapter 3. The review of them shows that the techniques differ in practical feasibility and TDR potential. TDR by spanwise wall oscillation is regarded as one of the most prominent techniques. Therefore chapter 4 is

entirely devoted to it.

The ensemble of spanwise wall oscillation research shows that 2D pointwise statistics are well understood, however little is known about the coherent structure dynamics which lead to TDR. Proof for this are the dissimilar hypotheses of prominent researches such as in the work of Arturo and Quadrio (1995) and Choi et al. (1998). Advancements in studying the TDR mechanism of spanwise wall oscillations were performed by Kempaiah (2019) who conducted planar PIV measurements on the oscillating wall. The results confirmed the TDR quantification by earlier works and provided instantaneous velocity fields of the TBL subjected to spanwise wall oscillation. Analysing these fields showed that wall oscillation significantly changed coherent structures in TBLs. However, as these phenomena are strongly three-dimensional it was proposed to acquire three-dimensional PIV velocity fields to study these changes which will enhance the understanding of the mechanism. This is of utmost importance when aiming to design a more effective and efficient actuation mechanism. The research aim and objective of this thesis is to narrow this gap in understanding the mechanism.

To study the three-dimensional coherent structures tomographic PIV is used on the test set-up designed by Kempaiah (2019). The wind tunnel is operated such that a TBL of $Re_\theta \approx 1{,}000$ is measured in order to be canonical with the results of Kempaiah (2019). Detailed description of the facilities, set-up, measurement technique and an uncertainty analysis is performed in chapter 5.

The results of the experimental series are discussed from two viewpoints in chapter 6. The first one is pointwise statistics which are validated with the planar data of Kempaiah (2019) and complemented with the variables requiring a three-dimensional measurement system. The second approach is to use three-dimensional instantaneous flow organisations to study the impact of wall oscillation on their characteristics. This is the novelty of this work aiming to understand the TDR mechanism better. Finally, the findings and answers found towards the research questions are concluded in chapter 7 along with recommendations for future work.

# 2

# The turbulent boundary layer

This chapter provides an overview of TBLs developing over a flat plate implying a zero pressure gradient TBL (ZPGTBL) with an emphasis on the important details with regard to turbulent skin friction. The concept of wall bounded flows is presented in section 2.1 along with the well known Reynolds decomposition of TBL field quantities. There are two common approaches for TBL analysis. One is the so called statistical method from which the scaling of TBLs is derived in section 2.3. The scaling parameters are essential to understand the governing physical parameters in the corresponding region of the TBL. The second approach is to analyse TBLs in terms of their coherent structures which is discussed in section 2.4. Section 2.5 gives an overview of the turbulent skin friction generation mechanism from a statistical point of view as well as the link between point-wise statistics and coherent structures. It is imperative to understand this mechanism in detail to identify the parameters which need adjustment through TBL control to reduce turbulent skin friction.

## 2.1. The concept of wall bounded flows

A special type of flow is the so called wall bounded flow which is described by the Navier-Stokes equations subject to the no-slip and non-permeability boundary condition at the wall, which read as given in eq. (2.1). In other words, the wall-normal velocity and the streamwise velocity is 0 at the wall.

$$(u)_{y=0} = (v)_{y=0} = 0 \tag{2.1}$$

The region where the flow develops from the wall conditions to the free stream conditions is called the boundary layer, schematically shown in fig. 2.2 for a flat plate.

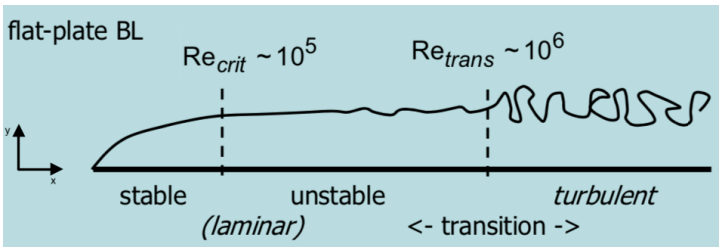


Figure 2.1: Development of a laminar boundary layer with turbulent transition over a flat plate (figure adapted from van Oudheusden, 2019)

It can be seen that there are three different regimes of the flat plate boundary layer which are the *stable*, *unstable* and *turbulent* regime. These regimes are separated by characteristic Reynolds numbers being $Re_{crit} \approx 10^5$ and $Re_{trans} \approx 10^6$, where the Reynolds number is given by eq. (2.2), $x$ being the streamwise position on the flat plate measured from the leading edge, $U_e$ is the external flow velocity and $\nu$ is the kinematic fluid viscosity.

$$Re = \frac{U_e x}{\nu} \tag{2.2}$$

In the *stable* regime, the boundary layer is laminar. The laminar boundary layer is characterized by following smooth streamlines and momentum transfer occurring on molecular scales. When $Re_{crit}$ is reached the laminar flow becomes unstable and when $Re_{trans}$ is reached the flow turns from laminar to turbulent. The TBL is characterized by a chaotic flow containing a large range of length and time scales. It also enhances mixing, as momentum is transported in bulks of molecules. These different characteristics also result in different velocity profiles for the laminar and turbulent case as shown in fig. 2.2. The laminar velocity profile is said to be less full than the TBL velocity profile. This implies that a laminar boundary layer possesses a lower streamwise velocity gradient at the wall in wall-normal direction than TBLs.

The wall shear stress, developed through the viscous nature of the boundary layer is given by eq. (2.3), implying that it is dependent on the gradient of streamwise velocity in wall-normal direction at the wall.

$$\tau_{wall} = \mu\left(\frac{\partial \overline{u}}{\partial y}\right)_{y=0} \tag{2.3}$$

Relating the given relationship in eq. (2.3) to the velocity profile characteristics in fig. 2.2 clearly shows that TBLs produce higher skin friction when compared to laminar boundary layers. This gives great motivation to study TBLs and its characteristics to find a way to reduce the generated skin friction (van Oudheusden, 2019).

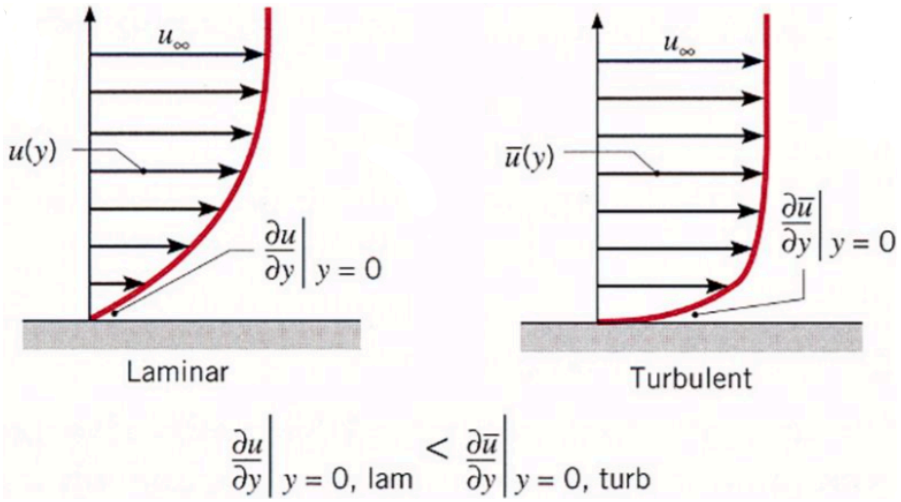


Figure 2.2: Laminar and TBL velocity profile (figure adapted fromUtah State University, 2019)

A further important concept for statistical analyses of TBL data is the so called Reynolds decompositions which splits a signal in a mean (denoted by an overbar) and a fluctuating part (denoted by a prime) as depicted in eq. (2.4) and fig. 2.3 taking the streamwise velocity component as a sample variable.

$$u = \overline{u} + u' \tag{2.4}$$

## 2.2. Turbulent boundary layer properties

The boundary layer thickness is defined as the wall-normal distance between the wall (y = 0 mm) and the point where the velocity of the boundary layer $u(y)$ reaches 99 % of the streamwise velocity of the external flow $U_e$ and is denoted by the symbol $\delta_{99}$. A graphical representation of the boundary layer thickness $\delta_{99}$ is given in fig. 2.4 (Veldhuis, 2018).

The problem of the boundary layer thickness concept is that the velocity distribution shows an asymptotic behaviour and therefore it has a rather arbitrary physical implication. To get physical meaningful parameters the displacement thickness, momentum thickness and the shape factor are defined

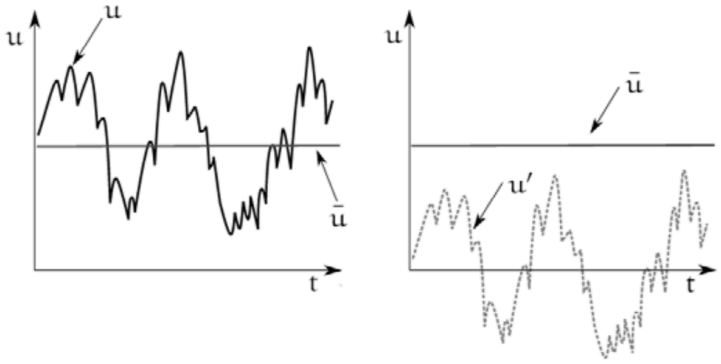


Figure 2.3: Mean and fluctuating decomposition (figure adapted from Reggente, 2014)

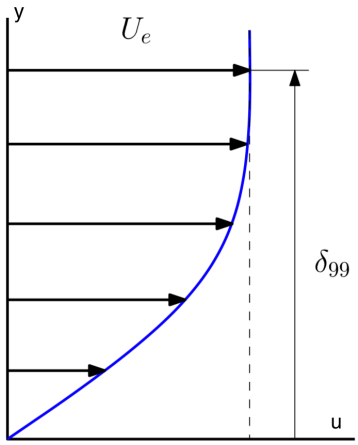


Figure 2.4: Boundary layer thickness (figure adapted from Veldhuis, 2018)

in the following.

The displacement thickness is an especially important concept with regard to the pressure distribution around an object surrounded by a viscous fluid flow and is denoted by $\delta^*$. A mathematical expression for the displacement thickness is given in eq. (2.5) and a graphical representation is given in fig. 2.5 (Veldhuis, 2018).

$$\delta^* = \int_0^\infty \left(1 - \frac{u(y)}{U_e}\right) dy \tag{2.5}$$

A more intuitive way to think of the displacement thickness is to imagine by how much the wall would have to be displaced into an inviscid flow while the flow maintains the same mass flow rate as in the viscous flow. Adding this thickness to the geometry and solving for an inviscid flow would yield accurate pressure distributions around the wall, however no information about the drag can be deduced from the displacement thickness.

The third property of boundary layers is the momentum thickness, defined as $\theta$ in eq. (2.6).

$$\theta = \int_0^\infty \frac{u(y)}{U_e}\left(1 - \frac{u(y)}{U_e}\right) dy \tag{2.6}$$

The intuitive explanation of the momentum thickness is to imagine the wall-normal distance by which the wall needs to be displaced in an inviscid flow while the flow retains the same streamwise momentum.

Furthermore, the shape factor is defined in eq. (2.7), being the ratio of the displacement thickness to the momentum thickness which gives important information about the shape of the boundary layer as depicted in fig. 2.6. A high shape factor indicates a concave velocity profile and a low shape factor indicates a convex velocity profile which also gives an indication of the velocity gradient at the wall and

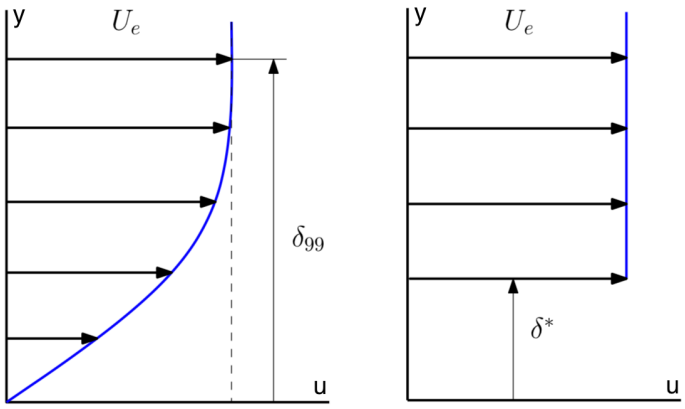


Figure 2.5: Boundary layer displacement thickness drawing where $\delta^*$ indicates the displacement thickness (figure adapted from Veldhuis, 2018)

consequently the skin friction drag (Veldhuis, 2018). Shape factor values reach up to 10 for a laminar separated flow. Typical values for TBLs are around 1.4 while the laminar Blasius profile possesses a shape factor of 2.59 (Masatoshi and Naomichi, 1985 and Stanford University, 2020).

$$H = \frac{\delta^*}{\theta} \tag{2.7}$$

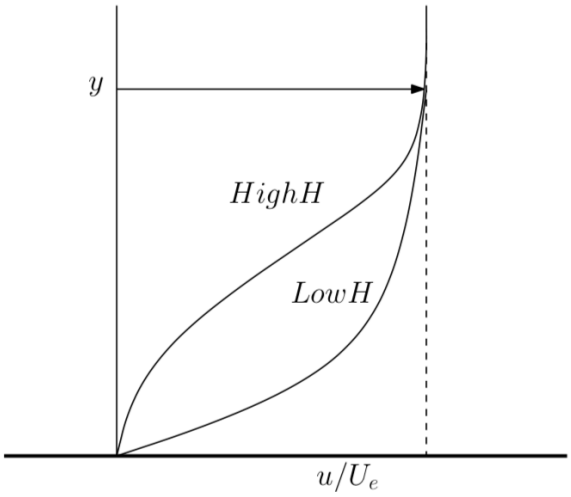


Figure 2.6: Boundary layer shape factor (figure adapted fromVeldhuis, 2018)

## 2.3. Scaling

TBLs can be divided in layers reaching from the wall at y= 0 up to $\delta_{99}$. The layer structure given in fig. 2.7. It splits the TBL in the outer and inner layer, having substantially different governing physical parameters.

The scaling laws for both layers can be derived using dimensional analysis. The outer layer is a function of the parameters given in eq. (2.8) which gives the so called ”defect law” as depicted in blue in fig. 2.7, where $U_e$ is the free stream velocity, $\delta_9 9$ is the boundary layer thickness, $y$ is the wall normal coordinate, $u_\tau$ is the friction velocity defined in eq. (2.9) and $p_e$ is the pressure of the external flow.

$$\frac{U_e - \overline{u}}{u_\tau} = g\left(\frac{y}{\delta_{99}}, \frac{\delta_{99}}{u_\tau}\frac{dp_e}{dx}\right) \tag{2.8}$$

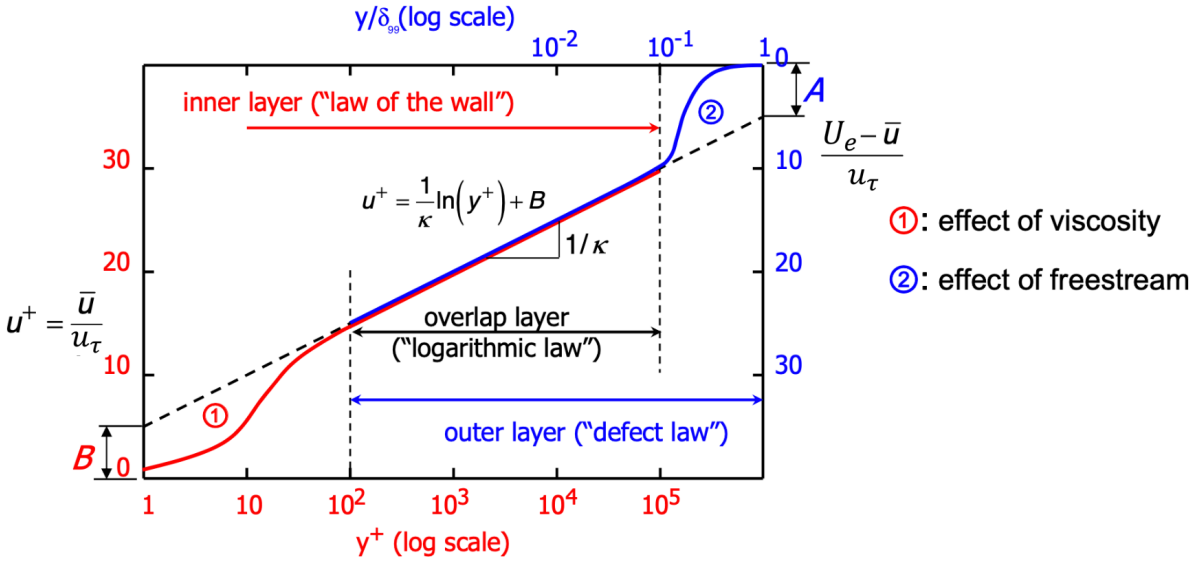


Figure 2.7: Layer structure of the TBL (figure adapted from van Oudheusden, 2019)

$$u_\tau = \sqrt{\frac{\tau_w}{\rho}} \tag{2.9}$$

The inner layer is a function of $y^+$ only as given in eq. (2.10), where $u^+$ and $y^+$ are defined in eq. (2.11) and eq. (2.12).

$$u^+ = f(y^+) \tag{2.10}$$

$$u^+ = \frac{\overline{u}}{u_\tau} \tag{2.11}$$

$$y^+ = \frac{y u_\tau}{\nu} \tag{2.12}$$

From these scaling laws it can be concluded that the outer layer is governed by the pressure gradient of the free stream and the inner layer is governed by viscous effects. This is an important finding as the generation of turbulent skin friction is a viscous effect (see section 2.5). This in turn limits the relevant part of the TBL for turbulent skin friction research to the inner layer which extends from $y^+$ = 0 to $y^+$ = 100 (see fig. 2.7). Therefore, the log-layer and outer layer are not part of the following discussion on coherent structures in TBLs and turbulent skin friction generation.

## 2.4. Coherent structures

Low-speed streak visualizations in a ZPGTBL exist from the work of Kline et al. (1967). They used helium bubble time lines introduced by a platinum wire into water flow. The flow had free stream velocities between 0.6 [m/s] and 2.1 [m/s] forming a TBL over a major portion of the 5.5 [m] long flat plate. The existence of low-speed streaks was shown between the wall up to $y^+$ = 38. However, the streaks appeared more sharp at the wall and tended to become unstable with increasing $y^+$. A clear visualization of the low-speed steaks at $y^+$ = 4.5 is shown in fig. 2.8a. The low-speed streaks are depicted by the bright regions which show an accumulation of the hydrogen bubbles. This inherently implies that regions of high-speed fluid must lie in between the low-speed streaks. Next to the existence of the near-wall streaks, Smith and Metzler (1983) found a characteristic spacing between low-speed streaks of 100 dimensionless wall units ($z^+$) in spanwise direction as shown in fig. 2.8b.

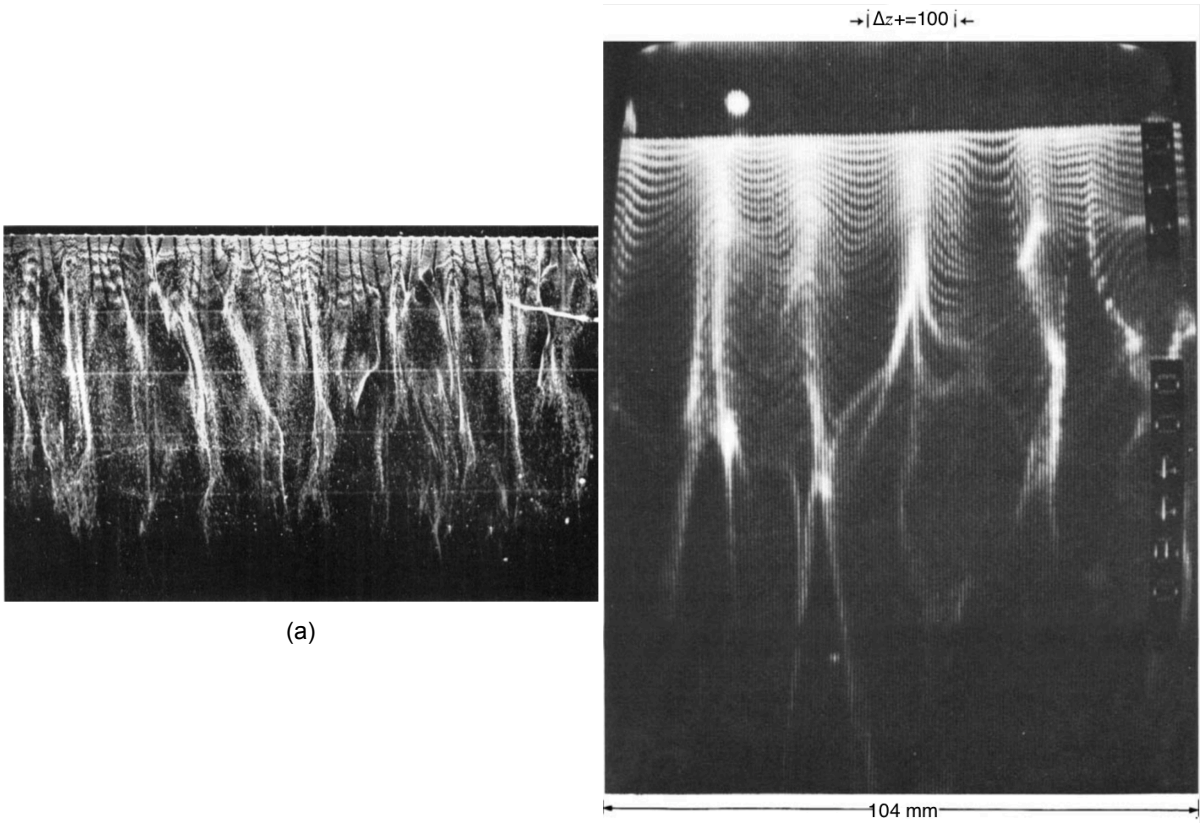


(a)

(b)

Figure 2.8: (a) Low-speed streak visualization using hydrogen bubbles at $y^+$ = 4.5 (Kline et al., 1967), (b) experiment on streaky structures in a TBL visualized at $Re_\theta$ = 740 (Smith and Metzler, 1983)

Hairpins were discovered in the early work of Theodorsen (1952) who initially named them horseshoe vortices (note that in this text, horseshoe vortex and hairpin vortex are synonyms). Adrien (2007) stated in a review article that, according to Theodorsen, horseshoe vortices constitute of a spanwise oriented vortex filament which is inclined by roughly 45 ° with respect to the wall into the mean flow. Therefore, the inclined part of the filament experiences higher mean streamwise velocity which stretches the filament in streamwise direction. A sketch of Theodorsens conceptual horseshoe model is given in fig. 2.9.

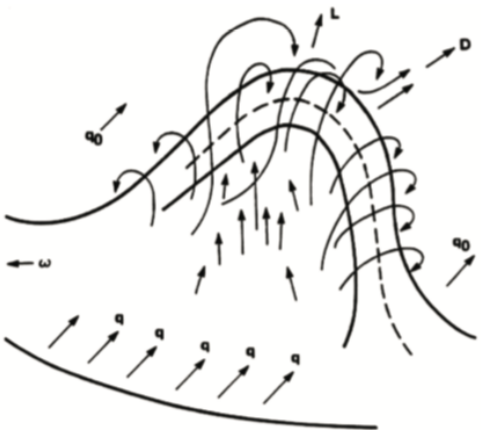


Figure 2.9: A sketch showing a horseshoe vortex (Theodorsen, 1952) following the work of Adrien (2007)

Head and Bandyopadhyay (1981) showed that the shape of hairpins is Reynolds number dependent. With increasing Reynolds number, the hairpins tended to elongate and the filament was spaced closer to each other in streamwise direction. In the same work, Head and Bandyopadhyay (1981) found that hairpins tend to exist in packets which increased in size with increasing Reynolds number. Therefore, they concluded that with increasing Reynolds numbers hairpins appeared in packets growing in size. Furthermore, Smith (1984) found in bubble visualizations that hairpins indeed existed in packets, thus supporting the findings of Head and Bandyopadhyay (1981). In the findings of Theodorsen (1952) the hairpin vortex appeared symmetrical and smooth, having a neck consisting of two inclined vortex filaments and an arch which connects the neck elements in spanwise direction. Robinson (1991) argued that a typical hairpin consists of the head, neck and additionally legs. The legs were comprised of streamwise vortex elements. A very important finding of Robinson (1991) was that hairpins rarely occurred in perfect symmetry but in only parts of the hairpins as shown in fig. 2.10. They mostly occurred in only streamwise vortices and or arches. Hairpins (or parts of hairpins) existed throughout the buffer and log-layer of TBLs according to Robinson (1991), implying that they were a dominant structure in the inner layer in their findings.

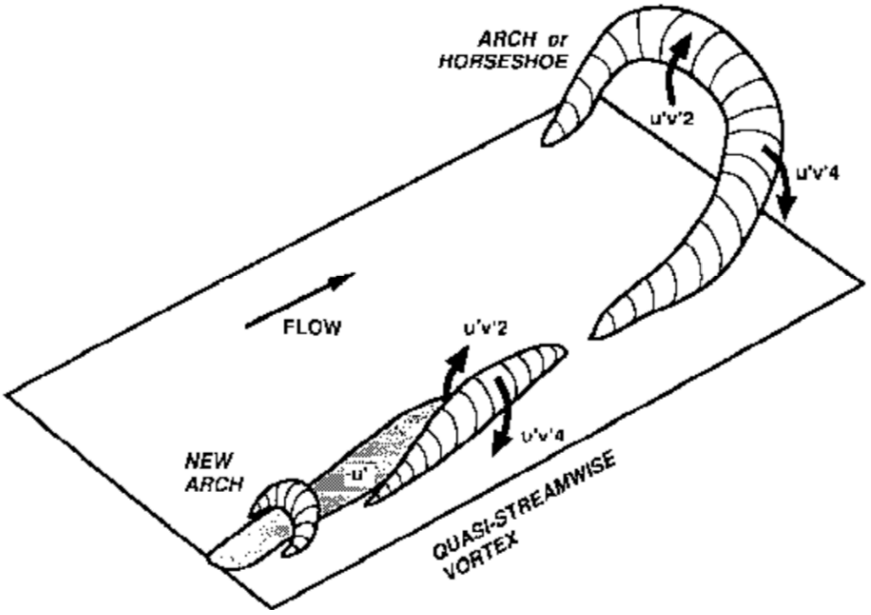


Figure 2.10: Arches, hairpins and quasi-streamwise vortices in TBLs (Robinson, 1991)

Further research of hairpin (packets) and their existence in TBLs was done by Adrian (2000) who described the hairpin shape and the induced velocities through the vorticity. Further he named its components (leg, neck and head) according to fig. 2.11. It also indicated the Q2 and Q4 events which both contribute to TKE production as will be seen in section 2.5.

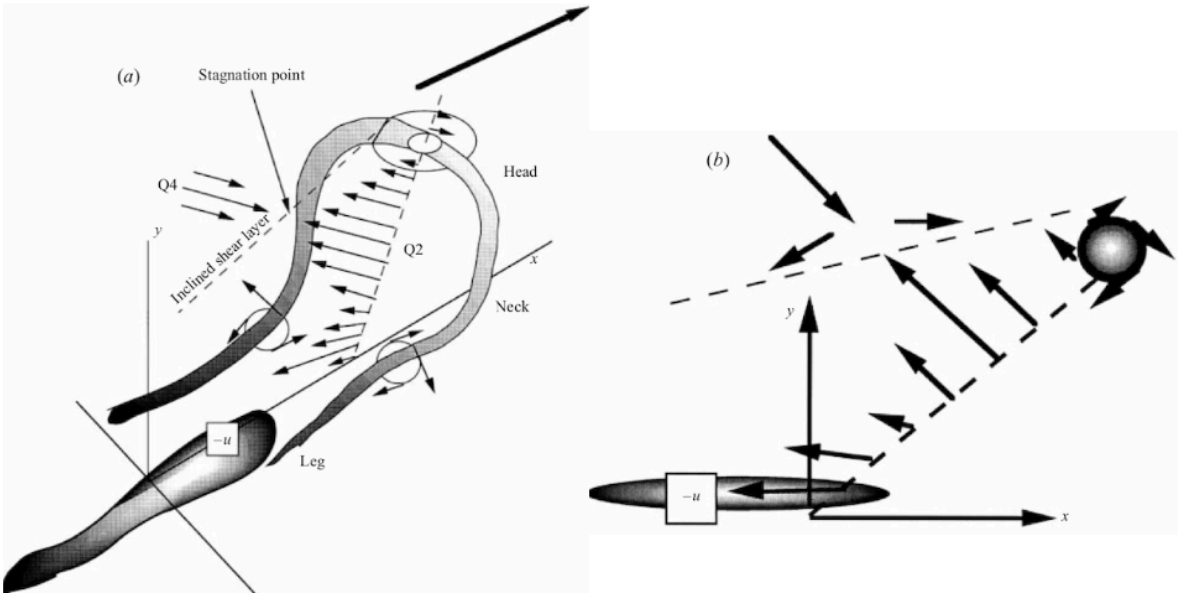


Figure 2.11: (a) schematic of a hairpin attached to the wall and (b) hairpin signature in streamwise-wall-normal plane Adrian (2000)

Figure 2.12 shows a conceptual model proposed by Robinson (1991) on the dynamic interaction between hairpins and low-speed streaks. It shows that low-speed streaks are induced through the spanwise vorticity of the hairpin arches and therefore lie in between the hairpin legs. As these legs are formed of streamwise vortex filaments they tend to lift the low-speed streaks located between their legs. This entails momentum transfer away from the wall through the streak inclination. This event is called an ejection. The induced momentum deficit through the ejection is compensated by faster moving fluid from the outer regions of the TBL towards the wall called the sweep event. Consequently, the mean streamwise velocity gradient in wall-normal direction at the wall is increased.

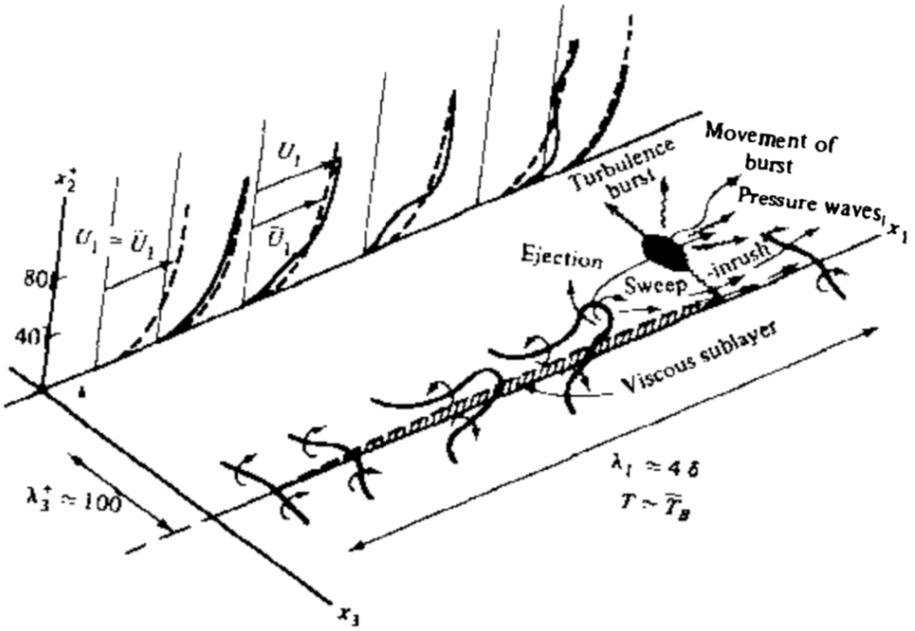


Figure 2.12: Vortical events in ZPGTBLs (Robinson, 1991)

The model of Robinson (1991) in fig. 2.12 proposed that the vorticity of the hairpins are the cause for

turbulence producing ejection and sweep events. Therefore, it is important to understand the formation of hairpins in TBLs. The research of Liu et al. (2014) shows that the formation of hairpins occurs in the boundary layer transition process form laminar to turbulent as shown in fig. 2.13.

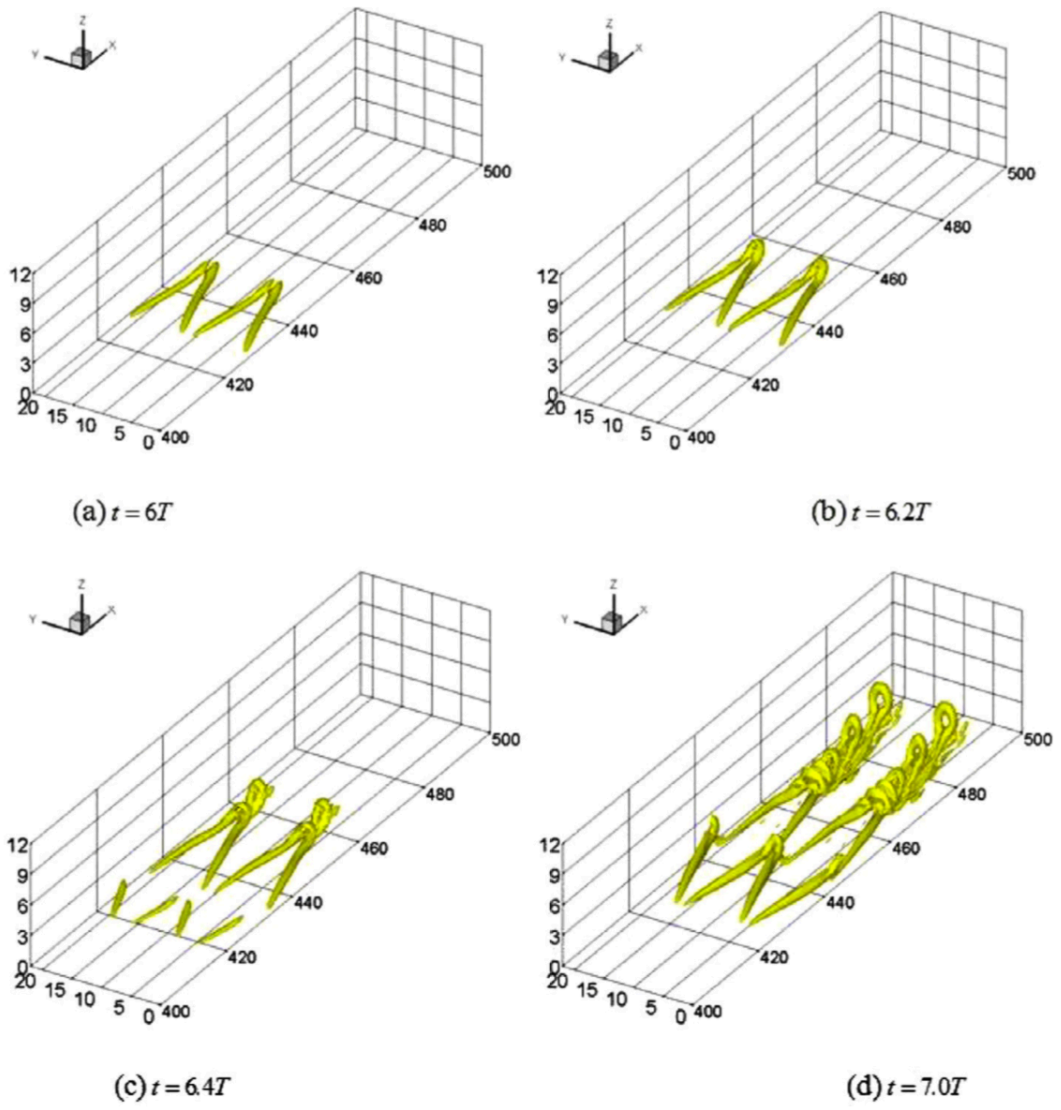


Figure 2.13: Formation of hairpins during boundary layer transition in chronological order from (a) to (d) (Liu et al., 2014)

Next to the hairpin formation in the transitional process, Zhou et al. (1997) showed that hairpins travel in packets in developed TBLs. These packets are a result of the hairpin autogeneration mechanism which says that a single hairpin in a TBL forms a hairpin packet containing more than one hairpin. The authors argue that this mechanism is the source of hairpin structures also in fully developed TBLs rather than just in the transition process. Zhou et al. (1997) found for a TBL at $Re_\theta \approx 1{,}000$ that hairpins in a packet are approximately spaced 100 non-dimensional streamwise wall units apart as shown in fig. 2.14.

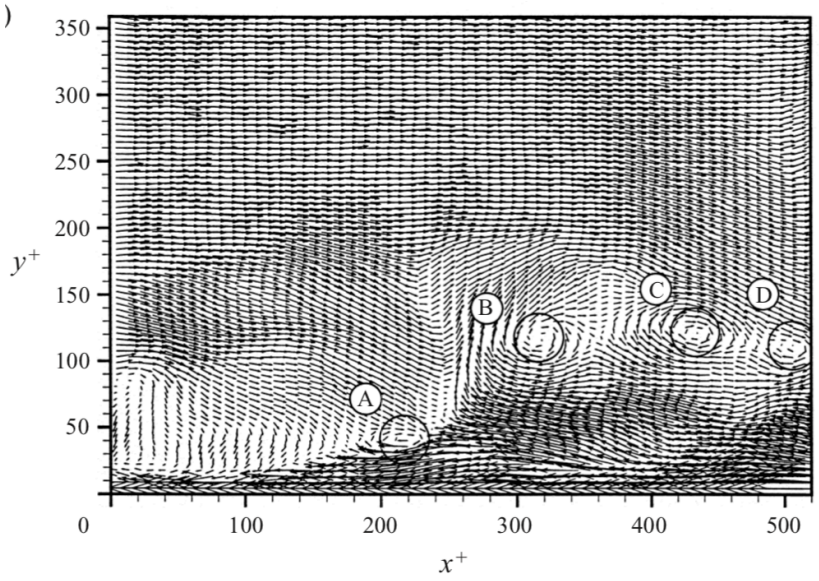


Figure 2.14: Hairpin packet in a fully developed TBL at $Re_\theta \approx 1{,}000$ (figure adapted from Zhou et al., 1997)

## 2.5. Generation of turbulent skin friction

Section 2.4 explained the typical coherent structures contained in a TBL. It was intuitively explained how the dynamic interaction between the low-speed streaks and hairpins lead so ejection and sweep events resulting in a high momentum transport from the outer region of the TBL to the wall. The increased streamwise momentum at the wall inherently leads to a larger gradient of the mean streamwise velocity in the wall-normal direction which results into a larger skin friction according to eq. (2.13).

$$\tau_w = \mu\left(\frac{\partial \overline{u}}{\partial y}\right)_{y=0} \tag{2.13}$$

Another straight forward way to assess the generation of turbulent skin friction is studying the turbulent kinetic energy (TKE) balance in TBLs. TKE is ”produced” at the large scales (being mainly coherent structures in TBLs) and is passed on to smaller scales until it is dissipated at the smallest scales. The definition of TKE is given in eq. (2.14) and its balance is given in fig. 2.15. The balance clearly reveals that TKE production peaks at around $y^+$ = 11. Viscous diffusion transports the TKE towards the wall where it is dissipated. This viscous diffusion and dissipation process is closely related to the generation of turbulent skin friction as friction is the mechanism by which the TKE is dissipated. This implies that the less TKE is transported to the wall through viscous diffusion, the less dissipation by skin friction is induced to keep the balance. From this follows that the production term as given in eq. (2.15) governs the magnitude of the wall skin friction (Hulshoff and Hickel, 2018).

$$k = \frac{1}{2}\left(\overline{(u)^2} + \overline{(v)^2} + \overline{(w)^2}\right) \tag{2.14}$$

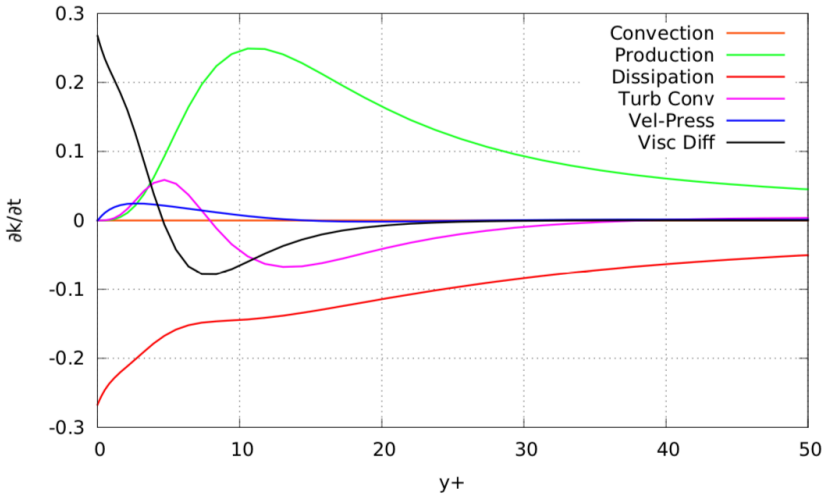


Figure 2.15: TKE budget terms vs. non-dimensional wall-normal distance (figure adapted from Hulshoff and Hickel, 2018)

$$P = -\overline{u_i{}' v_j{}'} \frac{\partial \overline{u_i}}{\partial x_j} \tag{2.15}$$

From the definition of the production term as given in eq. (2.15) follows that flow structures which are characterized by a negative product of $u'$ and $v'$ enhance TKE production. Fluctuating statistics of the coherent structures, namely streamwise vortices/hairpins, near-wall streaks and sweep/ejections are derived form a tomographic PIV experiment by Martins et al. (2019) and given in fig. 2.16.

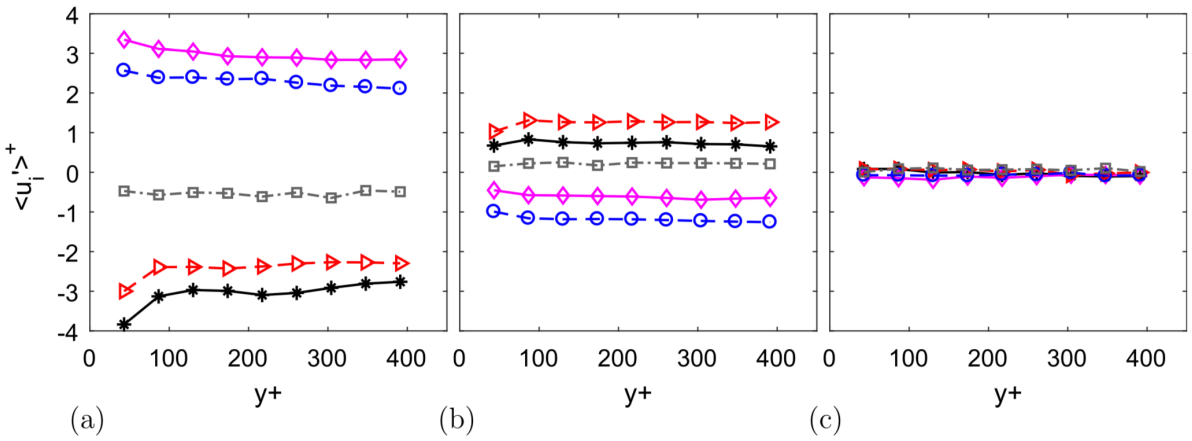


Figure 2.16: Non-dimensional velocity fluctuations in (a) u, (b) v and (c) w extracted per turbulent event: (diamond - purple) high-speed regions, (circle - dashed blue) sweeps, (rectangle - dashed grey) vortices, (triangle - dashed red) ejections, (stars - black) low-speed regions (Martins et al., 2019)

Statistical data of the coherent structures given in fig. 2.16 are discussed with respect to TKE production in the following. The discussion reveals that streaks, ejections and sweeps are the leading contributors to TKE production.

- **Vortices:** Vortices have the smallest offset in terms of velocity with respect to the mean flow in all three velocity components. This shows that the vortices itself are not the major contributor to TKE production, however they trigger turbulent events such as ejections and sweeps.
- **Low-speed regions & ejections:** The average velocity fluctuation data of the extracted flow region for low-speed regions show significant differences in wall-normal and streamwise direction.

Their average fluctuations in streamwise direction are negative and the wall-normal fluctuations are positive. The ejection is a follow-up event of the relatively slow lifting of the low-speed regions which is characterized by even higher wall-normal velocity fluctuations and a slightly smaller negative streamwise fluctuation when compared to low-speed streaks. From this it is derived, that both the low-speed regions and the ejections contribute to the turbulence production.

- **High-speed streaks & sweeps:** The momentum loss close to the wall due to the lifted low-speed streaks is compensated by the high-speed regions and sweep events. The high-speed regions move with a higher velocity in streamwise direction than the mean flow and with a negative velocity in wall-normal direction with respect to the mean flow, implying that they move towards the wall. The high-speed streaks result in the sweep event, which is characterized by a slightly lower streamwise fluctuation component with respect to the high-speed streaks which move faster towards the wall. The high-speed streaks and the sweep events are therefore also contributors to the production term of the TKE.

The Fukagata, Iwamoto & Kasagi (FIK) identity (Fukagata et al., 2002) also contributes towards understanding the generation of turbulent skin friction. It gives an expression of the turbulent skin friction coefficient as a function of TBL statistics. The expression for the skin friction coefficient is given in eq. (2.16) under the following assumptions:

1. Constant free stream velocity
2. Homogeneity in the spanwise direction
3. $\frac{\partial \bar{u}}{\partial y^*} = 0$ at $y^* = 1$ at with $y^* = \frac{y}{\delta_{99}}$
4. $u = w = 0$ at $y^* = 0$

$$C_f = \frac{4(1-\frac{\delta^*}{\delta_{99}})}{Re_{\delta_{99}}} + 2\int_0^1 2(1-y^*)(-\overline{u'v'})dy^* - 2\int_0^1 (1-y^*)^2\left(\overline{I_x} + \frac{\partial \overline{u}}{\partial t}\right)dy^* \tag{2.16}$$

with

$$\overline{I_x} = \frac{\partial \overline{(uu)}}{\partial x} + \frac{\partial (\bar{u}\bar{v})}{\partial y^*} - \frac{1}{Re_b}\frac{\partial^2 \overline{u}}{\partial x^2} \tag{2.17}$$

From eq. (2.16) and eq. (2.17) it becomes apparent that only the the second term of eq. (2.16) is variable for a fully developed TBL. This reveals that next to the magnitude of the term $-\overline{u'v'}$, also its weight towards the skin friction coefficient changes with its wall-normal position. If the distribution of this term is closer to the wall, the resulting skin friction coefficient is larger and vice versa.

So far the general characteristics of TBLs are discussed. These were chosen such that they give a solid basis to understand the concepts of turbulent drag reduction. There are several indicators for high turbulent skin friction which are aimed to be reduced/attenuated by the TDR techniques discussed in the next chapter. The indicators read as follows:

1. From eq. (2.13) it is derived that the mean streamwise velocity gradient in wall-normal direction at the wall is an indicator skin friction (large gradients result in high skin friction and a small gradients result in low skin friction assuming that the fluid's kinematic velocity is constant).
2. Studying the balance of TKE shows that a high level of dissipation is in close relation to increased turbulent skin friction. This implies that reduced TKE production lead to less dissipation and therefore less turbulent drag. More specifically, TKE production decrease is obtained if either the magnitude of $-\overline{u'v'}$ or $\frac{\partial \overline{u}}{\partial y}$ is decreased.
3. Related to this the FIK identity shows reduced skin friction for a lower magnitude of $-\overline{u'v'}$ and a redistribution away from the wall.

# 3

# Turbulent drag reduction

Section 3.1 gives an overview of TDR techniques which have been/are under research and/or industrial application and elaborates on the issues of the techniques explain the relatively low level of industrial readiness discussed in section 3.2.

## 3.1. TDR techniques

To achieve a reduction in turbulent skin friction at least one of the indicators discussed before has to be manipulated such that it has a turbulent drag reducing impact. The TDR techniques are categorised in passive and active techniques as described in the following (Yousefi and Saleh, 2015):

- **Passive:** Auxiliary power and control loop not required such as LEBU's and solid surface manipulation
- **Active:** Auxiliary power required such as wall blowing/suction, transversal travelling surface waves and spanwise wall oscillation

The remainder of this chapter reviews relevant TDR techniques documented on in literature which help to understand the concepts of TDR in practical and theoretical applications. It starts with the passive techniques in section 3.1.1 and section 3.1.2 followed by the active techniques in section 3.1.3 to section 3.1.5.

### 3.1.1. Large eddy break up devices

Large eddy break up devices (LEBUs) are passive flow control devices having a streamlined shape. They are placed parallel the object on which turbulent skin friction is to be decreased. As the LEBUs are placed in the TBL, they often possess the geometry of a flat plate or an airfoil to minimize device drag (Sahlin et al., 1988). An example illustration of an experimental set-up of two LEBU's attached to a flat plate with the goal to reduce skin friction on the plate is shown in fig. 3.1.

Experimental investigation of LEBU's was performed using direct drag measurement techniques, such as force gauges, to determine the total and skin friction drag of the plate. Examples are he work of Sahlin et al. (1988) and Lynn et al. (1995). Sahlin et al. (1988) found that the net drag was actually increased by 0-3 [%] while the TDR of the plate was reduced by 5 [%] in the best possible case, where the experiment was carried out at $Re_c$= 260,000 (based on LEBU's chord). The results of Lynn et al. (1995) showed that the LEBUs device drag was recovered by TDR up to 90 [%] in the best possible case and therefore also showed a net drag increase in the range between $Re_L$ = 150 to 300 million (based on the plat length $L$). Numerically, LEBUs were investigated by Chin et al. (2017) by a large eddy simulation (LES). Results showed that the TDR reduction balanced the LEBU device drag. These findings showed that the LEBU technique did not successfully induce a net drag reduction, however, it yielded TDR on the flat plate of interest. Finally, it shall be noted as the flow fields in the experiments described were not visualized and the LES simulation did not resolve the small scales, little insight in the mechanism leading to the TDR was given in the articles.

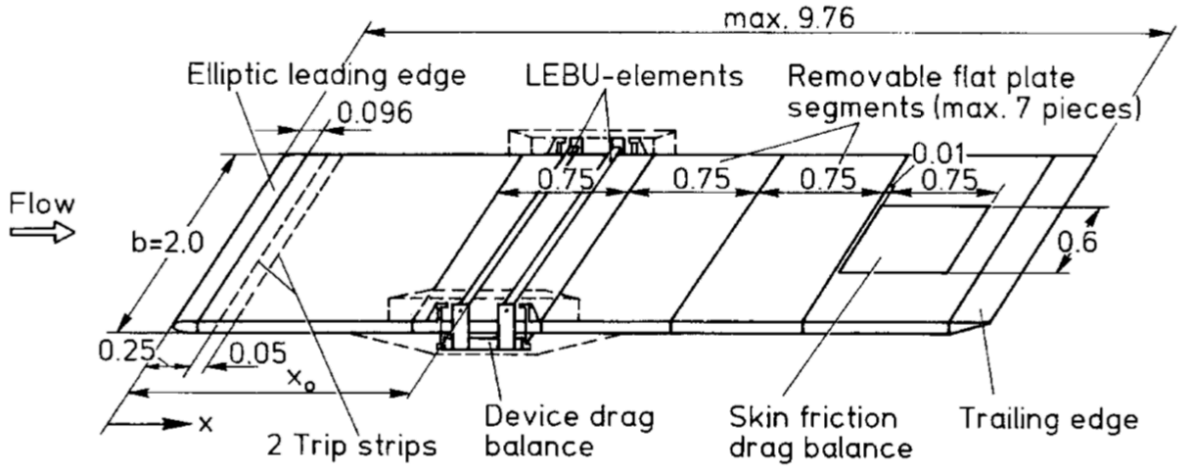


Figure 3.1: Experimental set-up clearly showing the direct force balances for LEBUs and skin friction, dimensions in m (Lynn et al., 1995)

### 3.1.2. Rigid surface manipulation

Riblets are a typical example where science learns from biology as their geometry was a adapted from a typical fast swimming shark skin which possesses streamwise ridges and valleys as shown in fig. 3.2a. Their exact spanwise cross section varies across many research articles. Therefore, the content of the review article of Choi (2013) is discussed which serves as a summary of riblet performance as a TDR technique. Figure 3.2b shows a summary of riblet performance in different flow regimes where the y-axis shows the drag of the manipulated surface with respect to the non-manipulated surface given as $[D_s/D]$ and the x-axis gives the dimensionless spacing $s^+$ (non dimensionalized by viscous wall units) of the riblets. Choi (2013) concluded that in the best possible combination of flight regime and riblet spacing, the TDR resulted in 8 [%].

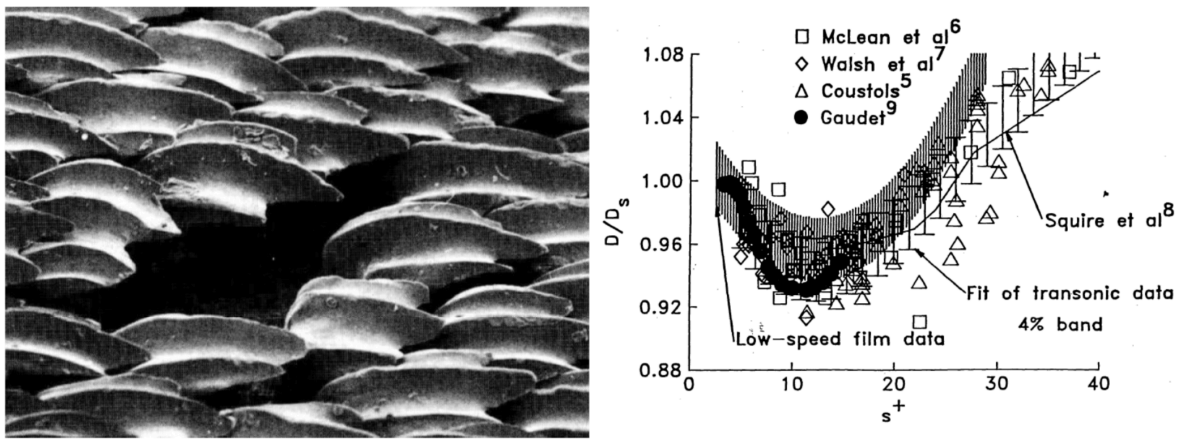


(a) (b)

Figure 3.2: (a) Skin of a shark (Choi, 2013), (b) Summary of experimental results measuring TDR by riblets (Choi, 2013)

Furthermore, the review article of Choi (2013) showed that the TDR varies with the geometry of the riblets. Choi (2013) concluded that the sharpness of the ridges governed the TDR percentage. The established relation showed that sharper riblet ridges led to a higher TDR. Next to scientific studies, the riblet technique also received considerable attention from industry as summed up in the same article by Choi (2013) . They have been investigated as early as in 1986 on a Learjet by NASA Langley who successfully found around 8 [%] TDR. Another flight test was performed by Airbus in 1989 on an A

320 resulting in 2 [%] of net drag reduction when 70 [%] of the aircraft skin was equipped with riblets. The degradation of the riblet effect was investigated by Airbus in cooperation with Lufthansa and Cathy Pacific Airways who tested the durability of riblets on an A340 in service. It was found that riblets have to be renewed every 2 to 3 years to keep constant performance (Choi, 2013), however Reneaux (2004) argued that riblets have to sustain at least 5 years in order to be economically beneficial. This kind of renewal of riblets is labour intensive, grounds the aircraft for days and is therefore costly. Furthermore, it can interfere with other maintenance activities such as a paint renewal. As a consequence of the labour intesive renewal of riblets, the aviation paint technique was invented by Stenzel et al. (2011). This paint possesses the geometry of riblets inside the structure of the paint, thus not requiring tooling on the skin. It was tested by Stenzel et al. (2011) on an airfoil in a wind tunnel and the resulting TDR was quantified to be 6 [%] with respect to the skin segments with usual paint up to $Re_L$ = 1.6 million.

Another surface manipulation technique which caught much interest in the recent past are micro-dimples. These micro dimples are manufactured in the skin segment and are of $\mu$m scale partially overlapping each other as described by Paik et al. (2015) achieving a TDR up to 3.38 [%] in water tunnels at $Re_\theta$ = 5,880. This technique seems to be promising as it is actively being researched to industrial readiness by the TU Delft start-up company ”Dimples” cooperating with Airbus to develop TDR techniques using dimples (Dimple Technologies, 2020).

The discussion on surface manipulation technique shows that up to 8 [%] TDR is achievable, however the trade-off between biological wear, cost and TDR needs to be fine tuned prior to permanent industrial service.

### 3.1.3. Wall blowing/suction

Wall blowing and suction is an active technique as it imposes a wall-normal and/or streamwise velocity component at the wall. There are two distinct spatial methods, one which applies the additional velocity component only at one streamwise position through a slot. The other branch applies the blowing/suction component through a micro-perforated surface, implying that the flow component is applied over an area. The two different methods are depicted by experimental set-ups following Kornilov and Boiko (2016) and Park et al. (2001) in fig. 3.3.

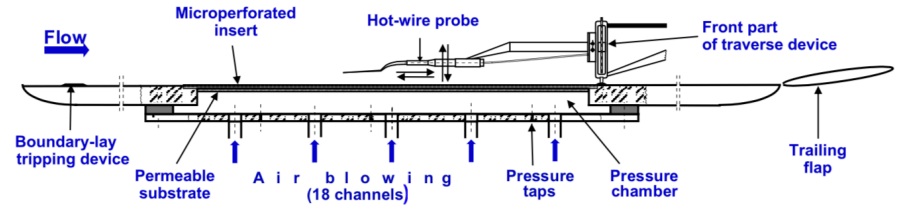


(a)

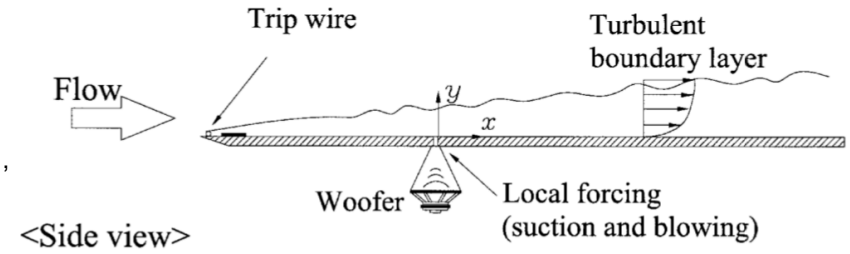


(b)

Figure 3.3: (a) Area injected test set-up (Kornilov and Boiko, 2016) (b) slot injection test set-up (Park et al.,2001)

Considerable work on area injected wall blowing/suction was performed by Choi et al. (1994) through DNS and Kornilov and Boiko (2016) through experimental investigation. Choi et al. (1994) implemented a feedback loop on the wall blowing/suction signal based on the flow characteristics at a wall parallel plane at different wall-normal distances. The principle was to scan the v-component of the velocity at a certain wall-normal distance and to introduce the same magnitude but reversed direction as a wall

blowing/suction signal. This method was named v-control. The same principle was investigated but using the w velocity component thus blowing or sucking air in wall parallel streamwise direction, called w-control. Choi et al. (1994) found up to 30 [%] for the optimal detection plane position at $y^+$ = 10 for $Re_\theta$ = 1,800. In practice it is highly infeasible as the detection plane would require a plane of sensors in the flow which are likely to be intrusive and therefore corrupt the flow. The study also contained a detection plane at the wall, however resulting in only 6 [%] TDR. Choi et al. (1994) proposed that the v-control simply pushed away sweep events from the wall and that the w-control weakened streamwise vorticity which was known to have a central role in turbulent skin friction reduction. Kornilov and Boiko (2016) used blowing over an area with constant magnitude through a micro-perforated wall as depicted in fig. 3.3a. A significant TDR of up to 87 [%] was reached over the actuated section of the wall at $Re_L$ = 0.56 million.

Wall blowing/suction through a slot was investigated by Masatoshi and Naomichi (1985) and Park et al. (2001). Masatoshi and Naomichi (1985) used constant wall blowing and suction documenting increased skin friction coefficients for suction and decreased skin friction coefficients for blowing. As opposed to the area injection, the maximum reduction/increase was found just downstream the slot after which it recovered asymptotically to the non-controlled state. Furthermore, it was concluded that the effect increased with increasing blowing/suction strength. Maximum local change in skin friction (increase and decrease) reported for the highest blowing signal was 66 [%] at the position downstream closest to the slot. Park et al. (2001) also investigated slot injected wall blowing/suction and applied a sinusoidal forcing signal, thus combining blowing and suction at $Re_\theta$ = 1,700. The same general effect has been reported as from Masatoshi and Naomichi (1985) where the maximum effect was found immediately downstream of the slot and the asymptotic recovery further downstream. Maximum local TDR % downstream the slot was found to be 45 [%]. Furthermore, it was concluded that the effect on turbulent skin friction increases with increasing frequency of the forcing signal.

### 3.1.4. Spanwise travelling transversal waves

The method of TDR by a spanwise travelling transversal waves was subject of the research of Klumpp et al. (2011), Roggenkamp et al. (2015) and Koh et al. (2015) who conduced numerical LES and experimental studies of the technique. The corresponding numerical and experimental set-ups show the working principle of the technique in fig. 3.4. The numerical work of Klumpp et al. (2011) implemented the working principle by the no-slip boundary condition of the moving wall and the experimental set-up of Roggenkamp et al. (2015) used an aluminium sheet with longitudinal bars underneath which were actuated in wall-normal direction to produce a travelling surface wave.

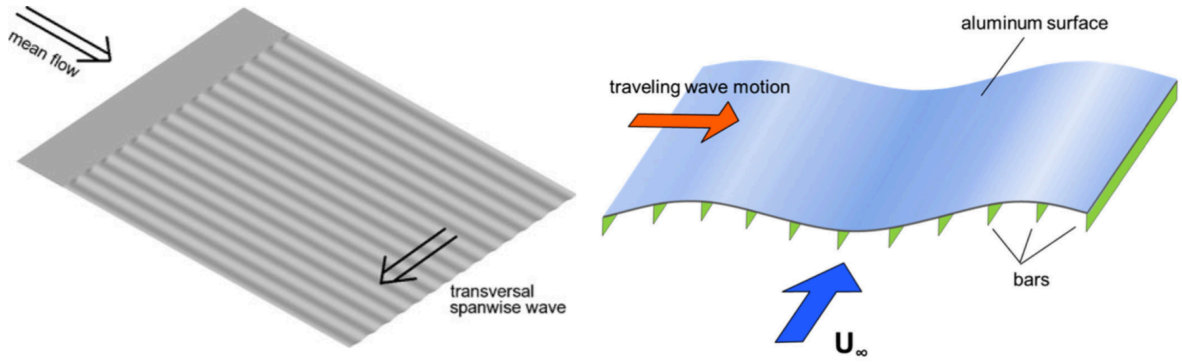


(a) (b)

Figure 3.4: (a) Numerical set-up (Klumpp et al. 2011) (b) experimental test set-up (Roggenkamp et al., 2015)

Klumpp et al. (2011) conducted the LES at $Re_{\delta^*}$ = 1,000 and found that the TDR was dependent on the characteristics of the surface wave. In total, two waves were tested, one showed a reduction in TKE production leading to a positive TDR and another one showing an increase in TKE production leading to a negative TDR. It is worth mentioning that the authors found increased streamwise vorticity

for the positive TDR case which challenged the common view that a positive TDR is in close relation with reduced streamwise vorticity which plays a vital role in the TKE production of non-controlled TBLs. Furthermore, the authors found reduced wall-normal velocity fluctuation which imply reduced TKE production following their line of argumentation.

The work of Koh et al. (2015) elaborated on the relation between TDR and the surface wave characteristics as well as a Reynolds number effect. They show from LES simulations that the TDR steadily increased with $A^+$ at $Re_\theta$ = 1,000 and had a peak at $A^+$ = 30 for $Re_\theta$ = 2,000 and 3,000. This implied that in general the TDR tends to increases with $A^+$ up to 30. A further important finding was that the magnitude of the possible TDR decreased with increasing $Re_\theta$.

The experimental findings of Roggenkamp et al. (2015) confirmed the observations from the numerical studies. The campaign tested at different $A^+$ and $Re_\theta$ and confirmed that the TDR magnitude decreased with increasing $Re_\theta$ while at $Re_\theta$ = 1,200, the TDR steadily increased with $A^+$ and appeared to have an optimum at an intermediate $A^+$ for higher $Re_\theta$ = 1,660 and 2,080.

### 3.1.5. Spanwise wall oscillation

Spanwise wall oscillation has been reported by many researchers, i.e. Jung et al. (1992), Laadhari et al. (1994), Arturo and Quadrio (1995), Choi et al. (1998), Ricco and Shengli (2004), Qaudrio et al. (2009), Gouder et al. (2013) and Kempaiah (2019). All of the mentioned researchers agreed that a maximum TDR of around 45 [%] could be obtained by spanwise wall oscillation. This showed that this technique offers high TDR potential as compared to the other techniques discussed. However, next to the quantification of the TDR, there existed many contradicting opinions such as the best practical mechanism to oscillate the wall, hypotheses about the mechanisms in TBLs under spanwise wall oscillation resulting in the TDR and the importance/presence of Reynolds number effects. Therefore, a separate chapter is dedicated to this technique discussing the important points in chapter 4.

## 3.2. Industrial readiness of TDR techniques

Section 3.1.1 to section 3.1.5 have shown that the techniques aiming to reduce turbulent drag are numerous. It became apparent that the techniques differ in their TDR potential from barely any effect of LEBU's to attainable TDRs up to 87 [%] for active techniques such as wall blowing/suction and oscillated walls. However, the literature review showed that only the solid surface manipulation techniques in form of riblets, dimples and aviation paint received industrial attention up until today.

One reason may be that boundary layer transition delay mechanism are much more efficient as they prevent the regime of much higher skin friction generated by TBLs compared to laminar boundary layers. However, Reynolds numbers on aeroplanes reach magnitudes up to $10^7$ (Swift, 2009) which is far above $R_{trans} = 10^6$. This shows the need for TDR techniques in addition to transition delay mechanisms.

Further problems in implementing TDR techniques are summarized in the following points:

- Some numerical studies are simply not feasible in practice such as the v- and w-control techniques as proposed by Choi et al. (1994) due to the sensor plane which needs to be placed in the flow. Surface waves and spanwise wall oscillations would pose huge requirements on the skin structure when they are actuated by a moving actuation mechanism such as crankshaft actuation.
- The set-up of the active control mechanism is expensive, adds additional weight and needs energy input to be operated which gives doubts whether a net effect is attainable (compare the study of Arturo and Quadrio, 1995).
- TDR techniques can suffer from biological wear. As an example, the degrading performance of the aviation paint is given (Stenzel et al., 2011).

These points remain to be researched and improved to see more TDR techniques in industrial applications.

# 4

# Spanwise wall oscillation

This chapter gives a detailed overview of TDR by spanwise wall oscillation. Section 4.1 gives an introduction of the technique describing the working principle and its governing parameters. Section 4.2 gives an overview of known actuation mechanisms and how the working principle can be implemented either numerically or experimentally. The significant statistical differences of a TBL under spanwise wall oscillation with respect to a unactuated TBL are given in section 4.3. Frequently used but different scaling methods are discussed in section 4.4. The mechanism in terms of coherent structures is discussed in section 4.5. How much TDR is possibly attainable and its sensitivity to the wave parameters and Reynolds number is discussed in section 4.6. Finally, net energy balances are summarized in section 4.7 and the thesis research aim complemented with research questions is given in section 4.8.

## 4.1. Working principle and governing parameters

The working principle of TDR by spanwise wall oscillation is depicted in fig. 4.1, showing the streamwise direction as x, spanwise direction as z and wall-normal direction as y. The rectangle shown is a flat plate on which a ZPGTBL is attached. The difference to a stationary plate is that the wall is moving in spanwise direction with velocity $w_{wall}$ following a sine signal as depicted by the large arrow at the flat plates trailing edge. The wall velocity is described by the angular frequency $\omega$ and amplitude $A$ as a time signal depicted by $t$. There are various methods how this principle is modelled in numerical simulations and experimental set-ups, which is discussed more detailed in section 4.2 (Arturo and Quadrio, 1995).

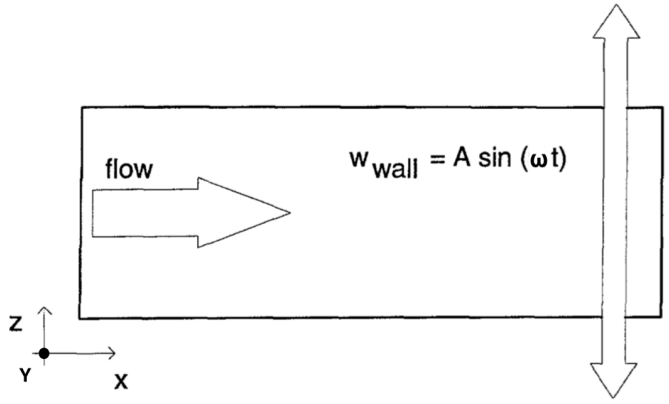


Figure 4.1: Working principle of a spanwise oscillating plate (Arturo and Quadrio, 1995)

From the oscillating motion of the wall given in fig. 4.1 and eq. (4.1), two main dimensionless parameters can be derived which govern the motion. These can be used to scale the wave motion to all kind of TBLs. The parameters are the dimensionless period $T^+$ and amplitude $A^+$ of the sine wave given in eq. (4.2) and eq. (4.3), respectively.

$$w_{wall} = Asin(\omega t) \tag{4.1}$$

$$T^+ = \frac{T \cdot u_\tau^2}{\nu} \tag{4.2}$$

$$A^+ = \frac{A \cdot u_\tau}{\nu} \tag{4.3}$$

In eq. (4.2) and eq. (4.3), $T$ is the dimensional period of the wave, $u_\tau$ is the friction velocity (note that it varies in literature if $u_\tau$ of the stationary or non-oscillated case is used) and $\nu$ is the kinematic viscosity of the corresponding fluid.

## 4.2. Actuation mechanisms

This section describes the different actuation mechanisms deployed so far in research (numerical and experimental). A high level differentiation is made between moving the wall itself or inducing a streamwise velocity component immediately at the wall.

Jung et al. (1992) conducted a DNS on TCF and modelled the oscillating wall by a spanwise boundary condition component ($v_{wall} \neq 0$). Another method used by Jung et al. (1992) was a spanwise induced cross flow component. No significant differences between these two methods were reported in terms of result. In Arturo and Quadrio (1995) and Qaudrio et al. (2009), the wall was modelled via the wall boundary condition ($v_{wall} \neq 0$).

The traditional method in experimental research on TDR through spanwise wall oscillation is the actuation of a flat plate by an electrical motor - crankshaft system as depicted in fig. 4.2 which is also used by Kempaiah (2019).

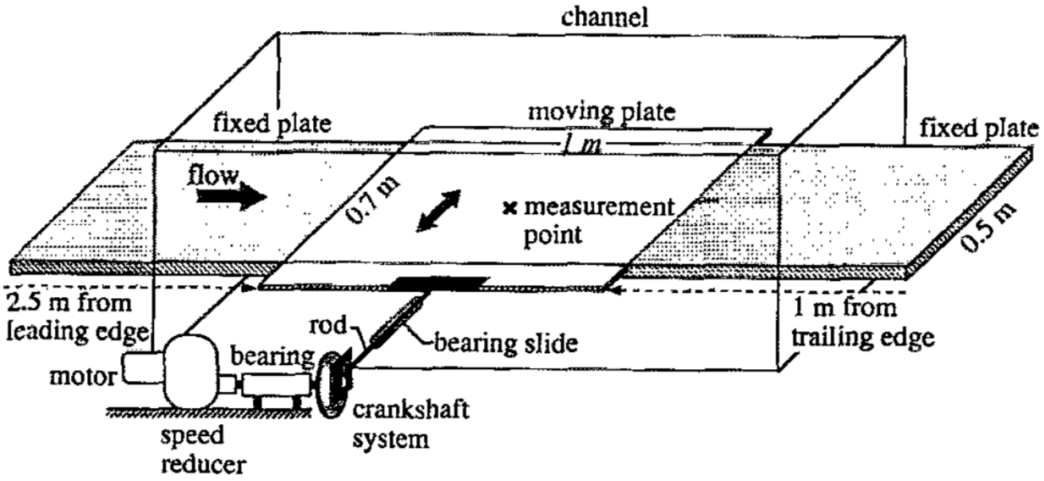


Figure 4.2: Crankshaft actuation system as used by Laadhari et al. (1994)

It is quite apparent that the crankshaft actuation mechanism is not suitable to be installed on aeroplanes as it introduces vibrations and it would have to be installed somewhere off the wing surface. Therefore, more recent experimental research of Gouder et al. (2013) focussed on alternative actuation such as electroactive polymers (EAPs) in the dielectric form of actuation and an electromagnetic-driven linear motor.

The EAP actuator and the linear electromagnetic motor which possess the common disadvantage that the wall is not stationary but has to physically oscillate. This is wished not to happen on aircraft skin segments. Therefore, another actuation technique by DBD (dielectric barrier discharge) plasma actuators has been under research recently by Whalley and Choi (2014). This actuator is characterized by a stationary wall and an induced flow through a plasma build up between two electrodes.

## 4.3. Pointwise velocity statistics

The TBL statistics of the oscillated wall case gives insights in the TDR mechanism when compared to the stationary wall. The main differences were identified by many researches in the mean streamwise velocity profile, turbulence intensities and Reynolds stresses. These differences led to adjusted TKE production and dissipation terms. These quantities are addressed in section 4.3.1 to section 4.3.3.

Each of these statistical considerations is discussed hereafter separately and is supported by citations of research articles supporting the findings.

### 4.3.1. Mean velocity profiles

Figure 4.3 clearly shows the change in the dimensionless streamwise velocity profile of the TCF-DNS study by Jung et al. (1992) and the experimental study of TBLs by Laadhari et al. (1994). The change in wall-normal gradient of streamwise velocity ultimately leads to TDR. These findings were confirmed in later works by Arturo and Quadrio (1995), Choi et al. (2011), Gouder et al. (2013) and Kempaiah (2019).

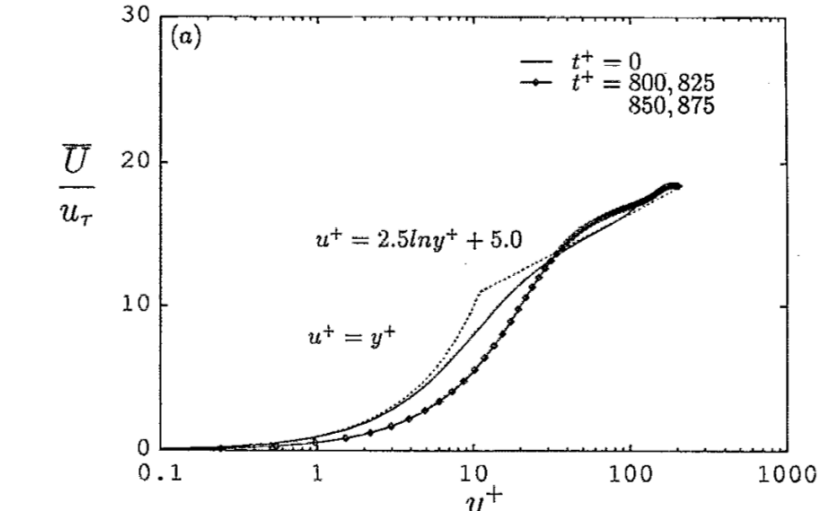


(a)

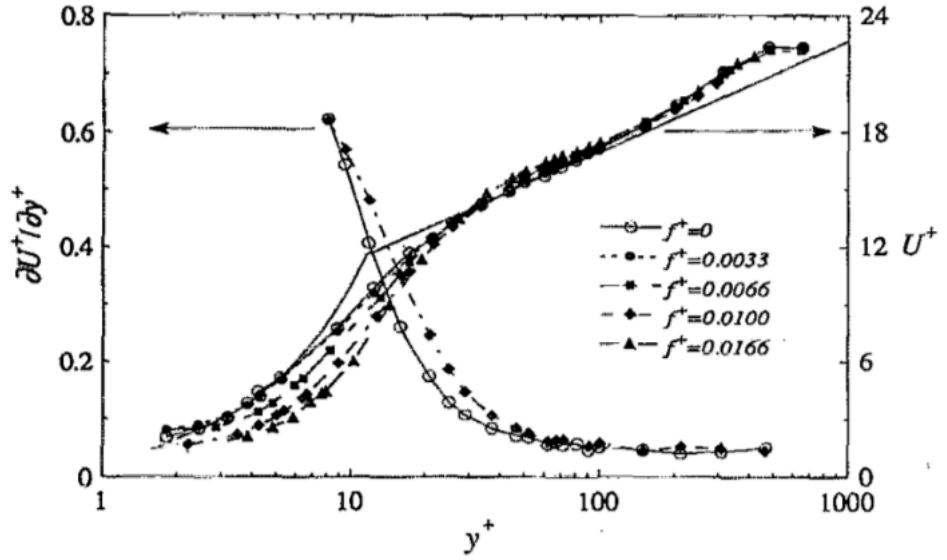


(b)

Figure 4.3: Velocity profiles oscillated vs. non-oscillated for: (a) TCF (Jung et al., 1992) and (b) TBL (Laadhari et al., 1994)

### 4.3.2. Turbulence intensities

Figure 4.4 shows that in the TCF-DNS of Jung et al. (1992) and the TBL experimental study of Laadhari et al. (1994) all components of the turbulence intensities were clearly decreased when the wall was oscillated. However, there were differences between TCF and TBL results. TCF results showed a similar decrease in all quantities whereas in the TBL, the decrease of streamwise turbulence intensity was much larger than the other two components. These findings were supported by the work by Arturo and Quadrio (1995), Choi et al. (2011), Gouder et al. (2013) and Kempaiah (2019).

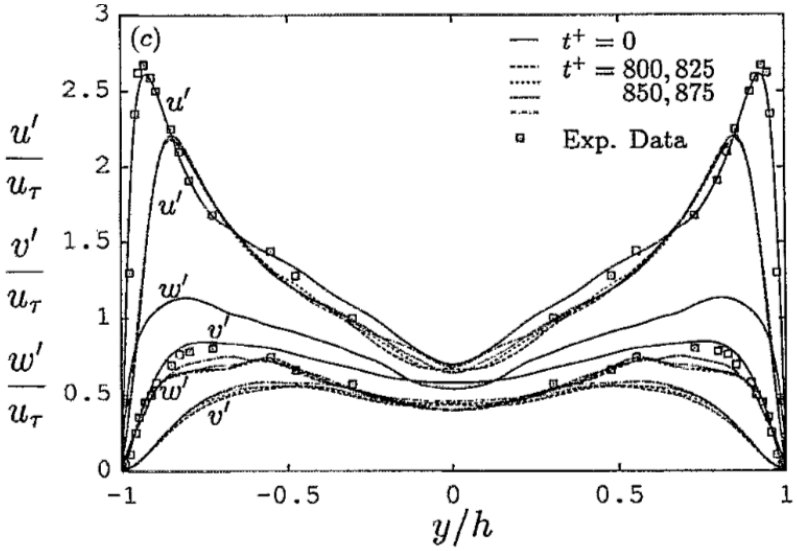


(a)

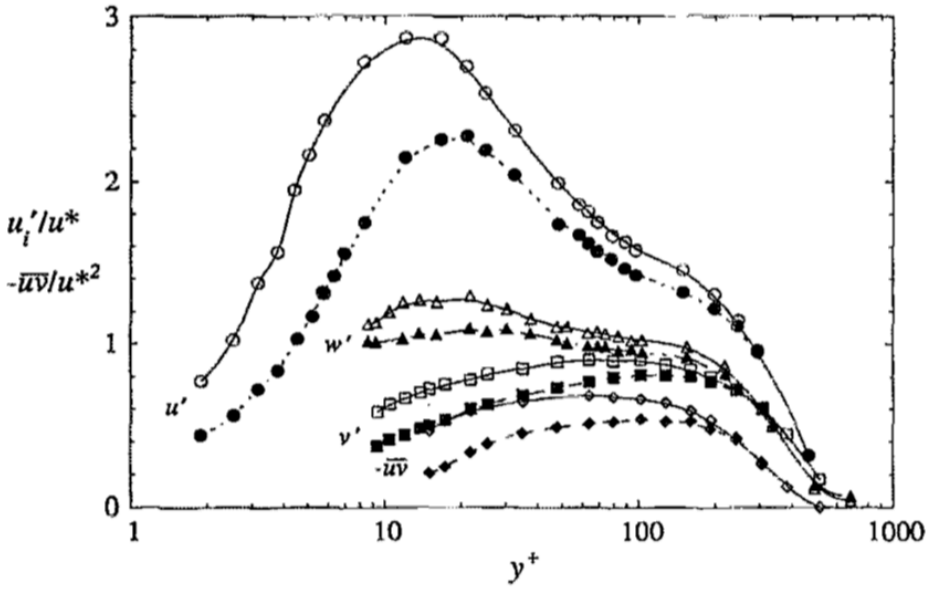


(b)

Figure 4.4: Turbulence intensities oscillated vs. non-oscillated for: (a) TCF (Jung et al., 1992) and (a) TBL (Laadhari et al., 1994)

### 4.3.3. Reynolds shear stresses and turbulent kinetic energy budget

Figure 4.5 shows that the Reynolds stress $-\overline{u'v'}$ decreased for both, the TCF and TBL by Jung et al. (1992) and Laadhari et al. (1994). This was a very important finding, as this Reynolds stress is in close relation to turbulent skin friction shown by the FIK identity (section 2.5).

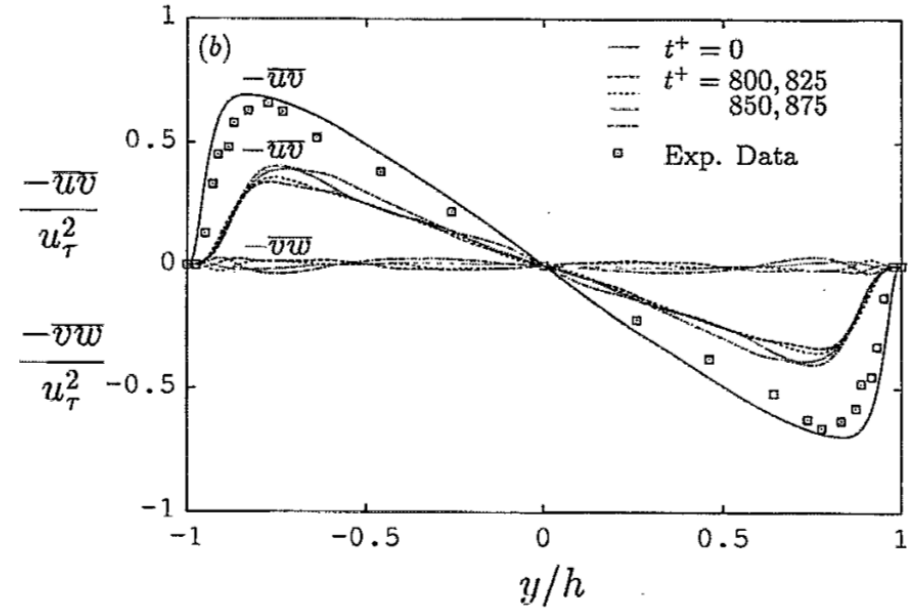


(a)

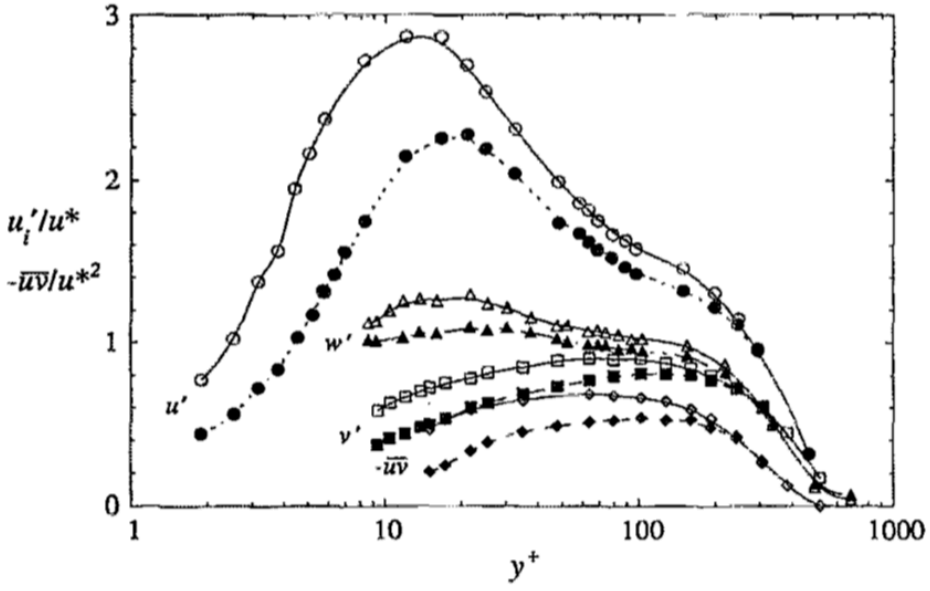


(b)

Figure 4.5: Reynolds stresses oscillated vs. non-oscillated for (a) TCF (Jung et al., 1992) and (a) TBL (Laadhari et al., 1994)

Furthermore, this Reynolds stress is responsible for the main turbulence production ($P \approx -\overline{u'v'}\frac{\partial \overline{u}}{\partial y}$) in TBLs which is a major indicator for turbulent skin friction. It indirectly represents the intensity and frequency of sweep and ejection events, thoroughly discussed in section 2.4. It was shown by Arturo and Quadrio (1995) that the spanwise wall oscillation had the biggest impact on the TKE production and dissipation term. Both of them showed a much smaller maximum magnitude and the peak of the production term was shifted away from the wall. These effects were shown already before in this report to reduce turbulent skin friction. Decreased Reynolds stresses and TKE production were also confirmed by Kempaiah (2019).

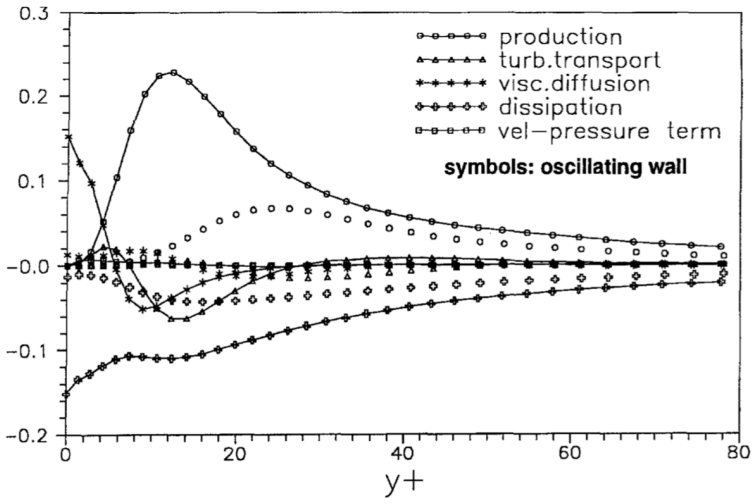


Figure 4.6: TKE balance for oscillated vs. non-oscillated case (Arturo and Quadrio, 1995)

## 4.4. Scaling

Gouder et al. (2013) investigated the impact of different scaling approaches as there appear to be contradicting opinions on the way of scaling velocity profiles, turbulence intensities and Reynolds stresses as well as the TKE budget in the field of TDR by spanwise wall oscillation. The statistics shown in section 4.3 were all scaled using the friction velocity $u_\tau$ of the non-oscillated case. Another option of scaling was to use $u_\tau$ of the oscillated case. There was no right or wrong about which one to use, but it was very important to state which method was used. The major difference between the two methods was that the unperturbed $u_\tau$ scaled the log-layer of the velocity profile and made the drag reduction apparent in terms of the wall gradient as seen in fig. 4.7. If $u_\tau$ of the oscillated case was used, it was seen that scaling was valid in the near-wall region up to $y^+$ = 10, but an upward shift in the log-layer was apparent (fig. 4.8).

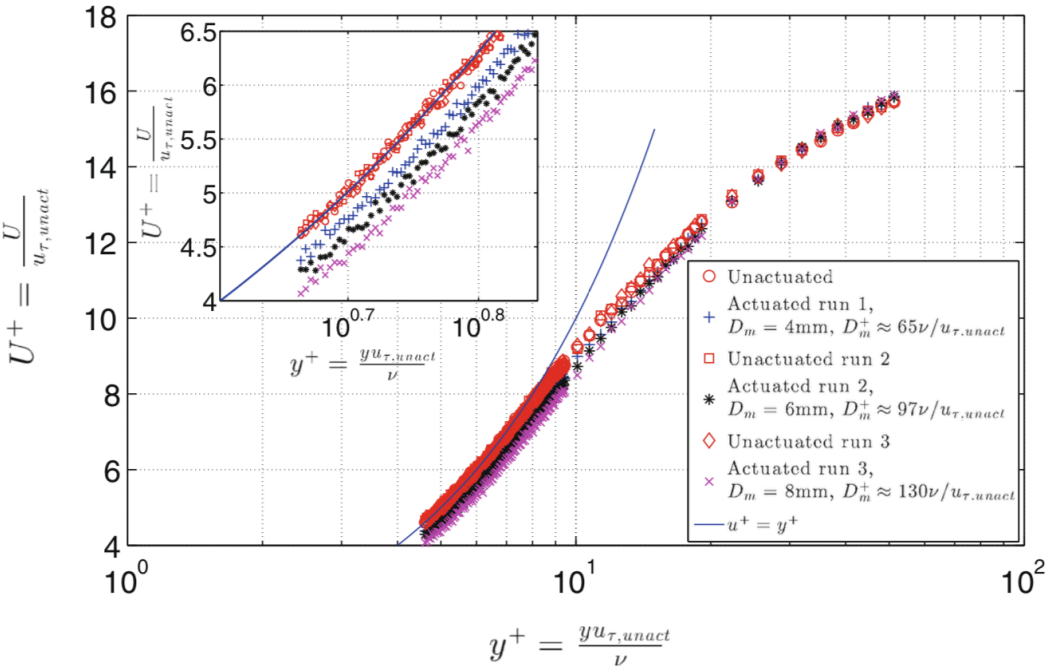


Figure 4.7: Mean streamwise velocity profiles scaled with non-oscillated wall $u_\tau$ (Gouder et al., 2013)

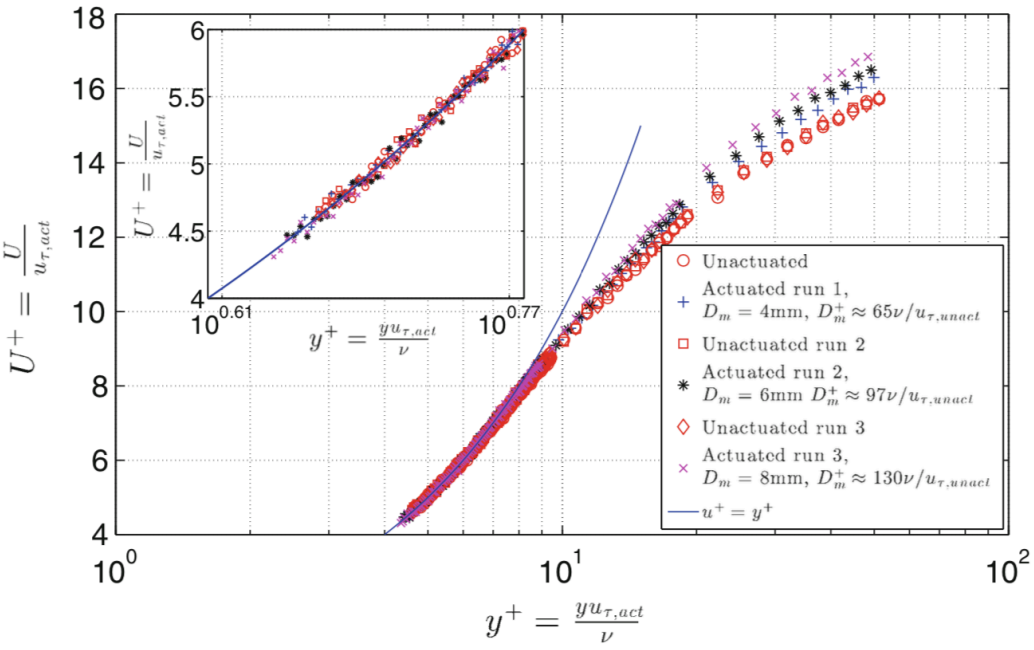


Figure 4.8: Mean streamwise velocity profiles scaled with oscillated wall $u_\tau$ (Gouder et al., 2013)

## 4.5. Turbulent drag reduction mechanism

The mechanism in terms of coherent structures which leads to the TDR by spanwise wall oscillation was discussed in contradiction among different researches. There are two main theories. Arturo and Quadrio (1995) argued that there is a Stokes (or Rayleigh) layer generated by the spanwise wall oscillation which lifted up the longitudinal vortices above the position of the streaks as shown in fig. 4.9. The streaks were mostly contained in the 10 wall unit thick Stokes layer and the vortices were positioned above which prevented the interaction between the two. This led to less turbulence producing events such as ejection and sweeps and therefore reduced turbulent drag.

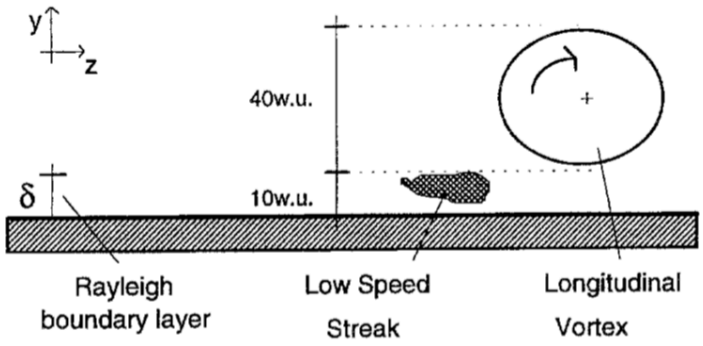


Figure 4.9: TDR mechanism through spanwise wall oscillation (Arturo and Quadrio, 1995)

The theory of Choi et al. (1998) also had its origin in the presence of the periodic Stokes layer generated by the spanwise wall oscillation. They argued that the Stokes layer introduced a spanwise vorticity component which induced an upstream velocity component in streamwise direction, no matter of the direction of motion (see fig. 4.10) and therewith decreased the wall-normal velocity gradient of streamwise velocity at the wall as conceptually drawn in fig. 4.11.

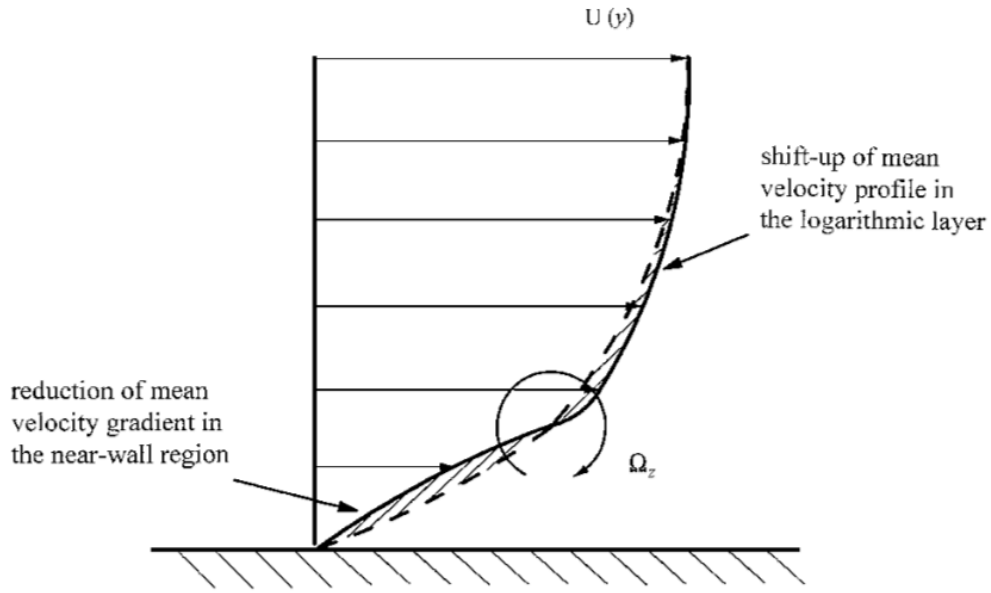


Figure 4.11: Conceptual model of TDR by spanwise wall oscillation (Choi et al., 1998)

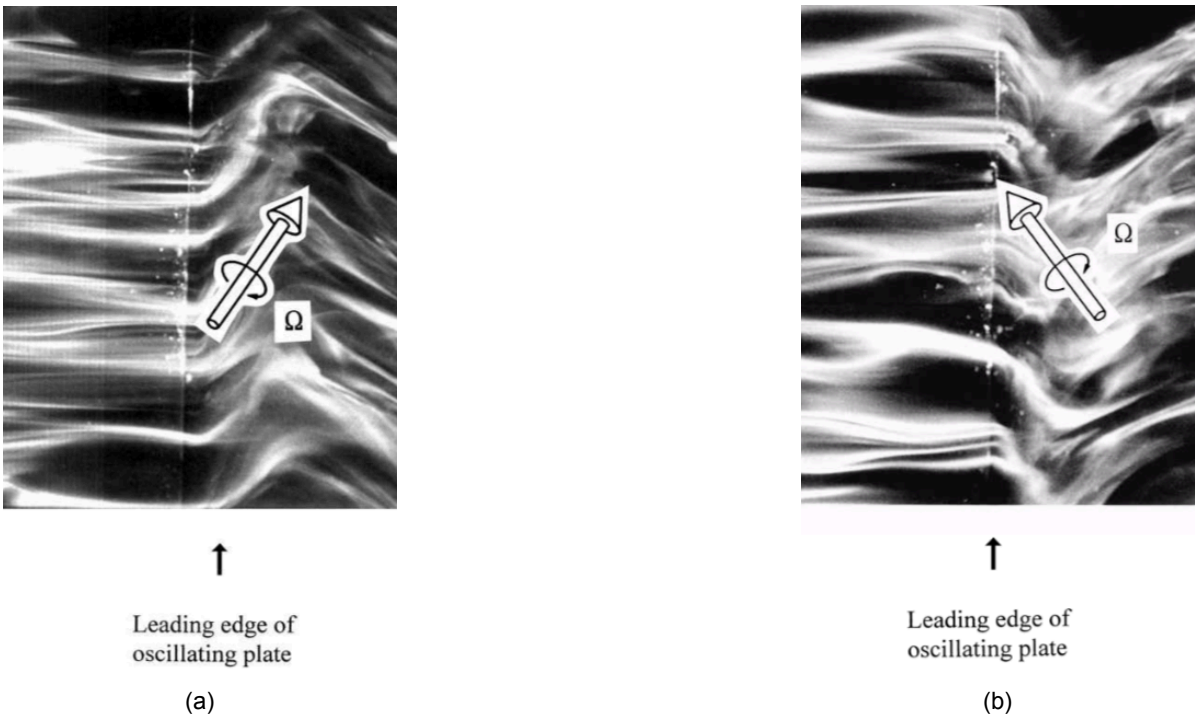


Figure 4.10: Flow visualizations at two motion directions of the plate (a) and (b) (Choi et al., 1998)

Further investigation of the TDR mechanism by spanwise wall oscillation in terms of coherent structures was undertaken by Kempaiah et al. (2020). The work documents on planar PIV data in the x-y plane visualizing vorticity from which vortex signatures can be seen in fig. 4.12. It was concluded that vortical structures in the outer layer were clearly discerned, however to construct a more detailed model in terms of coherent structures, a 3D experiment was proposed to fully visualize coherent structures.

However, the work performed by Kempaiah et al. (2020) was in confrontation towards the theories of Arturo and Quadrio (1995) and Choi et al. (1998). Kempaiah et al. (2020) argued that hairpins were less numerous under oscillation while the others argued that there is vorticity introduced to the flow.

As it will be seen in chapter 6 the tomographic measurement of this thesis also show reduced vorticity in all components. This gives rise to criticize the work of Arturo and Quadrio (1995) and Choi et al. (1998).

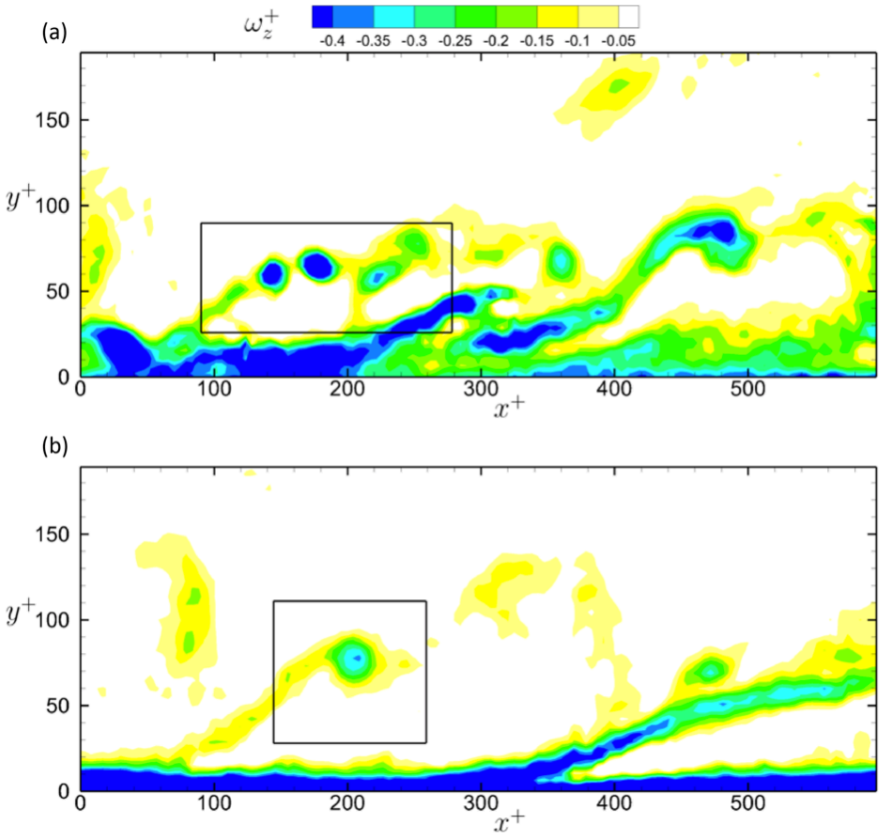


Figure 4.12: Vorticity visualizations of the (a) unoscillated case and (b) oscillated case showing hairpin signatures (Kempaiah et al., 2020)

## 4.6. Turbulent drag reduction quantification

This section serves as an overview of the maximum TDR percentages found by scientists up until now and their corresponding conditions (section 4.6.1) as well as studies which were not aimed to maximize the TDR percentage but investigated other phenomena, such as Reynolds number effects or net energy saving evaluation in section 4.6.2.

### 4.6.1. Studies documenting maximum turbulent drag reduction

Maximum TDR percentages are documented along with their governing oscillation parameters $A$ and $T^+$ respectively $f$, as well as boundary layer properties such as $Re_\theta$ or $Re_\tau$ depending on the type of flow investigated (TBL or TCF) in table 4.1. The number of articles documenting on the maximum TDR with the spanwise wall oscillation technique is surprisingly low. This in turn implies, that the initial finding by Jung et al. (1992) is widely accepted and was never challenged nor unproven until today.

| Name | Year | Re [-] | A [mm] | $T^+$ [-] | $f$ [Hz] | TDR [%] | Type |
|---|---|---|---|---|---|---|---|
| Jung et al. | 1992 | $Re_\tau$= 200 | $\frac{0.8Q_x}{2h}(28mm)$ | 100 | - | 40 | numerical |
| Choi et al. | 1998 | $Re_\theta$= 1,190 | 50 | - | 5 | 45 | experimental |

Table 4.1: Summary on research papers documenting on maximum TDR by spanwise wall oscillation ($Q_x$ is the streamwise flow rate and $h$ is the channel half width)

### 4.6.2. Studies investigating relevant parameters

Table 4.2 gives an overview of scientific work in the area of TDR through spanwise wall oscillation which all have a distinct research focus of great importance to understand this TDR technique. The findings of the papers are summarized in a paragraph following the table. Each paragraph treats one research focus.

| Name | Year | Research focus | Type |
|---|---|---|---|
| Laadhari et al. | 1994 | frequency dependence | experimental |
| Arturo and Quadrio | 1995 | amplitude dependence | numerical |
| Ricco and Shengli | 2004 | Reynolds number effects | numerical |

Table 4.2: Summary on research papers documenting on parameter effects on TDR by spanwise wall oscillation

**Frequency dependence:** The work of Laadhari et al. (1994) focused on studying the impact of oscillation frequency on the TDR % and found in general that an increase in oscillation frequency triggered a higher TDR %. The paper showed this effect in a graph which gave the streamwise wall-normal velocity gradient which decreased with increasing frequency (fig. 4.15a).

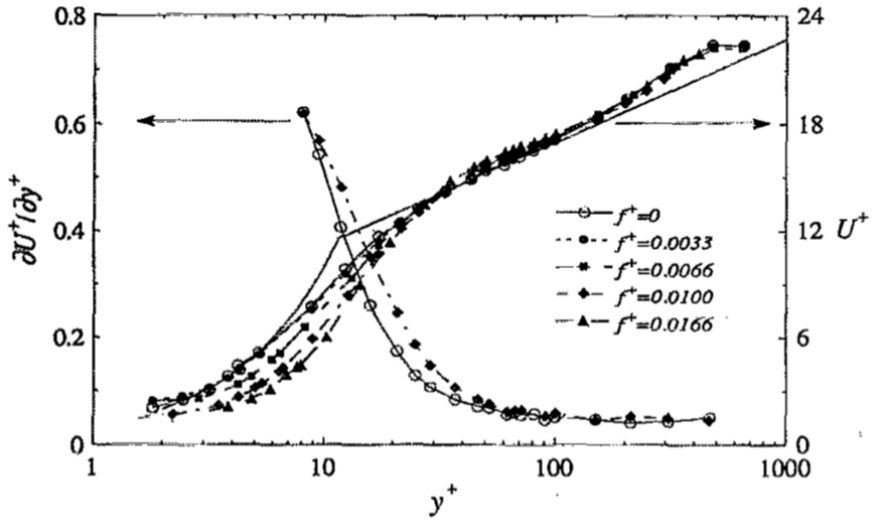


Figure 4.13: Frequency dependence of the mean velocity profile (Laadhari et al., 1994)

**Amplitude dependence:** The dependence of the amplitude on the TDR was first researched by Arturo and Quadrio (1995) who calculated the power saving through TDR rather than a direct drag measurement and found that the energy saved increased with increasing amplitude as shown in fig. 4.14.

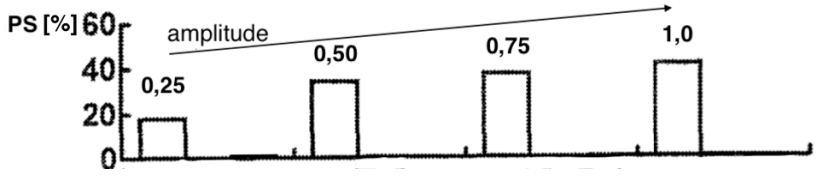


Figure 4.14: Power saving (PS) of TDR by spanwise wall oscillation for changing amplitudes (Arturo and Quadrio, 1995): Amplitude given as fractions of $\frac{Q_x}{2h}$, where $Q_x$ is the streamwise flow rate and $h$ is the channel half width

**Reynolds number effects:** As compared to the amplitude and frequency effects there is little investigation of the Reynolds number effect in air flows. However Ricco and Shengli (2004) conducted

an experiment in a water tunnel testing at Reynolds numbers $Re_\theta$ between 500 and 1,400 and documented on the TKE production and the % TDR found as shown in fig. 5.13. It was concluded that there are no dramatic Reynolds number effects which gave an argument that the technique might be suitable in high Re-regimes, such as aviation as well.

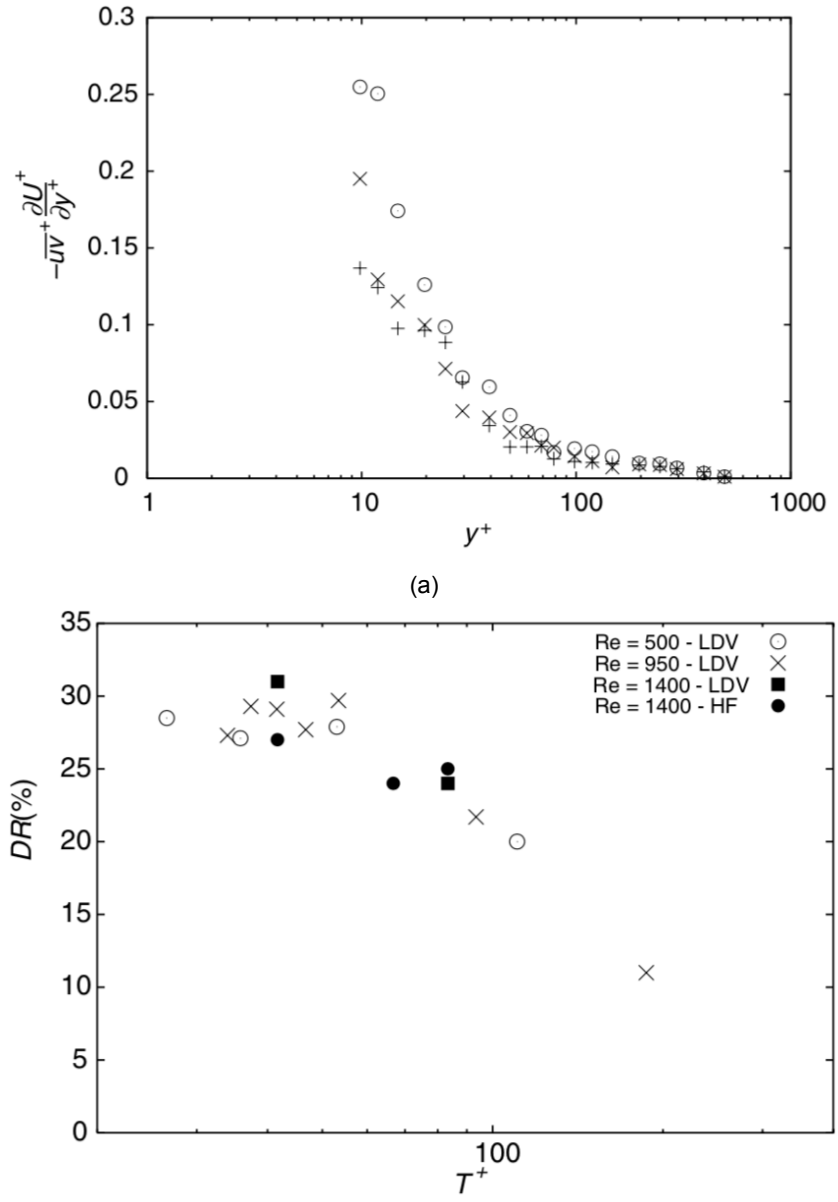


Figure 4.15: Reynolds number dependence of: (a) TKE production and (b) TDR (Ricco and Shengli, 2004)

## 4.7. Energy considerations

Finally, albeit having shown that TDR by spanwise wall oscillation is one of the most promising techniques when it comes to the amount of TDR which can be obtained, one must consider that it is an active technique and therefore in need of an energy input. This implies, that even if a 45 % TDR is reachable it has to be evaluated if the energy input to the actuation mechanism outweights the TDR saving in terms of energy. One early study by Arturo and Quadrio (1995) evaluated the net energy saving by subtracting the energy input required from the energy saved through TDR for different ampli-

tudes of the spanwise oscillation amplitude which is shown in fig. 4.16. The data clearly show that only a positive energy balance was reached when the amplitude was low and actually that at high TDR the net energy balance was highly unfavourable. This showed that next to the structural constraints of an oscillating plate, also the energy input is too high. Therefore, alternative actuation mechanisms such as plasma actuation need to be applied in order to get a larger positive net energy effect.

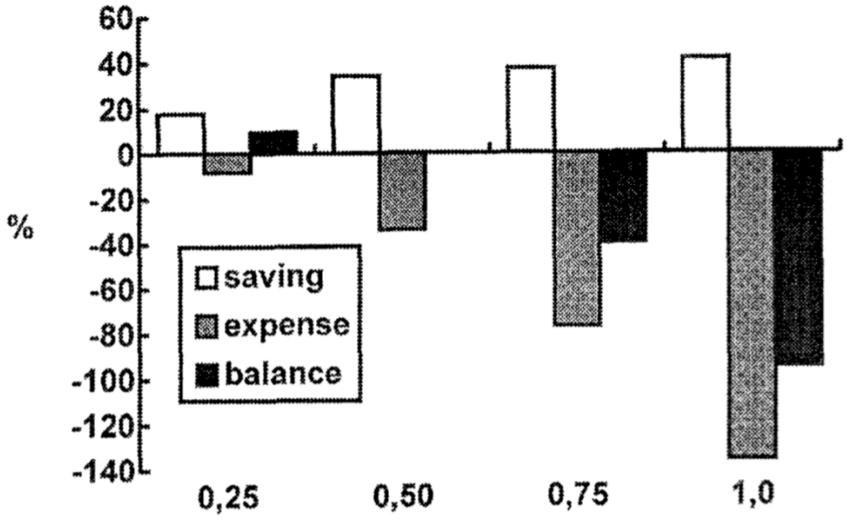


Figure 4.16: Net energy balance in the spanwise oscillated wall cases where the energy is given in % on the vertical axis and the amplitude is expressed on the bottom in terms of $\frac{Q_x}{2h}$ (Arturo and Quadrio, 1995)

## 4.8. Thesis research aim and objective

TDR by spanwise wall oscillation showed to decrease turbulence intensities and turbulence production as a main lever to reduce turbulent skin friction. Next to the maximum attainable TDR, it was discussed how sensitive the technique is towards changes in the input of the wall oscillation (frequency and amplitude) and how the TDR behaves for different Reynolds numbers. A huge gap and contradictory hypotheses were found in terms of the coherent structures TDR mechanism. Qaudrio et al. (2009) argued that the coherent structures are separated by the generated Stokes layer of the spanwise oscillating wall, Choi et al. (1998) argued that the actuation introduced a spanwise vorticity component which decreased the mean streamwise velocity gradient at the wall. Kempaiah (2019) showed reduced vorticity in the outer layer, however he argued that planar-PIV data were not sufficient to derive a full hypothesis of TDR mechanism. It became apparent that there is much light to shed in the area of understanding this mechanism. The tremendous need to understand this mechanism became obvious when the energy balance of the technique was considered as a whole. It is showed that only around 10 % net energy savings were obtained when the flat plate was actuated by a crankshaft system. There are alternative methods of actuation currently under study. One of the most promising methods is plasma actuation. This technique could result into a higher net energy effect as only spots are actuated which ultimately lead to the TDR.

This shows that a better understanding of the mechanism in terms of coherent structures could serve as an enabler to design a more energy efficient actuation mechanism as compared to the the oscillating flat plate. From this identified research gap, the following research question (plus sub-questions) arises which is aimed to be answered in the following thesis:

**How is the three-dimensional vortical mechanism of the TDR due to a spanwise oscillating flat plate related to the phase of the plate motion and can a descriptive/mathematical model relating the plate motion phase to the change of coherent structures in the TBL be defined?**

1. Is the oscillating wall affecting the coherent structures in the TBL?

(a) What is the number of coherent structures (streaks, hairpins, ejections, sweeps) in different phases of the plate motion found in the volume of view?

(b) What is the intensity and size of the coherent structures (streaks, hairpins, ejections, sweeps) in different phases of the plate motion found in the volume of view?

2. Can the plate motion phase be related to the coherent structure number, size and intensity?

(a) What kind of relationships can be established between the phase of the plate motion and number, intensity and size of the coherent structures?

(b) Is it possible to set-up a descriptive/mathematical model describing the changes in coherent structure number, intensity and size as a function of the plate motion phase?

# 5

# Experimental apparatus and procedures

This chapter describes the experimental facilities and set-up including the measurement system used. Furthermore, the data acquisition technique as well as data reduction and processing methods are explained. The wind tunnel, test section and actuation mechanism are presented in section 5.1 to section 5.3. The measurement method including the sampling and data reduction strategy is described in section 5.4. The chapter is closed with an uncertainty analysis of the results obtained from the tomographic reconstructions in section 5.5.

## 5.1. W-tunnel and flow conditions

The experiment was conducted in the low-speed W-tunnel at TU Delft in the faculty of Aerospace Engineering which facilitates a turbulence level of approximately 0.5 % (TU Delft, 2020). The W-tunnel is an open return low-speed tunnel with adjustable converging outlet sections. The tunnel has a contraction ratio of 9:1 and is powered by a 16.5 [kW] electrical motor reaching flow speeds up to 25 [m/s]. For the experiment a converging section resulting into a 0.4 [m] x 0.4 [m] outlet was used. Downstream of the contracting section, a rectangular wood channel of 1 [m] length was mounted (see also fig. 5.1). It included a pitot tube for dynamic pressure determination which was used to set the tunnel speed. The wood channel was extended by a 0.6 [m] long plexiglass section allowing for visual access. The two rectangular sections of constant cross-section ensured a quasi-zero pressure gradient flow. The tunnel was operated at a dynamic pressure of 5.51 Pa at 20 $^{\circ}C$ corresponding to a velocity of $U_e$ = 3 [m/s] resulting in a TBL of $Re_\theta \approx$ 1,000. These flow conditions were chosen following the work of Kempaiah (2019) as he used the same set-up and showed successful drag reduction for these flow conditions, which is an important note as the experiment was not designed to quantify TDR.

## 5.2. Test section

The test section was reused from the work of Kempaiah (2019) consisting of two wood plates and one carbon plate and a rectangular plexi glass channel as shown in fig. 5.2. The fixed main plate was 1.1 [m] long and was manufactured from wood. It was located in the constant rectangular W-tunnel outlet section spanning its whole width of 0.4 [m] and therefore embodied the most upstream plate section of the test section. The plate section was equipped with Lego bricks at the leading edge to trip the boundary layer and extended 0.1 [m] into the plexigass section which was immediately mounted to the W-tunnel outlet, thus connecting the wooden outlet to the plexiglass section. The plexiglass section had a cross-section of 0.4 x 0.4 [m] and therefore embodied a constant cross-section extension of the wind tunnel outlet, implying that the flow through the plexiglass section had a quasi-zero pressure gradient. The side walls of the section had two slits 0.1 [m] from the bottom, centred in streamwise direction. They were 0.4 [m] long and a carbon plate element was stuck through them. The carbon fibre plate was supported by bearings and had a 0.6 [m] span which allowed for spanwise movement of the carbon plate. Downstream of the carbon plate another 0.6 [m] long secondary stationary wooden plate was attached extending from the plexiglass section to the ambient thus constituting the outlet of the test section (see also fig. 5.1).

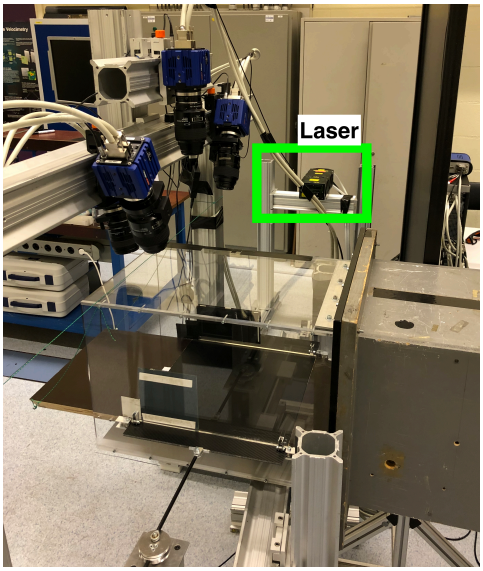


Figure 5.1: Test section set-up image from the actual experimental series, flow is from right to left

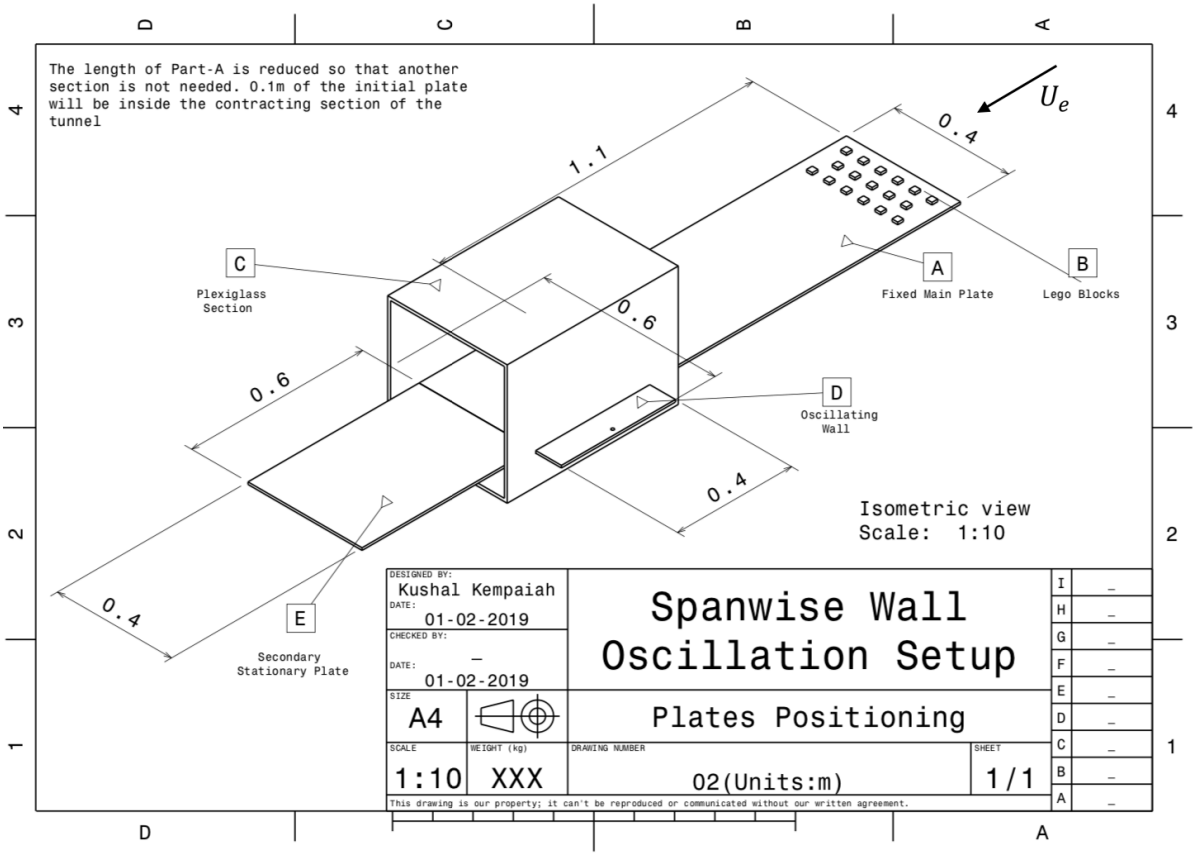


Figure 5.2: Oscillating wall test section, flow is from right to left (Kempaiah, 2019)

## 5.3. Actuation mechanism

The oscillating wall mechanism was also reused from the work of Kempaiah (2019). The mechanism oscillated the carbon plate in spanwise direction and consisted of a slider-crank system as shown in fig. 5.3 powered by a Maxon DC motor (Part number: 138690). Furthermore, the system was balanced by a sliding counterweight to reduce vibrations which might corrupt measurements. For the experiment,

the carbon plate was oscillated at 15 Hz which corresponds to a $T^+ \approx 100$, the condition where TDR is maximized as reported in literature (see section 4.6.1) for $U_e$ = 3 [m/s]. From the planar measurements of Kempaiah (2019), it was known that this wind tunnel setting corresponds to $Re_\theta \approx 1{,}000$ and a TDR of 14.63 [%].

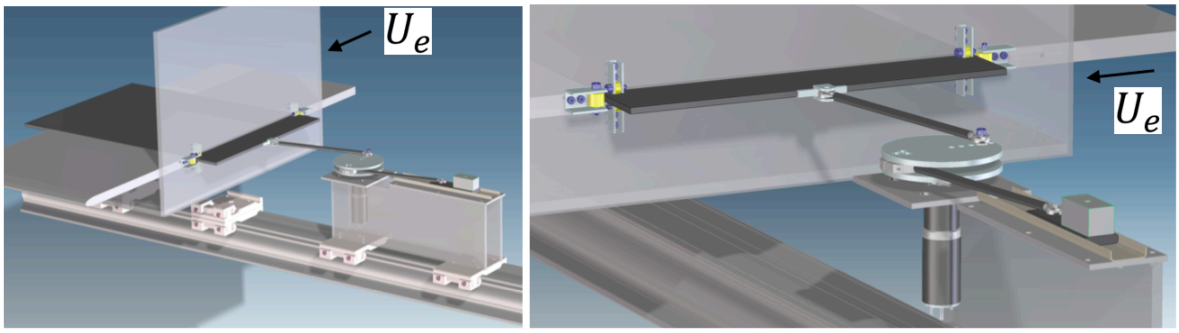


Figure 5.3: Slider-crank system used as actuation mechanism, not to scale, flow direction as indicated in the figure (Kempaiah, 2019)

## 5.4. Tomographic PIV

The tomographic PIV system used was manufactured by LaVision and the software to control the equipment was DaVis 8.4.0 by LaVision which outputs a 3D3C velocity field. The working principle of tomographic PIV consists of nine steps as shown in fig. 5.4 from seeding to 3D interrogation. The details of the steps are discussed in section 5.4.1 to section 5.4.6.

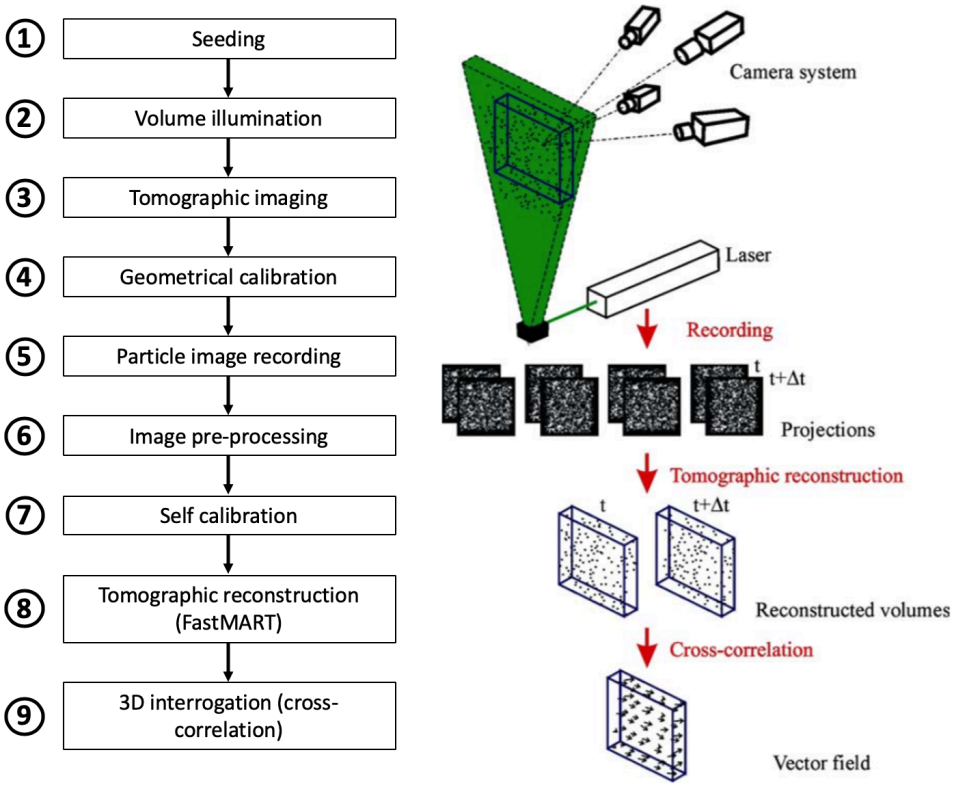


Figure 5.4: Tomographic PIV working principle (reproduced after Elsinga et al., 2006 and Raffel et al., 2018)

### 5.4.1. Seeding

Seeding is the process of introducing flow tracer particles into the flow. For this experimental series, spherical fog droplets with a diameter of 1 [$\mu$m] were used which were inserted through a SAFEX fog generator placed in the intake of the W-tunnel. In tomographic PIV it is essential to find a level of seeding which guarantees sufficient spatial resolution. However, the seeding density is limited by multi-scattering effects followed by a loss of contrast if the seeding density becomes too high. Raffel et al. (2018) showed that the seeding density can be increased with the number of cameras. This implies that more cameras ultimately lead to a higher spatial resolution. In this experiment, four cameras were used for which a ppp (particle per pixel) up to 0.05 yielded accurate reconstruction following Raffel et al. (2018). The ppp of the used particle images was approximately 0.02.

### 5.4.2. Volume illumination and tomographic imaging

The illumination and imaging set-up for the actuated test section is shown schematically in fig. 5.6. The laser and cameras were synchronized by a LaVision PTU. The goal of the illumination system was to illuminate the volume of view (VOV) shown in orange with a maximum uniform laser sheet of 10 [mm] thickness. The laser source was a double pulsed Nd:YAG Evergreen 200 laser from Quantel producing light at a wavelength of 520 [nm]. The pulse energy is 200 [mJ] and the maximum repetition rate was 15 [Hz]. The laser was placed parallel to the right hand side wall of the plexiglass section (see fig. 5.1, indicating laser position) in flow direction and produced a beam of 6.35 [mm] which was expanded horizontally and vertically through negative cylindrical lenses. This set-up resulted into a laser sheet of slightly more than 10 [mm] thickness at the side wall of the plexiglass section. The sheet was cut off at 10 [mm] height through a knife-edge filter at the inlet side of the plexiglass section and reflected through a mirror on the opposite side to increase the illumination intensity in the volume of view (Ghaemi and Scarano, 2010).

The VOV dimensions along with the sign convention are given in fig. 5.5. The dimensions were 60 [mm] · 60 [mm] · 10 [mm] (x · y · z). The right-handed frame of reference is centred in the bottom plane of the VOV. Its axes define the velocity components $u$, $v$ and $w$, where $U_e$ is aligned with the x-axis.

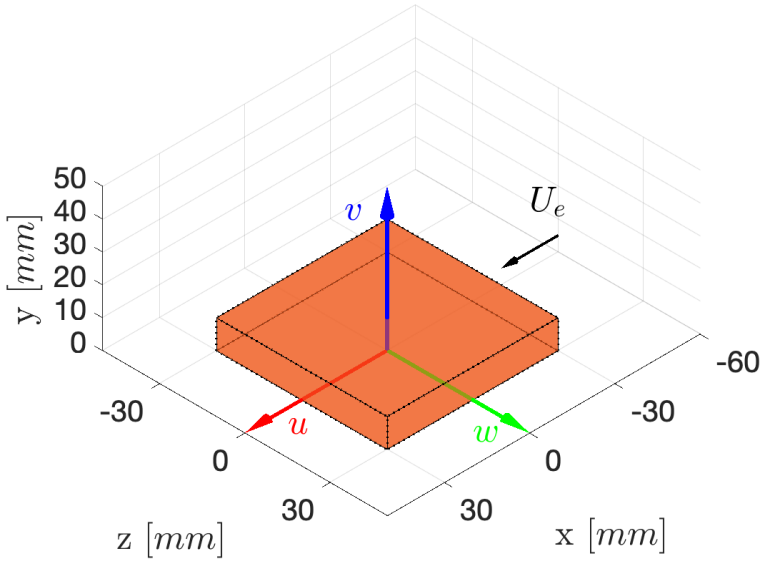


Figure 5.5: Dimensions and sign convention of the VOV giving the velocity convention (blue, green and red arrow) and spatial coordinates (x, y and z) on the black axes

The imaging system used four low speed sCMOS cameras with 2560 x 2160 pixels of 6.5 [$\mu$m] size. This kind of camera is very sensitive as every pixel has a storage capacity of 16 bits, implying that 65536 intensity levels can be distinguished. Cameras one to three (fig. 5.6) were mounted along a circular arc having its origin in the VOV and spanning an angular aperture of 58°. The fourth camera

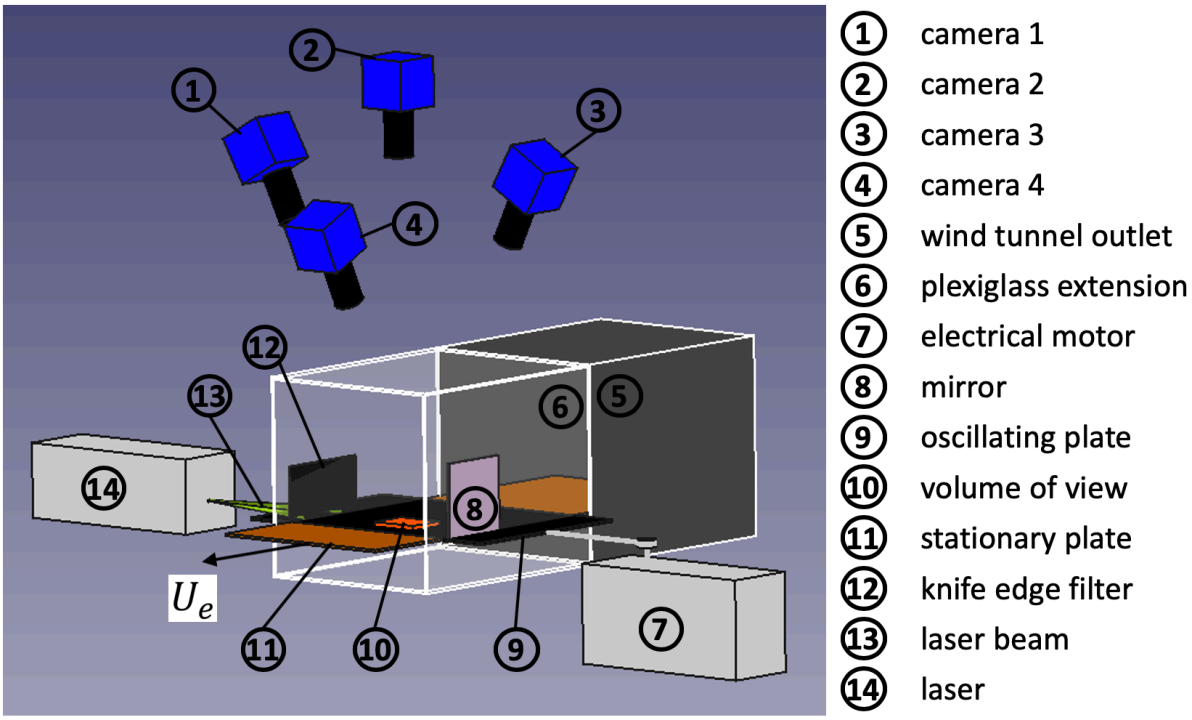


Figure 5.6: Illumination and imaging set-up

was mounted in the same x-z plane as camera two subtending an angle of 25° with respect to camera two. The camera set-up of a tomographic PIV experiment is quite complex and must meet certain requirements to guarantee a clean reconstruction as stated hereafter :

1. The maximum of the x and z dimension (x = 83 [mm]) of the camera field of view (not to be confused with the VOV) and the camera pixel number and size determine the magnification factor as calculated in eq. (5.1). The magnification also indirectly determines the focal length ($f$) of the lenses based on their mounting distance from their focal plane.

$$M = \frac{2560 \cdot 6.5 \cdot 10^{-6} m}{0.083 m} = 0.2 \tag{5.1}$$

2. All cameras spanning an angle with the $y$-axis have a Scheimpflug adapter between the camera and lens which is set to an angle which rotates the focal plane parallel to the carbon plate. The Scheimpflug angle $\Theta$ is a function of the magnification factor $M$ and the angle of the line of sight subtended with the $y$-axis ($\beta$) as given in eq. (5.2).

$$\Theta = \tan^{-1}(\tan(\frac{\beta}{2})\frac{M}{M+1}) \tag{5.2}$$

3. The focal plane of all cameras lies in the center of the VOV at its half height y = 5 [mm]. The required focal depth $dz$ to focus the whole VOV determines the $f_\#$ of the cameras as given in eq. (5.3). It was calculated that a $f_\#$ of 12 is needed to reach a focal depth of 10 [mm].

$$f_\# = \frac{\sqrt{dz} \cdot M}{\sqrt{4.88\lambda}(1+M)} \tag{5.3}$$

4. The total image particle diameter should be at least twice the pixel pitch of the camera to prevent pixel locking. For $M$ = 0.2 and $f_\#$ = 12, the effective image particle diameter is found to be 17 $\mu$m, thus more than 2 · 6.5 [$\mu$m] which implies that pixel locking will not occur in the set-up.

The described requirements and geometrical constraints such as that the lenses can not penetrate the plexiglass or the line of sight can not pass through the edges of the plexiglass section yielded the camera specifications given in table 5.1.

| | **x** [m] | **y** [m] | **z** [m] | $\mathbf{M}$ [-] | **f** [mm] | $\mathbf{f}_{\#}$ [-] | Θ [°] |
|---|---|---|---|---|---|---|---|
| **Cam 1** | 0.1 | 0.61 | 0.35 | 0.2 | 120 | 12 | 4.8 |
| **Cam 2** | -0.1 | 0.7 | 0.1 | 0.2 | 109 | 12 | 0 |
| **Cam 3** | 0.1 | 0.6 | -0.35 | 0.2 | 120 | 12 | 4.8 |
| **Cam 4** | -0.1 | 0.44 | 0.1 | 0.2 | 65 | 12 | 3.3 |

Table 5.1: Camera specifications for all four cameras giving the position in space (x,y,z), magnification factor ($\mathbf{M}$), focal length (**f**), f-stop ($\mathbf{f}_{\#}$ ) and Scheimpflug angle (Θ)

### 5.4.3. Geometrical calibration

The camera system was geometrically calibrated using a type 10 calibration plate from LaVision. During the calibration process, the carbon wall was removed from the set-up and the calibration plate was placed at three different x-z planes in the VOV. The first position was at the position of the wall (y = 0 [mm]), the second position at the center of the VOV (y = 5 [mm]) and the third position at the top of the VOV (y = 10 [mm]). At each position a single image of the calibration plate was taken with all cameras. After manually marking the calibration plate dots in DaVis a mapping function was determined for each camera which mapped the coordinates in the camera frame of reference on the reference frame defined by the calibration plate. To get an idea of how a calibration plate looks like, fig. 5.7 shows a type 11 calibration plate manufactured by LaVision.

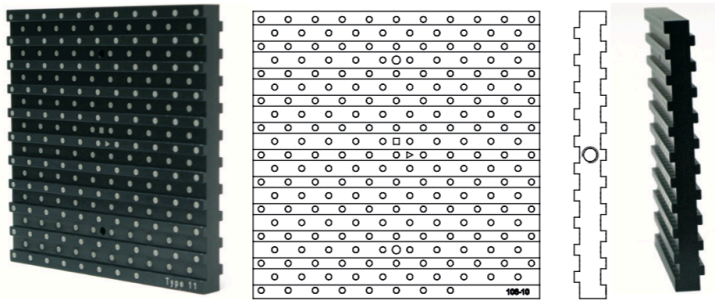

Figure 5.7: Sample calibration plate from LaVision (figure adapted fromLaVision, 2019)

### 5.4.4. Particle image recording

For the low speed particle image recordings, the laser was double pulsed at maximum 15 [Hz] with a pulse separation of 100 [$\mu s$] resulting in maximum particle displacement of 33.8 pix following eq. (5.4). As a rule of thumb, this value should not exceed $\frac{1}{4}$ of the interrogation box edge dimension.

$$\Delta x_{particle_{max}} = \Delta t \cdot U = 100 \cdot 10^{-6}[s] \cdot 2.2[m/s] = 0.00022m = 33.8pix \tag{5.4}$$

Acquisitions of the stationary plate were taken at a sampling frequency $f_{acq}$ of 15 [Hz]. In the actuated case, $f_{osc}$ was set to 15 [Hz] ($T^+ \approx 100$) and $f_{acq}$ was set to 13.85 [Hz]. The values for $f_{osc}$ and $f_{acq}$ were chosen as they resulted in the stroboscopic effect sampling at eight phases during one cycle of wall oscillation as shown in fig. 5.8. These phases were named by the speed of the plate ($HS$ = high speed, $IS^-$ = intermediate speed (- for deceleration), $LS$ = low speed, $IS^+$ = intermediate speed (+ for acceleration)). As the motor of the wall actuation was not synced with the illumination and imaging system, specific sampling phases can not be controlled. However, using this effect it was guaranteed that each quarter of a pi contains one sampling phase. This is important as these acquisitions serve as a data base for phase dependent phenomena. Furthermore, as tomographic PIV is computationally expensive in terms of volume reconstruction and cross-correlation, image processing was performed for one sequence of $HS$, $IS^-$, $LS$ and $IS^+$. This was done to save computation time as these phases contain the whole physics to investigate the mechanism. The resulting sampling positions are also

given in fig. 5.8 by the red circles. Their size indicate that there was some phase scattering in the acquisitions due to lack of precision of the motor. Scattering was found to lie within $\pm$ 0.25 [mm] for all plate motion phases corresponding to $\pm$ 0.25 [Hz]. The phase was indicated by a small piece of tape on the oscillating plate and a reference millimetre paper on the downstream stationary wooden plate. This indicator was captured by the field of view of at least one camera.

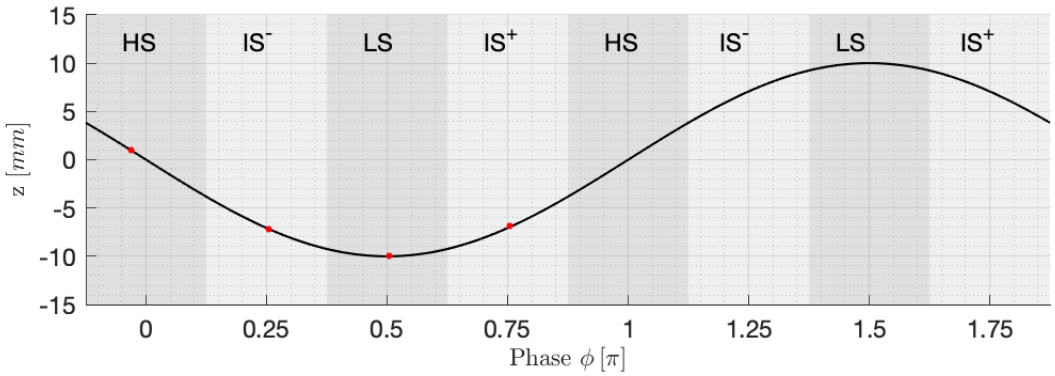


Figure 5.8: Phasewise discretisation of the plate oscillation including a measure of the phase scattering represented by the red dots

### 5.4.5. Image pre-processing

After the particle image recording, the background noise and reflections needed to be removed from the raw images. The background noise level was a result of light being scattered by elements of the test set-up other than the fog droplets. These intensities were usually lower than the intensities of the particles. The so called wall reflection was an exception of small regions which scatter a lot of light and appear much more intense than the particles. Figure 5.9 shows the raw image including the background noise appearing as the light grey shade in the image and wall reflections appearing as large red dots in the domain (implying saturation). The background noise was removed by subtracting the sliding mean intensity level using a filter width of three images. Following this filter operation the DaVis built in image pre-processing filter for tomographic-PIV was applied which subtracts the sliding spatial minimum of 3 pix and applies a Gaussian smoothing followed by a sharpening operation. The resulting pre-processed image is shown in fig. 5.10 where the particles are clearly recognizable.

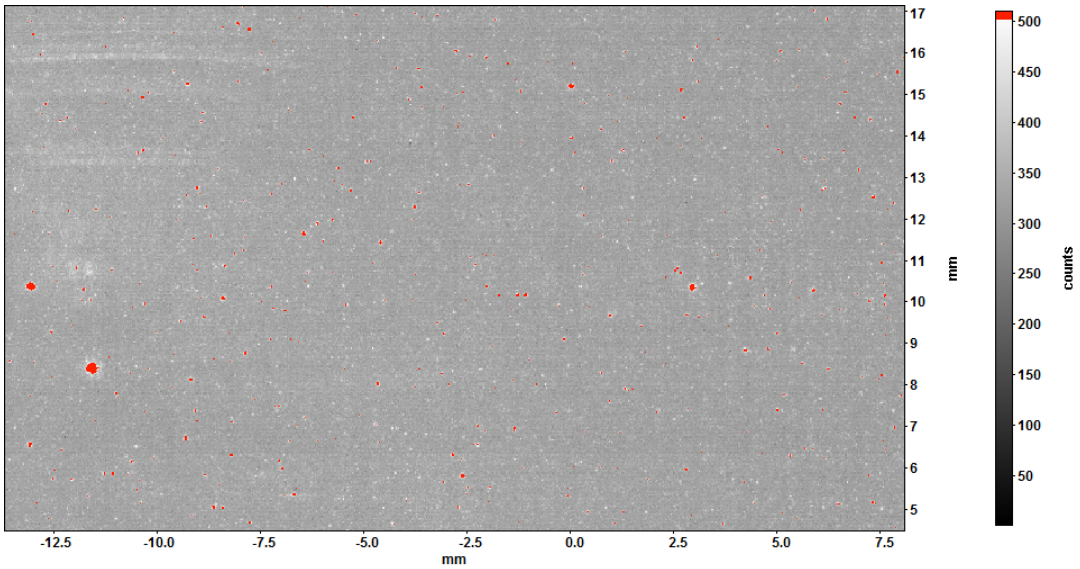


Figure 5.9: Raw image

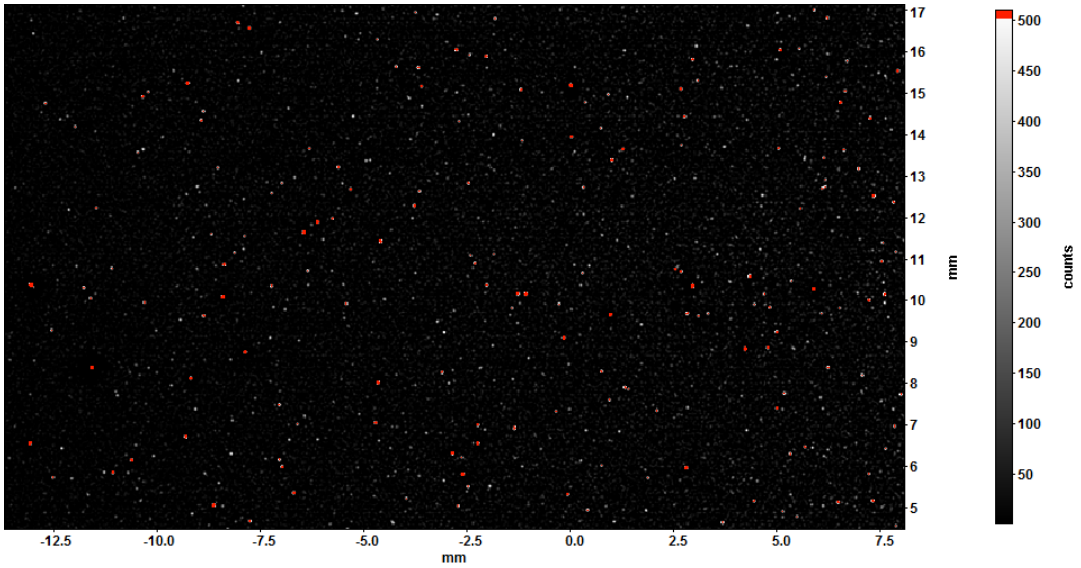


Figure 5.10: Pre-processed image

### 5.4.6. Self calibration, tomographic reconstruction and 3D cross-correlation

Raffel et al. (2018) argue that any error in the calibration propagates in the volume reconstruction. Therefore, a so called ”self-calibration” is recommended which corrects the geometrical calibration. In other words, the geometrical calibration is not accurate enough for a high quality volume reconstruction. The disparity between the geometrical calibration and the self-calibration determines the correction function for the geometrical calibration. The disparity map is determined from the particle images via an algorithm (for more details see Wieneke, 2008) and applied to the geometrical calibration.

Once the self-calibration had been applied, the particle positions in the VOV were reconstructed from the pre-processed particle images (see also fig. 5.4). This process is called volume reconstruction and determines the particle positions in space from the raw images. For the volume reconstruction the FastMART algorithm with 6 iterations was used (for more details see Herman and Lent, 1976). The value of 6 iteration was chosen as result of a cost-accuracy trade-off. Novara et al. (2010) showed that the reconstruction quality is improved by only 1.4 % when increasing iterations from 6 to 10. Once the volume was reconstructed, the signal to noise ratio (SNR) of the domain was derived from the intensity distribution. In this process, the minimum intensity in the wall region of the volume was assumed to be the background noise level. From this the SNR was determined by eq. (5.5). The reconstructed average intensity in wall-normal direction is shown in fig. 5.12. In this figure, the position of the wall is clearly recognized by an intensity peak at y = 0 [mm]. The region between y = 0 and 1.8 [mm] (shaded in grey) show another peak, which probably originated from a reflection caused by components of the test set-up. These reflections corrupt the data and therefore they must be treated with care, as they introduce regions of high intensity which are not physical particles. The region between y = 1.8 to 8.9 [mm] showed to have an average SNR (signal to noise ratio) of 2 with a minimum of 1.5. At y = 8.9 [mm] the intensity dropped as the laser power decreases. Therefore, all data points above y = 8.9 [mm] suffered from a poor SNR and are therefore shaded in grey as well.

$$SNR = \frac{I(y)}{I_{min}} \tag{5.5}$$

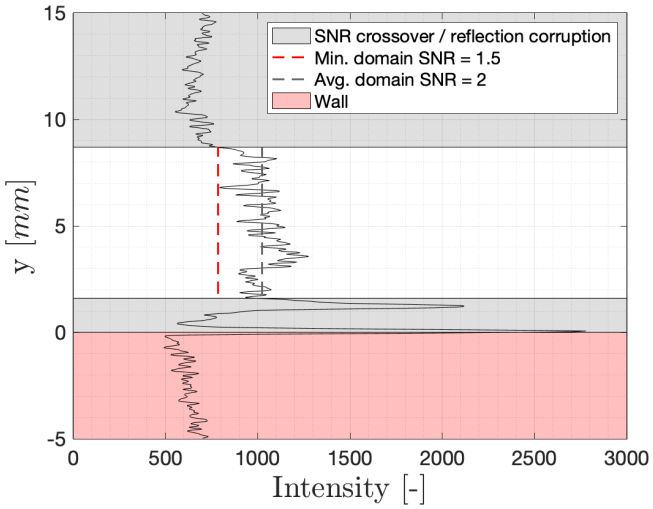


Figure 5.11: Intensity distribution across the VOV indicating the wall and regions of sufficient and low SNR

In the last step, the reconstructed volume is cross-correlated in 3D to determine the 3 dimensional velocity field with 3 components. The settings of the cross correlation were fine tuned to find a trade-off between affordable computational time and acceptable accuracy and spatial resolution of the resulting velocity fields. These settings resulted in an interrogation box size with edge length of 2 mm. 75 % overlap is motivated by the work of Tokgoz et al. (2012) who showed that velocity gradient results are more accurate for higher overlap ratios.

| | Size [voxel] | Shape | Overlap [%] | Peak search radius [voxel] | Volume Binning | Passes |
|---|---|---|---|---|---|---|
| Step 1 | 96 | 1:1 | 75 | 16 | 8x8x8 | 2 |
| Step 2 | 64 | 1:1 | 75 | 8 | 4x4x4 | 2 |
| Step 3 | 64 | 1:1 | 75 | 4 | 2x2x2 | 2 |
| Step 4 | 64 | 1:1 | 75 | 2 | no | 2 |
| Step 5 | 32 | 1:1 | 75 | 1 | no | 2 |
| Step 6 | 24 | 1:1 | 75 | 1 | no | 2 |

Figure 5.12: Fine tuned cross-correlation settings as used for the results presented in chapter 6

## 5.5. Uncertainty analysis

Uncertainty analysis is an important domain when analysing experimental results as it gives insights on their accuracy. This is important to be aware of when deriving hypotheses and conclusions based on the results. Uncertainty analysis distinguishes between systematic and random errors. Random errors are discussed in section 5.5.1 and indicate the level of measurement precision, while section 5.5.2 gives an overview of systematic errors indicating measurement accuracy. It shall be noted that it is not the aim of this section to quantify uncertainty distributions (therefore called analysis) for ever variable throughout the domain. It is rather intended to describe and mention which regions are most affected by uncertainty. This prevents conclusion being based on measurement errors rather than measured physics.

### 5.5.1. Random errors

Statistical errors are of random nature and play a vital role in uncertainty analysis of averaged parameters in experimental methods. To determine the statistical error of the mean velocity with a confidence

level of 95 %, eq. (5.6) was used resulting in a wall-normal error distribution as given in fig. 5.13b. The error for N = 5000 samples showed that it was bound below 1 % within the whole domain. The sampling locations where chosen through a grid in the volume where the points were spaced 2 mm apart, thus spaced by the edge length of an interrogation box. For this error analysis these sampling strategy was assumed to result in uncorrelated samples, allowing for the method chosen. For the A further check was to see if the variables converge. The convergence curves of the streamwise velocity are given in fig. 5.13a for three different wall-normal positions which showed to be clearly convergent.

$$\epsilon_{\overline{u}} = 1.96 \frac{\sigma_{\overline{u}}}{\sqrt{N-1}} \tag{5.6}$$

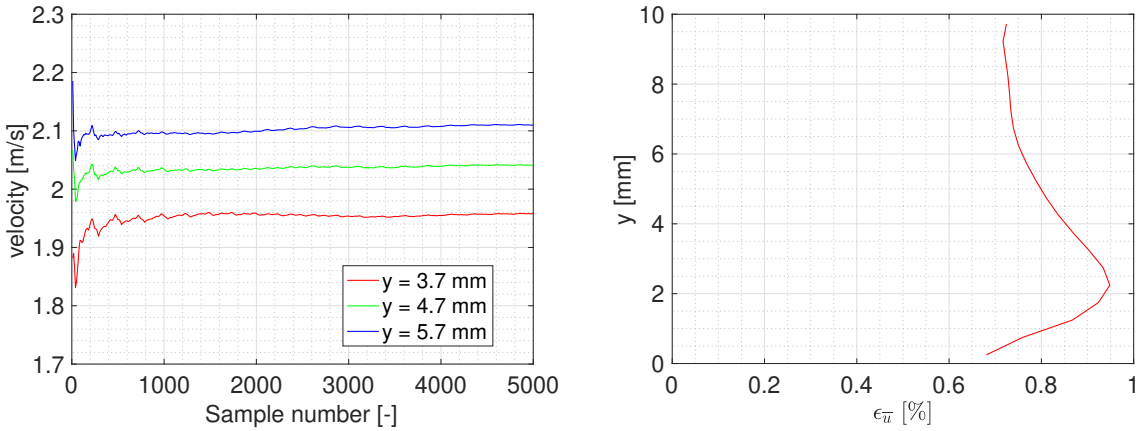


(a) (b)

Figure 5.13: (a) Convergence plot of streamwise velocity at different wall-normal positions (b) statistical error of streamwise velocity mean for N = 5000

Next to the statistical random error shown in fig. 5.13b, there exists a so called noise-floor in tomographic PIV which stems from various possible sources. These are the degree to which tracer particles follow the flow, non-uniform particle scattering, image distortion and aberration, uneven illumination, reflections, background intensity, CCD noise and loss of particles during two subsequent exposures (Atkinson et al., 2011). The authors of the article argue that it is yet unsolved to determine the errors due to the individual contributions. However, they determined the general random noise present in PIV measurements without a breakdown in separate sources. For a turbulent boundary layer, a noise level of 0.5 pixels is reported for velocity components resulting in an error given in eq. (5.7). This error would translate to an overestimation of velocity fluctuations which is not seen to this extend. This implies that either the estimation is too conservative or the error is balanced by other phenomena.

$$\epsilon_{vel} = \frac{0.5pix \cdot 6.5 \cdot 10^{-6} \frac{m}{pix}}{100 \cdot 10^{-6} s} = 0.035 \frac{m}{s} \tag{5.7}$$

The presence of ghost particles affect velocity gradients most severe, imposing random errors on the vorticity (Atkinson et al., 2011). An estimation of the error in vorticity can be obtained by evaluating the divergence of the velocity field as defined in eq. (5.8).

$$div(U) = \frac{\partial u}{\partial x} + \frac{\partial v}{\partial y} + \frac{\partial w}{\partial z} \tag{5.8}$$

As the measured flow was incompressible, an error free measurement volume would yield 0 divergence at every point in the VOV. Following the argumentation of Scarano and Poelma (2009) the maximum vorticity error can be estimated by one standard deviation of the divergence error distribution given in fig. 5.14. It shows a Gaussian error distribution with $\sigma_{div}$ = 170. If $\sigma_{div}$ is assumed to be the error magnitude and a typical vorticity magnitude in the near wall region reaches 1000 [1/s] (see fig. 5.15,

showing only the spanwise as the other components are ≈ 0 as shown in appendix A.1) the maximum error on vorticity can be approximated to be 17 [%]. This clearly shows that measuring gradients is one of the most severe weaknesses of tomographic PIV.

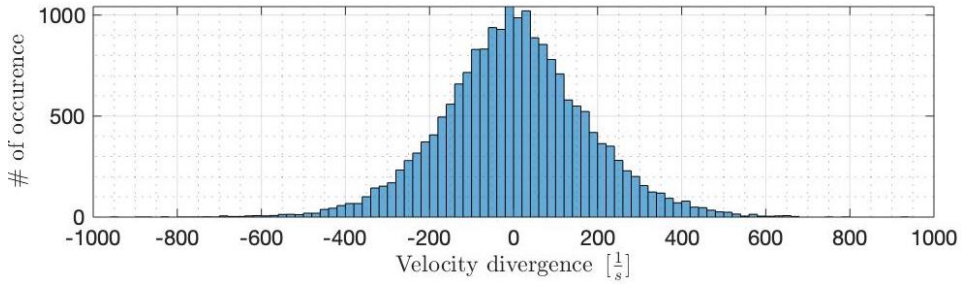


Figure 5.14: Divergence distribution in a sub volume of the VOV ranging from x = -10 to 10 [mm], z = -10 to 10 [mm] and y = 2 to 8 [mm]

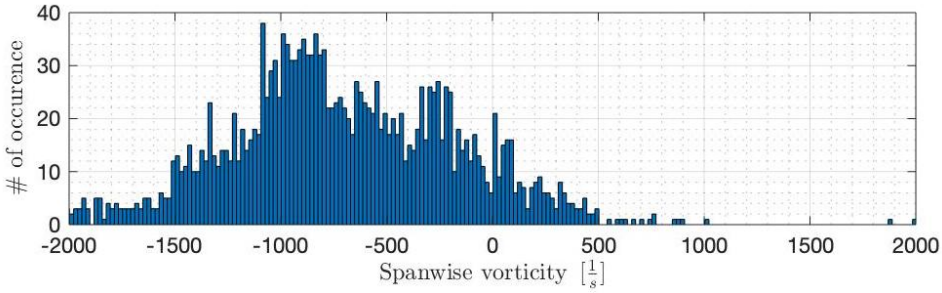


Figure 5.15: Spanwise vorticity from x = -10 to 10 [mm], z = -10 to 10 [mm] and y = 2 to 8 [mm]

### 5.5.2. Systematic errors

The first systematic error discussed is the averaging effect. Tomo PIV uses interrogation boxes to reconstruct the flow fields which govern the range of scales being resolved. The interrogation box can be regarded as a low pass filter with the filter width being the edge length of an interrogation. For the variables this implies that they suffer from an averaging error. For converging quantities such as the mean velocity and vorticity. This error can be quantified from data of higher resolution as shown in fig. 5.16 as indicated by the error bar.

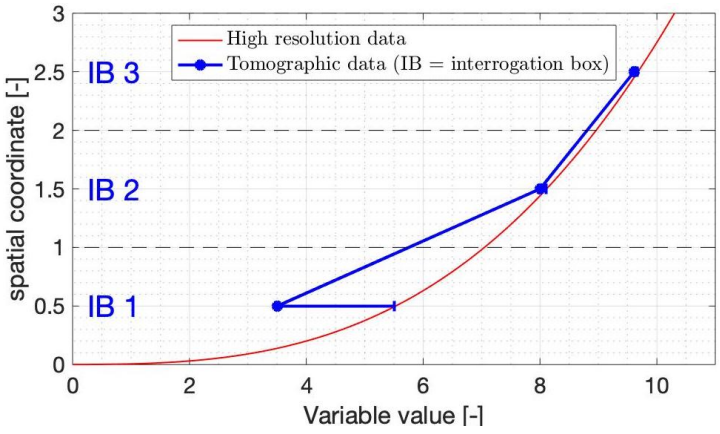


Figure 5.16: Averaging error of converged quantities using fake data suitable to show the effect

Of course a lack of resolution has an effect on non-converging properties such as RMS values as well. However, to quantify this error, very well resolved data sets are needed such as LES or DNS

results and is therefore considered to be beyond the scope of the present work.

Next to the averaging error, a systematic underestimation of large velocity fluctuations by tomographic PIV is found (Atkinson et al., 2011) ranging from 0.2 up to 1.5 pix. Here it shall be noted that these estimations are dependent on the measured flow and on the wall-normal position. In general it can be said that underestimations of velocity peaks increase in the regions of large velocity gradients up to 1.5 pix (Atkinson et al., 2011). The maximum error on velocity fluctuations found by (Atkinson et al., 2011) is 1 pix. In this experiment, 1 pix resulted in fluctuation RMS error as given in eq. (5.9). This agrees with the maximum underestimation found in the tomographic velocity fluctuation RMS. The value of 0.085 [m/s] corresponds to a maximum error percentage of 30 % for velocity fluctuations.

$$\epsilon_{velfluc} = \frac{1pix \cdot 6.5 \cdot 10^{-6} \frac{m}{pix}}{100 \cdot 10^{-6} s} = 0.085 \frac{m}{s} \tag{5.9}$$

### 5.5.3. Error propagation in derived quantities

The errors discussed so far are applicable to velocity distributions and their spatial derivations (vorticity). However, Reynolds stresses and TKE production are very import quantities in the domain of TDR. To analyze their errors, the error propagation theory was used which determined the error of a quantity by the errors of its multiplicatives as given in eq. (5.10) where $\epsilon$ is the error and V is the magnitude of the corresponding variable. Propagated errors in $Re_{12}$ reach up to 100 [%] for the oscillated case at y = 1.8 [mm]. The maximum error in the TKE production reaches up to 110 [%] in the peak locations as a result of velocity gradient errors and the Reynolds stress error.

$$\frac{\epsilon_{derived}}{V_{derived}} = \sqrt{\left(\frac{\epsilon_1}{V_1}\right)^2 + \left(\frac{\epsilon_2}{V_2}\right)^2} \tag{5.10}$$

# 6

# Results and discussion

This chapter presents the results of the tomographic PIV measurement campaign in terms of pointwise statistics in section 6.2 after introducing the canonical TBL in section 6.1. The tomographic data are complemented by the planar data of Kempaiah (2019) who measured the same TBL as was investigated in the present work. At this stage it is worth mentioning that based on the boundary layer characteristics found form the planar data by Kempaiah (2019), 1 mm corresponds to 10 dimensionless spatial units.

Section 6.3 makes use of the available three-dimensional instantaneous flow fields to analyse the characteristics of coherent structures in the stationary and oscillated case ($HS$, $IS^-$, $LS$, $IS^+$). Due to the quite erroneous gradient measurements detected in section 6.2, coherent structures analysis is limited to ejection/sweep events and high/low-speed streaks and doesn't contain vortical pattern recognition. Finally, the results and observations of section 6.2 and section 6.3 are used to formulate a descriptive model of the vortical mechanism in TBLs subjected to spanwise wall oscillation in section 6.4 which is well linked to general TBL theory as given in chapter 2.

## 6.1. Canonical turbulent boundary layer

The canonical boundary layer which is aimed to be reproduced in the experiment is fully turbulent. The mean velocity profile is shown in fig. 6.1. The TBL data used to validate the tomographic measurements are obtained by planar PIV in the work of Kempaiah (2019) and its properties are given in table 6.1. This boundary layer is chosen as it results in the largest TDR percentage under spanwise wall oscillation at $T^+ \approx 100$ as shown by Kempaiah (2019). The planar data available are the mean and fluctuating velocity ($u$,$v$), mean and fluctuating spanwise vorticity ($\omega_z$), Reynolds stress ($Re_{12}$) and the derived TKE production term.

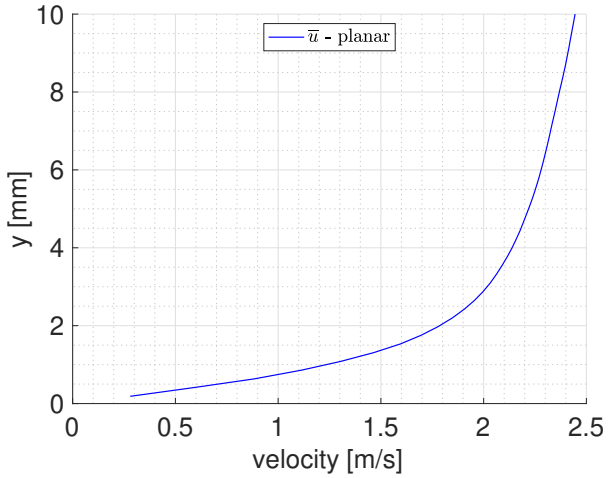


Figure 6.1: Canonical TBL with the properties of table 6.1 as measured by Kempaiah (2019)

| $Re_\theta$ [-] | $U_e$ [m/s] | $\delta_{99}$ [mm] | $\delta^*$[mm] | $\theta$ [mm] | $u_\tau$ [m/s] | $y^+$ [mm] | $H$ [-] |
|---|---|---|---|---|---|---|---|
| 1,000 | 3 | 59.2 | 6.68 | 4.925 | 0.145 | 0.10 | 1.356 |

Table 6.1: Canonical TBL characteristics as given by Kempaiah (2019)

## 6.2. Pointwise statistics

Results in terms of pointwise statistics are broken down per flow quantity for better readability. Mean velocity and fluctuations are discussed in section 6.2.1 followed by mean and fluctuating vorticity in section 6.2.2. In section 6.2.3 Reynolds stresses and the production term of TKE is discussed. For the stationary case and for each oscillation phase ($HS$, $IS^-$, $LS$ and $IS^+$) 5,000 samples are used to determine pointwise statistics. The oscillated statistics presented in the remainder of the section are the average of the phases, thus containing 20,000 samples in total, while the stationary data contain 5,000. For simplicity only variables are discussed in this section which are known to be other than $\approx 0$ according to TBL theory. The interested reader finds the full set of pointwise statistics for the stationary case and the phases ($HS$, $IS^-$, $LS$, $IS^+$) in appendix A.

### 6.2.1. Velocity

The mean velocity profile components of the flow fields measured in the experiment are given in fig. 6.2a. Tomographic and planar data of the u-component are given for the stationary and 15 [Hz] ($T^+ \approx 100$) oscillated case.

Tomographic data are complemented by error bars originating from the averaging effect and statistical uncertainty (see section 5.5). It is immediately apparent that the tomographic profiles are shifted to the left indicating that $U_e$ was set to a value slightly lower than 3 [m/s] during the experiments. Nevertheless, common trends of the planar and tomographic profiles are observed. The wall-normal gradient of streamwise velocity is clearly decreased when the plate is oscillated in the region between y = 0 and 3 [mm]. Furthermore, exceeding y = 3 [mm], the mean velocity gradient is increased. This is a strong proof that the wall friction is decreased by spanwise wall oscillation for $T^+ \approx 100$ as it depends on the gradient only, assuming the fluid is of the same viscosity (compare eq. (2.13)). The changes imposed by wall oscillation onto the mean velocity gradients agree with the findings of the works of Jung et al. (1992) and Laadhari et al. (1994) presented in fig. 4.3. At this point it shall be noted that investigating the behaviour of coherent structures is the aim of this thesis rather than quantifying the TDR, justifying that the mean profile is not discussed further.

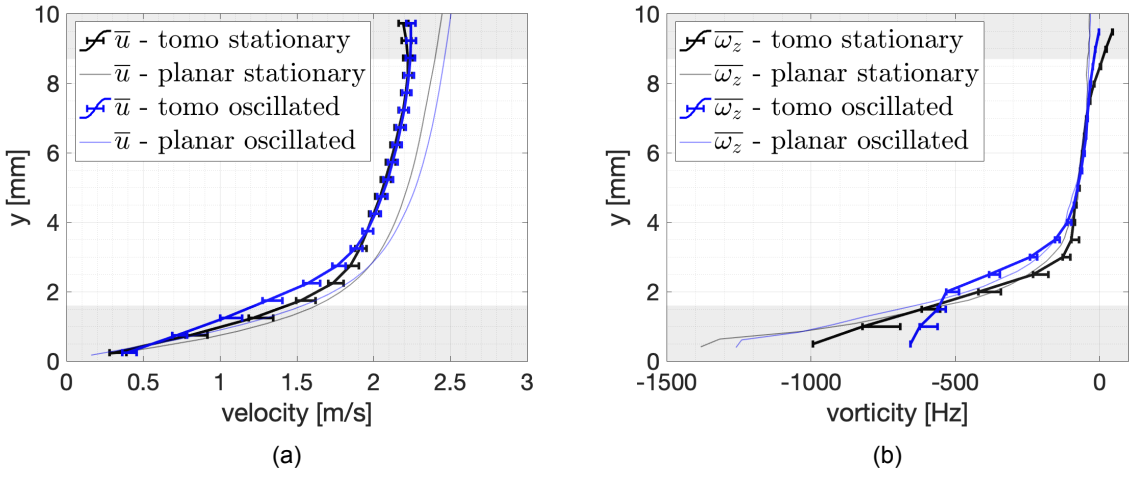


Figure 6.2: Stationary and phase-averaged ($HS$, $IS^-$, $LS$ and $IS^+$) TBL (a) mean velocity profile (b) mean vorticity profile (planar data adapted from Kempaiah, 2019)

Next to the mean velocity profile, velocity fluctuation RMS distribution are shown in fig. 6.3. These properties are important to discuss as they can be associated with specific coherent structures (compare section 2.4 and the work of Martins et al., 2019). Spanwise fluctuations show to have the highest

magnitude throughout the domain. They tend towards zero at the wall and increase rapidly in positive wall-normal direction to a peak in the region around y = 1.5 to 2.25 [mm]. From the peak location towards the free stream flow they tend to decrease asymptotically. The tomographic data reveal that wall oscillation decreases the magnitude of the $u'_{RMS}$ in the whole domain. The largest decreases is visible at the peak location. This trend is in line with planar reference data. Nevertheless the data expose one of the most severe weakness of tomographic PIV, as it tends to underestimate large velocity fluctuations. The length of the given error band in the fig. 6.3 corresponds to an error of 1 pix as discussed in section 5.5. Even that the tomographic data show large underestimations of the peak it can be concluded that wall oscillation attenuates streamwise velocity fluctuations which indicates less numerous and/or intense low and/or high-speed streaks.

The wall-normal component $v'_{RMS}$ shows to have the smallest magnitude of all components. It starts off at zero from the wall and shows a weak asymptotic increases towards the free stream flow. The data show that wall oscillation also attenuates wall-normal velocity fluctuation. However, tomographic PIV overestimates these fluctuations when compared to the reference planar data. This effect possibly stems from a less effective image pre-processing in the oscillated case leading to cross-correlation inaccuracies. However, decreased magnitudes indicate less numerous and/or intense sweep and ejection events (Martins et al., 2019) which are the main contributors to TKE production and therefore skin friction.

The spanwise velocity component RMS $w'_{rms}$ lies in between the magnitude of the spanwise and wall-normal component. Note that there are no planar reference data available as it is a two component measurement technique. The stationary data tend to zero at the wall while the oscillated data seem to approach a finite value due to the wall movement in spanwise direction. In positive wall-normal direction, the magnitude increases asymptotically to a value of 0.19 [m/s] and 0.17 [m/s] for the stationary and oscillated case, respectively. Away from the wall, the $w'_{RMS}$ can be linked to the presence and intensity of the streamwise vortices constituting the hairpin legs implying that their number of occurrence and/or intensity is attenuated. Next to the comparison with the results of Kempaiah (2019) the findings agree with pointwise statistics of Laadhari et al. (1994). It shows that the fluctuations of both stationary and actuated case are in order $u'_{rms} > w'_{rms} > v'_{rms}$. Furthermore, all components are decreased when the plate is oscillated. The maximum decrease is found in the $u'_{rms}$ term.

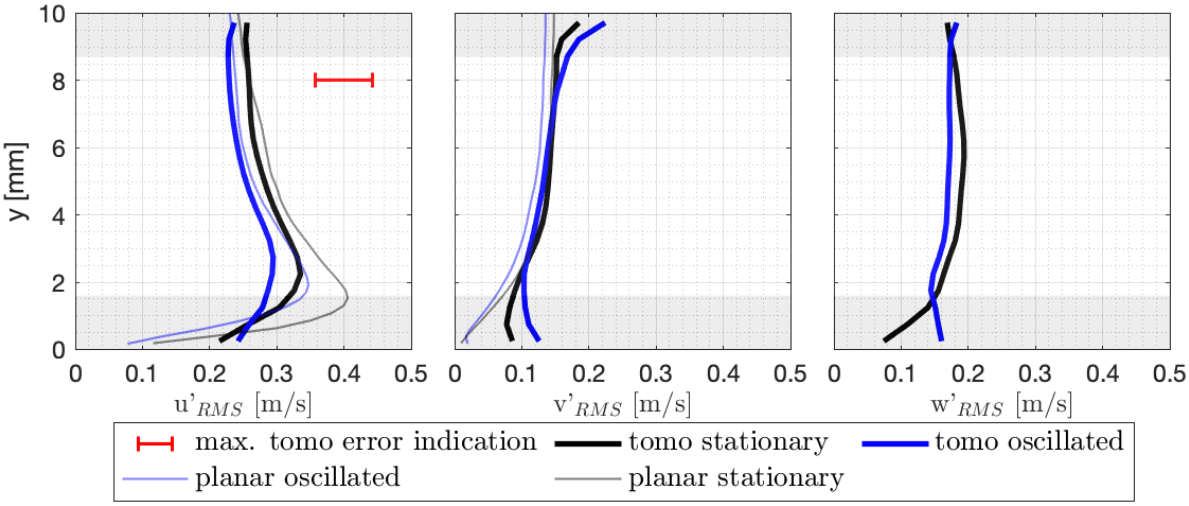


Figure 6.3: Stationary and phase-averaged ($HS$, $IS^-$, $LS$ and $IS^+$) TBL velocity fluctuation RMS (planar data adapted from Kempaiah, 2019)

### 6.2.2. Vorticity

The mean vorticity profile shown in fig. 6.2b is limited to the spanwise component as it is the only non-zero one. The errorbars give the averaging effect for mean profiles. It is derived that the stationary tomographic profile increases asymptotically towards the wall closely matching the planar PIV data between y = 1 [mm] and 8 [mm] apart from a small region at 3 [mm] where the vorticity is slightly un-

derestimated. The vorticity increases quasi-linearly from -1300 [Hz] to -100 [Hz] between y = 1 [mm] and y = 4 [mm] and then reaches a plateau which slowly decreases towards y = 8 mm to a finite value of -50 [Hz]. The oscillated tomographic profile shows differences with respect to the stationary profile in the near wall region between y = 0 and 4 [mm]. The region between y = 2 and 4 [mm] shows an upward shift of around 0.5 [mm]. Below 2 [mm] the profile shows a much smaller decrease in spanwise velocity as compared to the stationary case. However, especially the tomographic vorticity data show to be affected by a noisy signal below 2 [mm]. Nevertheless, oscillated tomographic and planar data both show to have lower vorticity towards the wall, but a slightly elevated level between y = 2 to 4 [mm] when compared to the stationary case. The drop in mean vorticity towards the wall indicates reduced turbulent skin friction. Here it shall be noted that the determination of vorticity is novel in this work as earlier works did not resolve the flow field in 3 dimensions and 3 components. Vorticity is a derived quantity from velocity which was found to agree well with earlier works. A special attention during uncertainty analysis was given to vorticity as there are little reference values.

Analysing the vorticity RMS profiles in fig. 6.4 provides indications of vortical structures in the stationary and oscillated turbulent boundary layers. Connecting to section 2.4 vorticity fluctuation components can be attributed to different parts of the hairpins in the stationary TBL. Streamwise vorticity fluctuations are associated with the hairpin legs, wall-normal vorticity fluctuations with the neck segments and spanwise vorticity fluctuations with hairpin arches. The spanwise component shows to be clearly decreased between y = 2.5 to 8.5 [mm]. This decrease can stem from two sources. The first being less numerous/intense hairpin legs, the second being an inclination of the hairpin legs due to the plate motion. The second possibility implies that the leg vorticity is split in streamwise and spanwise direction. From the pointwise statistics it is obscure which phenomenon causes the effect. The wall-normal vorticity fluctuations are decreased by 50 [Hz] in the range between 2 and 6 [mm] through wall oscillation. Outside this range towards the wall and the free stream flow, the stationary and oscillated distributions converge. This indicates reduced hairpin neck activity. The spanwise component shows no significant difference between the stationary and oscillated case apart from a small region at y = 2 [mm]. Here it is also in doubt if the oscillation triggers a contribution by the hairpin legs towards the spanwise components. Generally speaking decreased vorticity fluctuations are found throughout the domain implying reduced hairpin strength and/or numbers in the domain. The discussion on vorticity fluctuation has to be treated with care. As described in section 5.5 tomographic PIV tends to underestimate vorticity fluctuations especially in regions of large gradients which is close to the wall in TBLs. A maximum error of 170 [Hz] was derived from the divergence error of the flow field. Indeed, comparing planar and tomo $\omega_{z_{RMS}}'$ data shows a significant underestimation close to the wall of up to 145 [Hz] as indicated by the red error bar in fig. 6.4. However, both data sets follow the trend to decrease in magnitude away from the wall and the underestimation becomes less significant. For example, the error at y = 4 [mm] shows an maximum underestimation of 40 [Hz] translating in an error of 4 [%] in vorticity. This shows that absolute values of vorticity have to be treated with care but trends can be trusted.

### 6.2.3. Reynolds stresses and turbulent kinetic energy production

Figure 6.5 shows the Reynolds stresses excluding the normal Reynolds stresses as they can be derived from the velocity fluctuations given in fig. 6.3. The ensemble of both give the full Reynolds stress tensor. Special focus in the discussion is given to $Re_{12}$ as its weight in the TKE production is largest ($P_k \approx -\frac{\partial \overline{u}}{\partial y} Re_{12}$) due to the strongest gradient of streamwise velocity in wall-normal direction in TBLs. This implies that negative regions of $Re_{12}$ lead to TKE production which has been discussed to increase turbulent skin friction. The figure reveals that both cases tend to 0 at the wall, which is a logical consequence of the wall boundary condition. The stationary distribution decreases rapidly in the negative regime and reaches its maximum of -0.018 [$m^2/s^2$] at y = 3 [mm]. Further in wall outward direction it reaches a slightly increasing plateau up to y = 8 [mm]. The oscillated case shows a similar shape, but with a decreased peak at y = 3 [mm] at -0.012 [$m^2/s^2$] followed by the plateau along the same Reynolds stress value. Comparing tomo to planar data a clear underestimation in the near wall region between y = 1 and 3 [mm] is found which is at no surprise as velocity fluctuations have shown to suffer from underestimation in this region. Therefore, these errors propagate to a maximum error of 0.004 [$m^2/s^2$] indicated by the error bar in the figure as was discussed in section 5.5.

$Re_{13}$ shows to be 0 throughout the domain both for the stationary and oscillated case. This be-

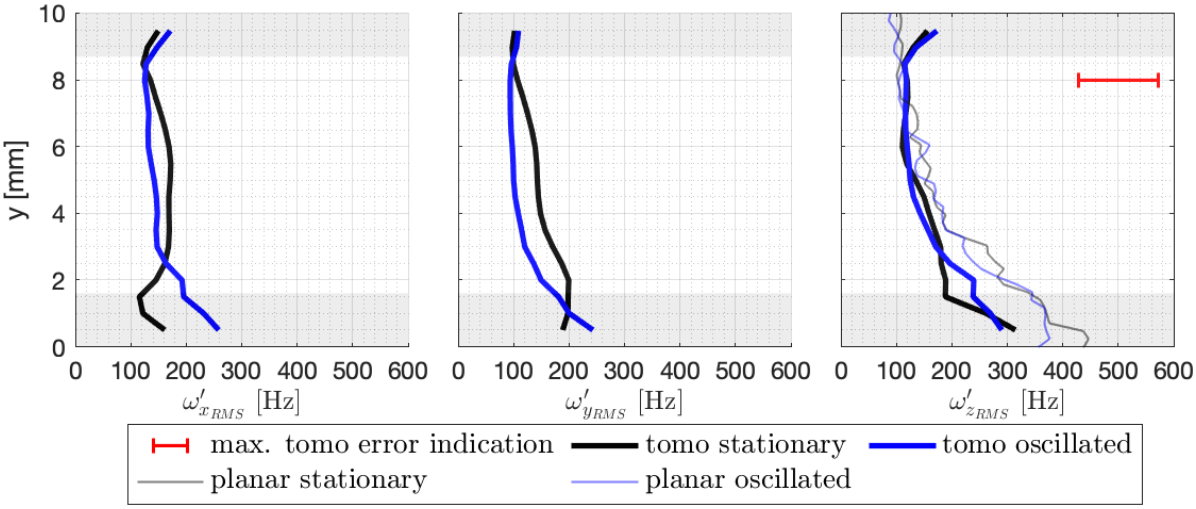


Figure 6.4: Stationary and phase-averaged ($HS$, $IS^-$, $LS$ and $IS^+$) TBL vorticity fluctuation RMS (planar data adapted from Kempaiah, 2019)

haviour could be attributed to the streamwise vortices which are responsible for spanwise fluctuations. As low and high-speed fluctuations lie in between these vortices, $\overline{u'w'}$ averages out to 0 due to the approximately equal but opposite impact from the streamwise vortices. As there are no planar data for the w-component, no accurate propagated error is determined, which also holds for the $Re_{23}$ distribution. $Re_{23}$ shows to tend to zero at the wall and increases to 0.04 [$m^2/s^2$] at y = 2.1 [mm] which marks an inflection point. Proceeding more outward the wall, the value decreases towards 0 at y = 5 [mm] after which the value recovers again to 0.04 [$m^2/s^2$] at y = 8 [mm]. The oscillated case shows to approach a finite value of around 0.01 [$m^2/s^2$] at the wall which reveals the effect of the oscillating wall. The distribution is characterized by a strong decrease towards 0 at y = 2 [mm] and then slightly deviates around 0 throughout the domain. The increased values near the wall show the effect of the periodic Stokes layer which is build up due to the plate oscillation. The decrease of $Re_{23}$ throughout the rest of the domain indicates less sweep and ejection events. Also here the advantage of tomographic PIV becomes apparent as the full set of Reynolds stresses can be determined. The decrease in $Re_{12}$ for wall oscillation was reported by many works before, $Re_{13}$ and $Re_{23}$ are novel. In comparison to $Re_{12}$ they are significant smaller in magnitude which implies that they are probably less affected by errors following the argumentation of Atkinson et al. (2011).

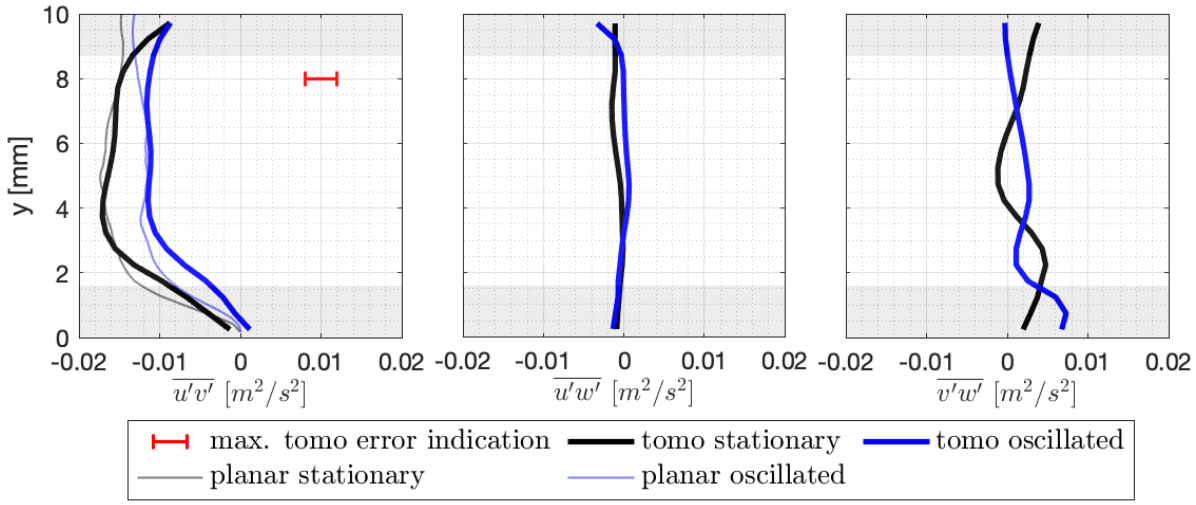


Figure 6.5: Stationary and phase-averaged ($HS$, $IS^-$, $LS$ and $IS^+$) Reynolds stresses: $Re_{12}$ (left), $Re_{13}$ (middle), $Re_{23}$ (right)

Planar and tomographic TKE energy production terms are given for the stationary and oscillated case in fig. 6.6. All curves follow a characteristic form, they start from 0 at the wall increase quasi-linearly to a peak at around y = 1.8 [mm] after which an asymptotic decrease follows towards a quasi constant value between y = 5 to 8 [mm]. Both, tomo and planar data sets show that the peak of the production is clearly decreased. The planar data show a decrease of 30 [%] and the tomographic data show a decrease of 40 [%]. This shows a clear offset of the tomographic data which is however at no surprise. The production term is calculated by ($P_k \approx -\frac{\partial \overline{u}}{\partial y} Re_{12}$). Both multipliers have shown to have the largest errors at the TKE peak location at y = 1.8 [mm] which propagate in the TKE production determination and can reach up to 110 [%] in the peak location indicated by the errorbar. This is a consequence of the drawbacks of tomographic PIV, being lower spatial resolution and underestimation of large velocity peaks. Even though these underestimations are quite severe, a decrease of TKE production through wall oscillation is found in both the planar and tomographic data sets. This clearly indicates less turbulence producing structures in the flow which translates to less strong or numerous sweep and ejection events.

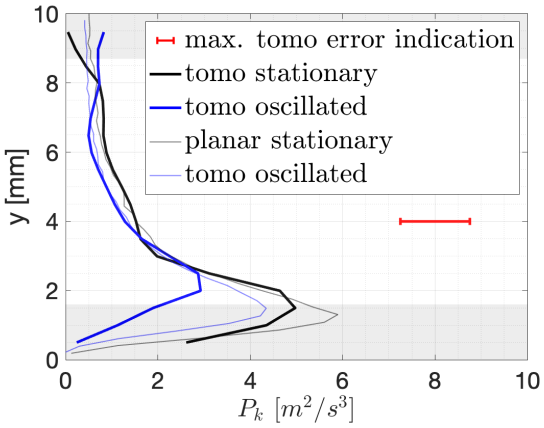


Figure 6.6: Stationary and phase-averaged ($HS$, $IS^-$, $LS$ and $IS^+$) TKE production planar approximated by $P_k \approx -\frac{d\overline{u}}{dy} Re_{12}$ and tomographic by $P_k \approx -\frac{d\overline{u}}{dy} Re_{12} - \frac{d\overline{v}}{dy} Re_{22} - \frac{d\overline{w}}{dy} Re_{22}$ (planar data adapted from Kempaiah, 2019)

## 6.3. Instantaneous coherent structure organisations

This section analyses coherent structures typically found in TBLs containing hairpin packets, sweep/ejection events and low/high-speed streaks. It shall be noted that sweep/ejection events can very well be related to the hairpin packets without analysing hairpins directly. Pointwise statistics have shown that the vorticity is the most critical property in terms of uncertainty. For this reason a pattern analysis on vorticity is not performed. Therefore, is decided to only analyse sweep/ejection and low/high-speed streaks which is done in section 6.3.1 and section 6.3.2. In total 10 instantaneous flow fields are used for the stationary case and for each phase of the oscillated case, implying that in total 50 VOV's are analysed. The pattern recognition method deployed is described in detail in section 6.3.1, whereas section 6.3.2 uses the same method but only presents the analysis results.

### 6.3.1. Sweep and ejection events

Sweep and ejection events are the major contributors to TKE production which has been discussed in section 2.5. The mechanism leading to sweep and ejections are hairpin packets resulting into a momentum exchange close to the wall which happens when low-speed fluid is lifted away (ejection) from the wall through the hairpin vorticity and the momentum deficit is equalized by high-speed fluid towards the wall (sweep). From this it is clear that based on the number, size and intensity of sweep and ejection events conclusions can be drawn concerning the size and intensity of the hairpin packets.

The method used to detect sweep and ejections is adapted from Martins et al. (2019), which uses detection function of the characteristic velocity statistics. Sweep and ejections are known to cause a

large negative fluctuations product of $u'v'$. Now the concept of detection functions is used to determine the regions where these fluctuations exceed the RMS of the corresponding flow field as given in eq. (6.1). A sample surface plot of the detection function of a stationary flow field at y = 5.2 [mm] is given in fig. 6.7a which gives detection function values between -3 and 3. The chosen threshold to categorize a region of the flow field as a sweep/ejection region is -1, implying coherent regions showing ${F^d}_{u'v'}$ < -1 are defined as such. In physical terms this method counts a region as a sweep/ejection region as such as soon as the fluctuations exceed the RMS of the corresponding plane.

$$ {F^d}_{u'v'} = \frac{u'v'(x,z)}{u'v'(y)_{rms}} \qquad threshold < -1 \tag{6.1} $$

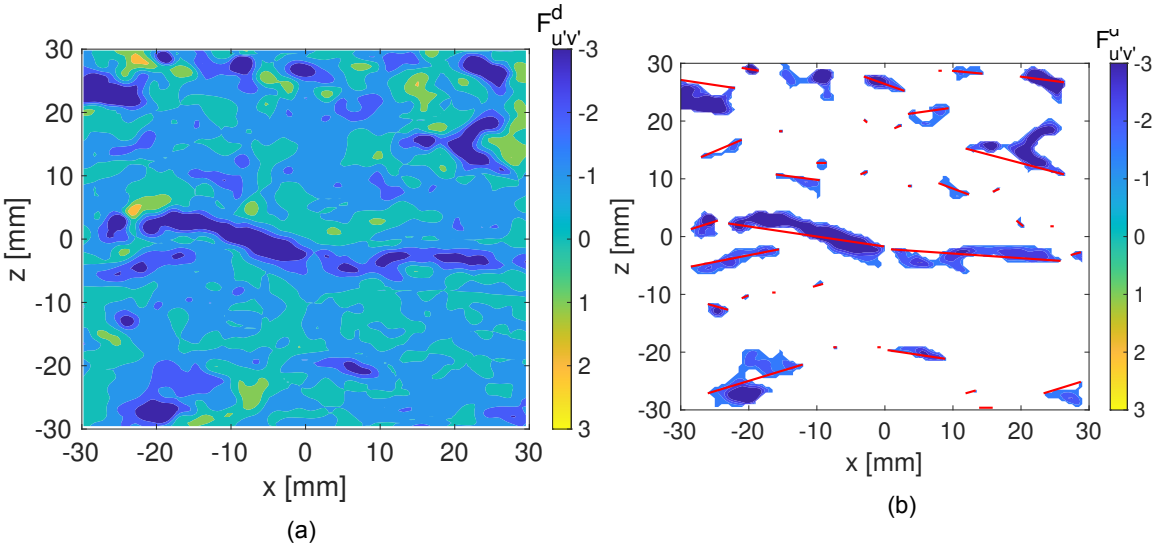


Figure 6.7: $F^d_{u'v'}$ stationary surface plots at y = 5.2 [mm] with (a) the full surface and (b) only areas classified as sweep/ejection events with indicated length scales (red lines), flow is from left to right

Using the method of eq. (6.1) the detected regions can be extracted which is shown in fig. 6.7b. These regions contain a lot of information about the vortical mechanisms in the TBL. Quantities of interest are the spatial occupation, intensity and length scale of the extracted regions. The spatial occupation gives information of the extend by which the plane is dominated by sweep/ejection events while the intensity level in terms of the detection function value gives insights in how strong those events are. In particular the length scale enables to link the events to the hairpin packet size following the findings of Zhou et al. (1997) which showed a streamwise hairpin head spacing of 100 $x^+$ for a TBL at $Re_\theta \approx$ 1,000. This allows for conclusions on the hairpin autogeneration mechanism which is the main engine of turbulence production and therefore turbulent skin friction.

The spatial occupation is simply evaluated as the ratio of the extracted area by the area total area of the plane. It is complemented by an intensity indication from which a intensity histogram arises for every wall parallel flow plane as shown in fig. 6.8a. It gives the number of extracted voxels ($|{F^d}_{u'v'}| > 1$) on the y-axis and the absolute value of $|{F^d}_{u'v'}|$ on the x-axis. The higher the mean of the histogram, the higher the average intensity found in the flow field. The length scale of the structures is found using an algorithm (PLautridou, 2016) capable of identifying clusters in matrices and storing the coordinates of all data points in the cluster. From these coordinates the distance between the most up- and downstream point within the cluster was regarded as the length of the structure (red lines in fig. 6.7b depict the length scales). From the length scales present in every plane a histogram is constructed with the length scale in [mm] on the x-axis and the number of structures on the y-axis as given in fig. 6.8b.

Spatial occupation and intensity characteristics per plane are represented as a function of wall-normal distance in fig. 6.9a and fig. 6.9b. The spatial occupation tends to 0 [%] when approaching the wall which is a logical consequence of the no-slip and non-permeability boundary condition of wall bounded flows (compare section 2.1). Throughout the viscous sublayer spatial occupation increases quasi-linear up to y = 3 [mm] after which all distributions reach a plateau like state between y = 3 to 8

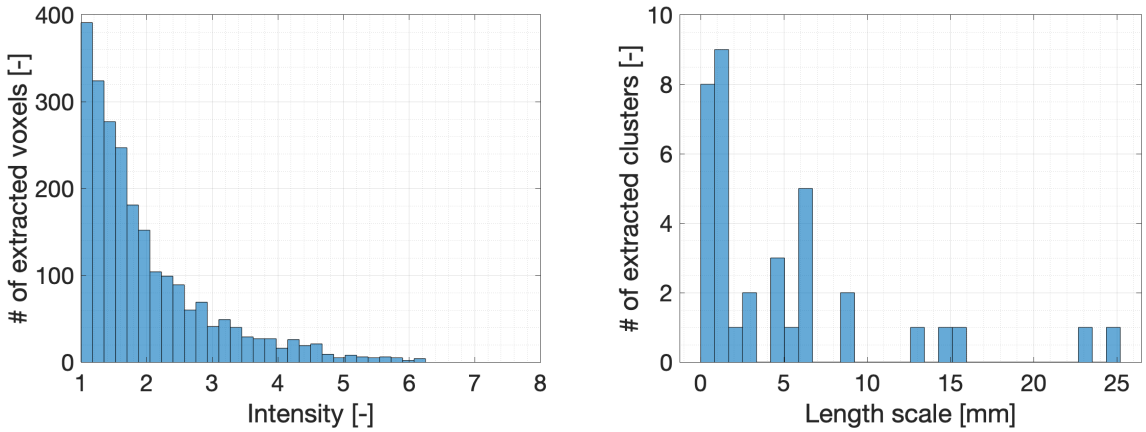


Figure 6.8: Histograms of sweep/ejection (a) intensity (measured as the magnitude of the detection function $|F^d{}_{u'v'}|$) and (b) length scales (measured as the distance between the most upstream and downstream point) of the single flow field given in fig. 6.7

[mm]. It is clearly seen that the stationary flow fields show a spatial occupation of 28 [%] at y = 3 [mm] while the mean of phases $HS$, $IS^-$, $LS$ and $IS^+$ shows to be located at 24 [%] at y = 3 [mm]. Entering the plateau between y = 3 and 8 [mm], the stationary distribution stays at a higher level, however the difference decreases towards 8 [mm]. The plateau values of the stationary wall decreases slightly from 28 [%] to 26 [%] while all batches show a constant level around 24 [%] having slight fluctuations, however no constant trend. The phase distributions only reveal noticeable differences in the region between y = 0 and 3 [mm] corresponding to $y^+ \approx 0$ to 30 which is known to contain the peak of TKE production from TBL theory (compare fig. 2.15). Here it is seen that only $IS^-$ shows 2 [%] less spatial occupation with respect to phase $HS$, $LS$ and $IS^+$ indicating that the formation of sweep/streak and therefore the hairpin autogeneration mechanism is attenuated the most in the cycle of a wall oscillation corresponding to the region just after the plate has reached the highest spanwise velocity.

The distribution of the streak/sweep intensities fluctuates for cases in the region between 1.6 and 2.2 as given in fig. 6.9b. The distributions seem to be randomly fluctuating. Therefore, it can be concluded that the intensity of the events is only little affected by the oscillation.

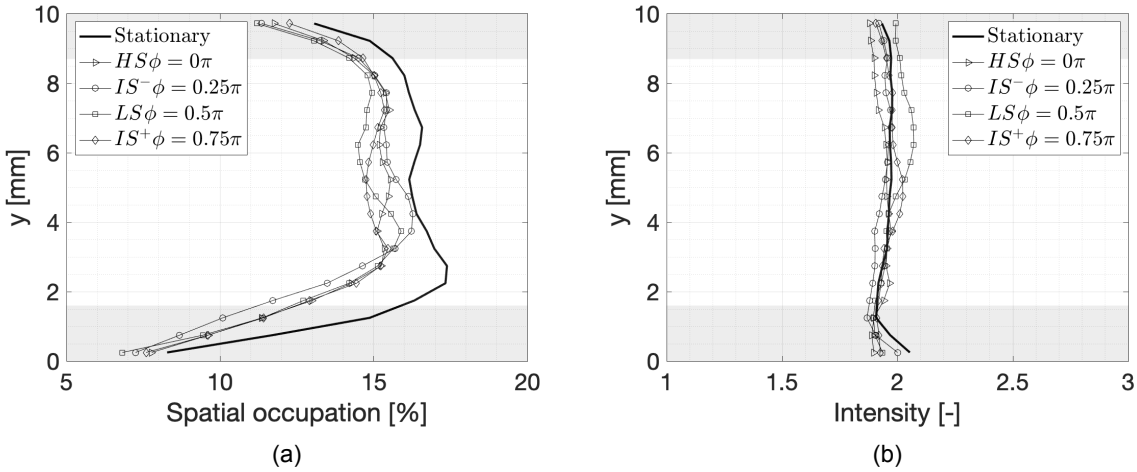


Figure 6.9: Wall-normal distribution of sweep/ejection events (a) spatial occupation (regions are classified if $F^d{}_{u'v'} < -1$) and (b) intensity (measured as the magnitude of the detection function $|F^d{}_{u'v'}|$)

Length scales of the identified sweep and ejection events are given in fig. 6.10. Figure 6.10a gives the mean length scale of the sweep/streak events per plate motion phase. Clearly reduced length scales are found when comparing the stationary to the oscillated case, where again the length scales in $IS^-$ are smaller than the the other phases of the plate motion. From section 2.4 it is known that in TBL of $Re_\theta \approx$ 1,000, hairpin heads are approximately spaced by 100 $x^+$ in streamwise direction. Considering the mean length scales, this would imply that only one hairpin is associated with an ejection event, however the mean length scale is dominated by granular turbulence production. To investigate the mechanism which produces the majority of the TKE production, one has to focus on the coherent regions to draw conclusions. To investigate those, the PDF of the length scales for the stationary case and the plate motion phase is given in fig. 6.10b.

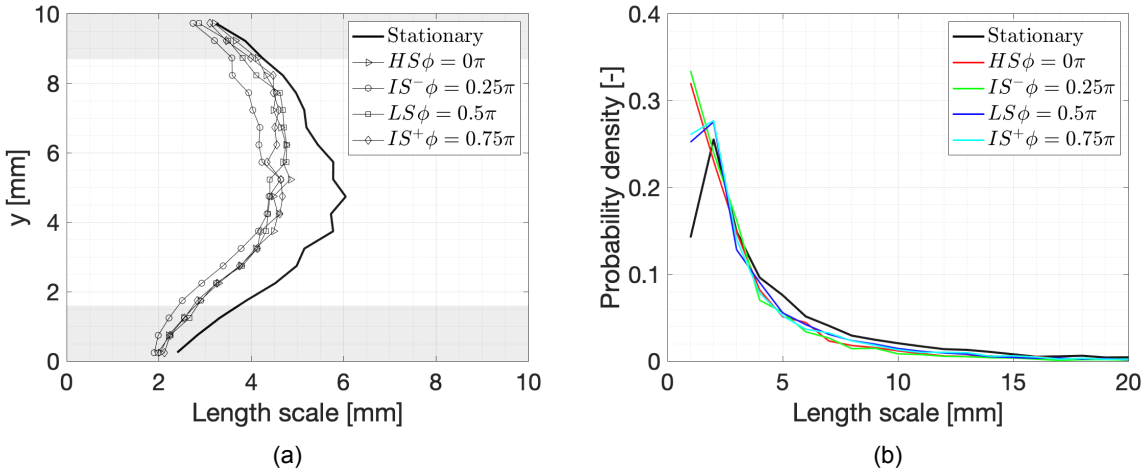


Figure 6.10: Length scales of sweep/ejection events (measured as the distance between the most upstream and downstream point) (a) wall-normal distribution (b) probability density function in the VOV

To focus on the coherent $-\overline{u'v'}$ events, it is wise to analyse the tail probabilities of fig. 6.10b in more detail and link them to an average hairpin packet number. This is shown in fig. 6.11 where an average hairpin head spacing of 100 $x^+$ is assumed, implying that 100 $x^+$ correspond to a packet number of two, 200 $x^+$ correspond to ta packet number three and so on. The results in fig. 6.11 clearly show that the occurrence of large packet number is decreased when the plate is oscillated. Towards the high packet numbers, $IS^-$ shows lowest probabilities on average, suggesting that the attenuation of hairpin autogeneration is affecting this phase most extreme.

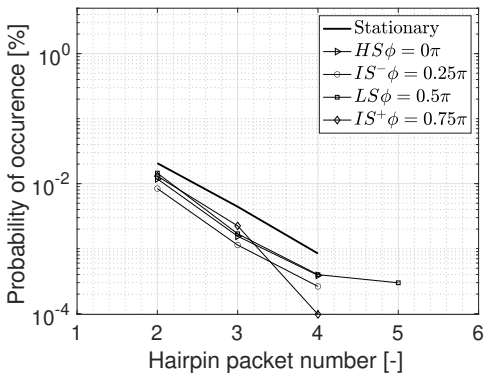


Figure 6.11: Probability of hairpin packet numbers for the stationary wall and during the four oscillation phases ($HS$, $IS^-$,$LS$ and $IS^+$)

### 6.3.2. Streak events

Low- and high-speed streaks are in close dependence with sweep and ejection events. Especially low-speed streaks are known to exist in the same locations of hairpin packets as their vorticity induces the lower speed of the streaks with respect to the field average (see section 2.5). Therefore, it is expected that also the streaks are shortest where the hairpin packet number was found to be the smallest, namely in the plate motion phase $IS^{-}$. The same detection methodology as applied in section 6.3.1 is applied for streak detection using the detection function eq. (6.2) with the given thresholds -1 for low-speed streaks and 1 for high-speed streaks (Martins et al., 2019).

$$F^{d}{}_{u'} = \frac{u'(x,z)}{u'(y)_{rms}} \qquad threshold < -1\, and\, > 1 \tag{6.2}$$

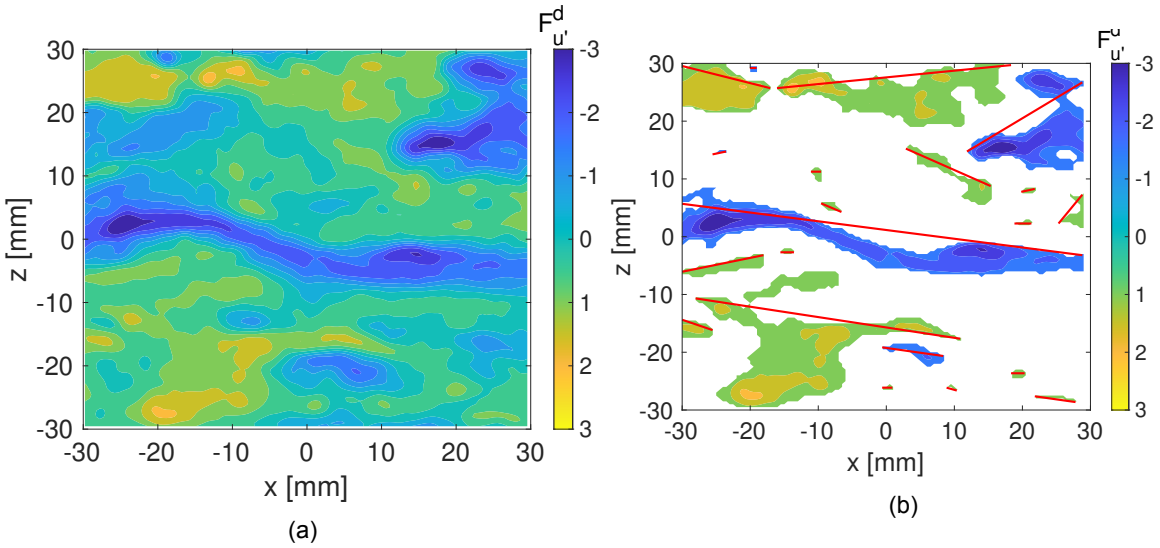


Figure 6.12: $F^{d}_{u'}$ stationary surface plots at y = 5.2 [mm] with (a) the full surface and (b) only areas classified as streak events with indicated length scales, flow is from left to right (same flow field as used in fig. 6.7)

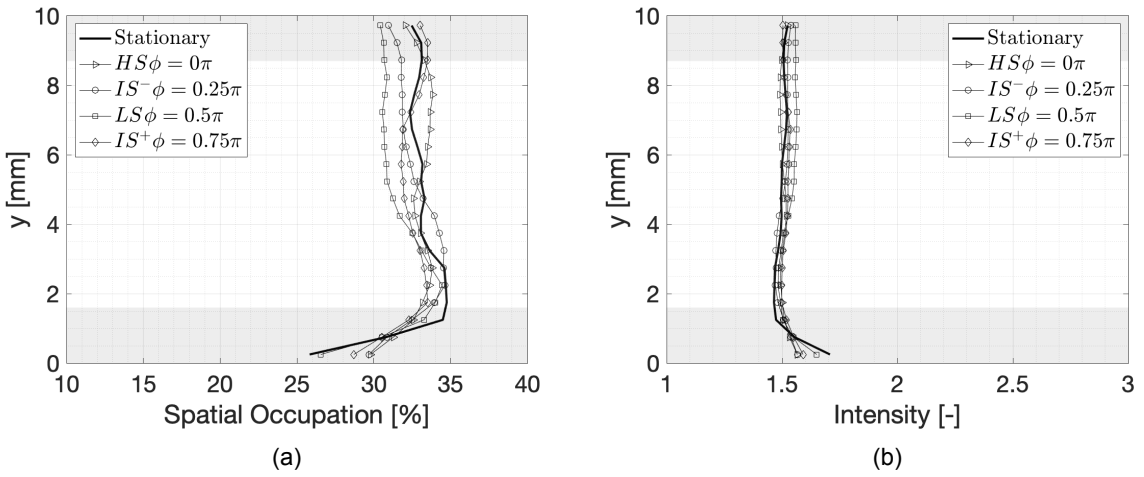


Figure 6.13: Wall-normal distribution of streak events (a) spatial occupation (regions are classified if $F^{d}{}_{u'} < -1 or > 1$) and (b) intensity (measured as the magnitude of the detection function $|F^{d}{}_{u'}|$)

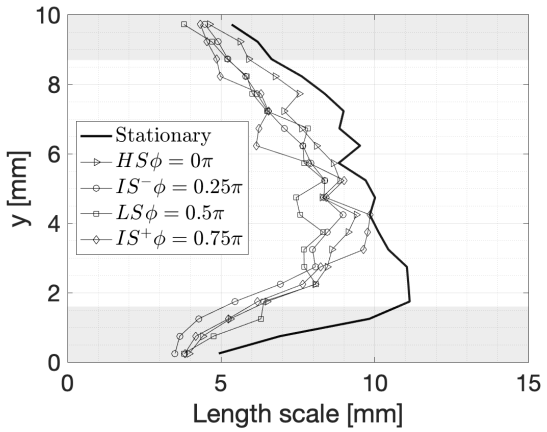


Figure 6.14: Wall-normal distribution of length scales of streak events (measured as the distance between the most upstream and downstream point)

Visually inspecting the surface plot of $F^{d}{}_{u'}$ in fig. 6.12a and the extracted low-speed streak locations in fig. 6.12b and confronting them with the surface plots of the sweep/ejection detection in fig. 6.7a and fig. 6.7b it is noted that the spatial coordinates of the low-speed streaks lie in close proximity of the sweep/ejection events, which is a consequence of the vortical dynamics in TBLs.

Analysing the wall-normal distribution of spatial occupation, intensity and length scales in fig. 6.13a, fig. 6.13b and fig. 6.13b it can be concluded that especially in region between y = 0 to 4 [mm] there are no significant differences in spatial occupation and intensity of the streaky structures. However, as expected, the length scales of the oscillated case are significantly reduced by up to 35 [%] at y = 2 [mm] with respect to the stationary case. In the near wall region between y = 0 and 3 [mm], the $IS^{-}$ section of the cycle shows to have the smallest length scale of the streaks which motivates the hypothesis stated in section 6.3.1 saying that in $IS^{-}$ the probability of high hairpin packet numbers is decreased.

## 6.4. Mechanism model

The findings of section 6.2 and section 6.3 have revealed many changes in TBL characteristics of a stationary vs. oscillated plate. The tomographic pointwise velocity statistics showed that the gradient of spanwise velocity in wall-normal direction was decreased under spanwise wall oscillation. In terms of velocity fluctuations, the streamwise component was decreased by 10 [%] while spanwise and wall-normal fluctuations only decreased marginally. Vorticity fluctuations have shown to be attenuated in all three components. These differences result in to smaller magnitudes of Reynolds stresses and sum up to a decrease of 40 [%] of TKE production. It is known from literature that TKE production is the cause of turbulent skin friction. Therefore the region of large TKE production differences in tomographic measurements is characterized by much vortical activity and is limited to y = 0 to 3 [mm] corresponding to $y^{+}$ = 0 to 30 (Kempaiah, 2019).

Analysis of instantaneous coherent flow organizations in section 6.3 backed up these findings. The reduction in spatial occupation of streaks and sweep/ejection events is most severe between y = 0 and 3 [mm] (see fig. 6.13a and fig. 6.9a) while the $IS^{-}$ region shows significant lower spatial occupation than the other phases (for clarification the discretisation method used is given again in fig. 6.15). The same trend can be found in the length scale analysis of these structures in fig. 6.14 and fig. 6.10a which show significant reduction in length scale in the oscillated cases and $IS^{-}$ with the smallest scales among the oscillated data.

These results seem to be insightful, however in (section 6.2) it was discussed in much detail that many of the properties are underestimated especially in the regions of large gradients due to a low SNR as seen in fig. 5.12. However, as all tomographic measurements suffer from this systematic underestimation, a relative quantitative comparison of coherent structure characteristics is still possible to derive a descriptive model of the mechanism, while any mathematical doesn't seem to add value to the discussion.

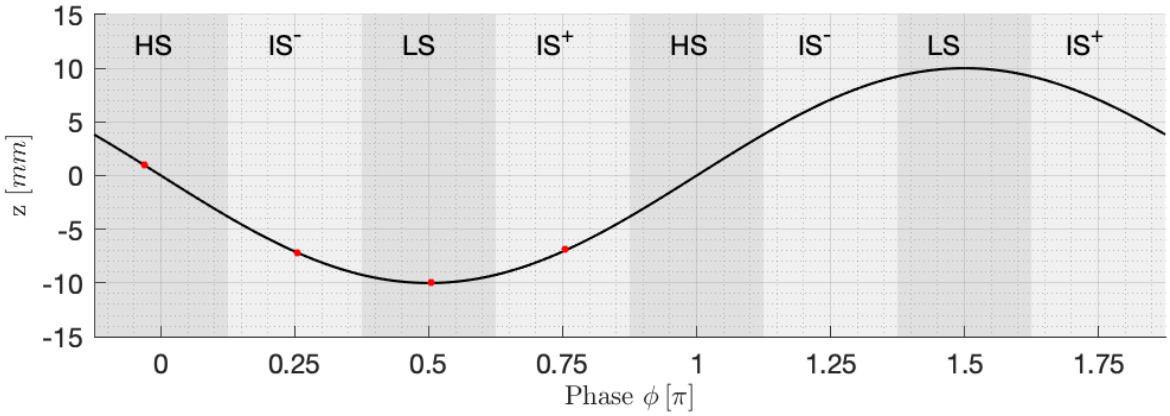


Figure 6.15: Phasewise discretisation of the plate oscillation including a measure of the phase scattering represented by the red dots

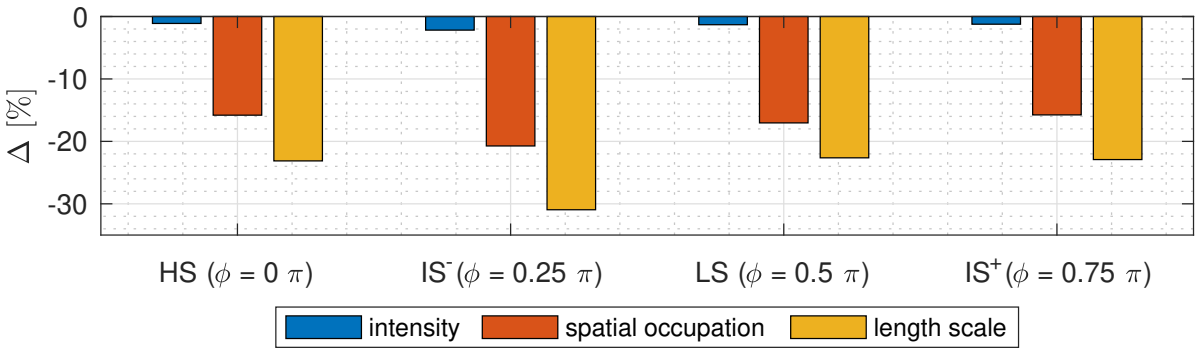


Figure 6.16: Mean changes (Δ) of sweep/ejection characteristics relative to the stationary wall from $y^+$ = 0 to $y^+$ = 30 in [%]

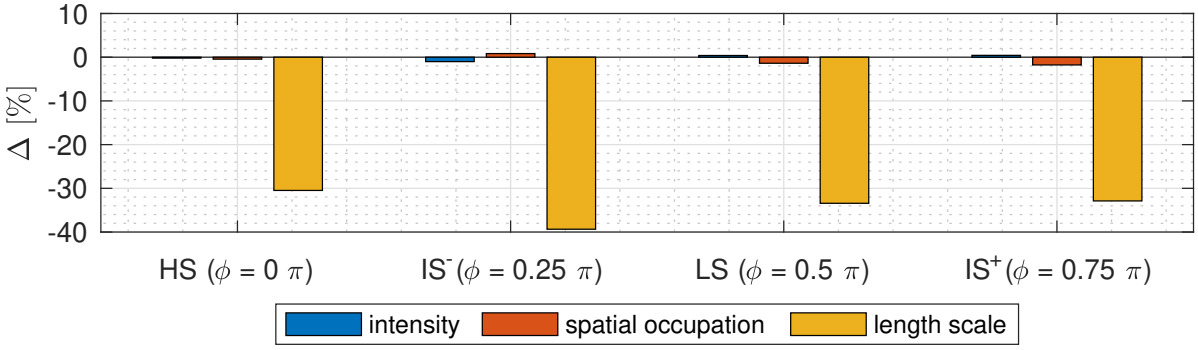


Figure 6.17: Mean changes (Δ) of streak characteristics relative to the stationary wall from $y^+$ = 0 to $y^+$ = 30 in [%]

A descriptive model is derived from the relative changes of sweep/ejection and streak characteristics of different motion phases ($HS$, $IS^-$,$LS$, $IS^+$) with respect to the stationary wall. The sweep/ejection data are given in fig. 6.16 which shows that the change in spatial occupation and length scale is much larger than intensity changes. Furthermore, it is concluded that the highest TDR favourable changes are found in $IS^-$ (least intensity, least spatial occupation and smallest length scales) indicating that coherent sweep/ejection events are shorter and less intense. From TBL theory it is well known that sweep and ejection events are triggered by hairpin packets which autogenerate. The better the autogeneration mechanism works, the larger those packets grow. This implies, that during high-speed motion of the

plate, this mechanism is disturbed most severe and the maximum attenuation effect lags the $HS$ phase and is most apparent in $IS^-$.

The findings for the streaks in fig. 6.17 show that the only significant changed characteristic is the length scale. It was discussed in section 2.5 that low-speed streaks are induced by the spanwise hairpin vorticity. Therefore a higher hairpin packet number causes longer low-speed streaks. Thus, the largest reduction in length in $IS^-$ supports the findings of reduced hairpin packet size and a less effective autogeneration mechanism in the $HS$ phase. Indicative instantaneous detection function surface plots for the stationary case and $IS^-$ phase are given in fig. 6.18 and fig. 6.19 showing sweep/ejection and streaky structures. These two flow fields are chosen as they show the two most extreme changes in streak and sweep/ejection characteristics. The same surface plots of the full cycle for streaks and sweeps/ejections are given in appendix A.3.

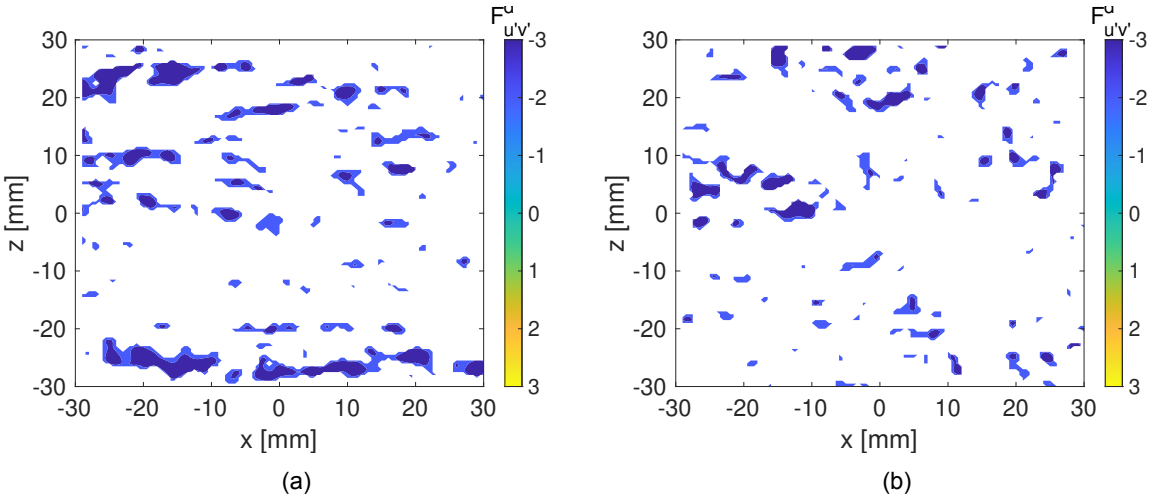


Figure 6.18: Representative surface plots of extracted streaks: (a) stationary, (b) $IS^-$ at 17 $y^+$, flow is from left to right

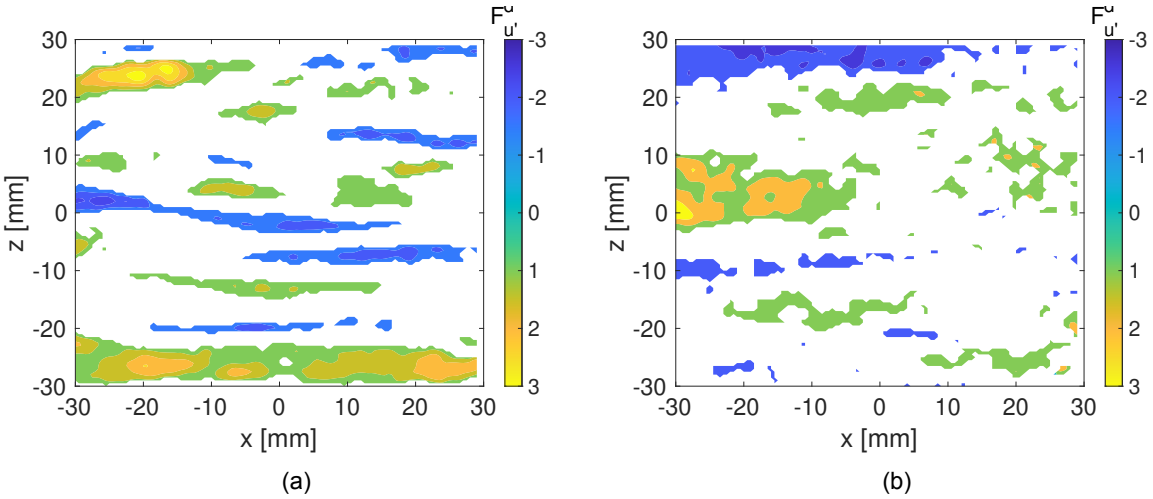


Figure 6.19: Representative surface plots of extracted sweeps/ejections: (a) stationary, (b) $IS^-$ at 17 $y^+$, flow is from left to right

# 7

# Conclusions and recommendations

This chapter concludes on the research results obtained in the thesis to answer the posed research questions as stated in section 7.1. During the research of this project many ideas arose in refining and improving the PIV set-up and post processing methods which could serve as an improvement to the findings and model which are presented in section 7.2.

## 7.1. Conclusion

The research of this MSc paper was done in the context of reducing carbon dioxide emissions of aviation by TDR. TBL theory with special attention to its coherent structures which play a vital role in turbulent drag generation are reviewed. One promising technique was identified to be TDR by spanwise wall oscillations. Many researchers have successfully shown that this technique can reach up to 45 % TDR under optimum circumstances. However, as three dimensional coherent structures are the dominant features in TBLs to generate turbulent drag, it is of utmost importance to understand the three-dimensional changes of TBLs under spanwise wall oscillation. This was a identified gap in TDR research by spanwise wall oscillation, as a three-dimensional analysis was not yet performed. From this, the following research question was formulated:

**How is the three-dimensional vortical mechanism of the TDR due to a spanwise oscillating flat plate related to the phase of the plate motion and can a descriptive/mathematical model relating the plate motion phase to the change of coherent structures in the TBL be defined?**

1. Is the oscillating wall affecting the coherent structures in the TBL?
    (a) What is the number of coherent structures (streaks, hairpins, ejections, sweeps) in different phases of the plate motion found in the volume of view?
    (b) What is the intensity and size of the coherent structures (streaks, hairpins, ejections, sweeps) in different phases of the plate motion found in the volume of view?

    To answer the questions, pointwise statistics are investigated and validated with planar measurements where possible. It is concluded that especially the fluctuating quantities of velocity and vorticity are decreased. Largest decreases are found in the region of $y^+$ from 0 to 30, which mark the region where TKE production is maximized. As the vorticity statistics suffer most severely from uncertainty, it is decided to only conduct a pattern analysis on sweep/ejections and low/high speed streak. However, this doesn't narrow the quality of analysis as it is known from TBL theory that these structures have a strong interdependence with hairpin vortices. This implies that findings in sweep/ejections and low/high-speed regions can be directly linked to hairpin packets. Sweep/ejection events in the oscillated acquisitions are found to have less spatial occupation in the measurement domain while they are also found to be decreased in length. It is decided to analyse the spatial occupation instead of the total number of structures, as they show to be much more granular when the plate is oscillated. Their intensity shows to be independent of the oscillation. The length of the sweep/ejection regions are linked to hairpin packet numbers from which

it is shown that large hairpin packets have lowest probability of appearance in the $IS^-$ phase. Low/high speed streaks show to be decreased in length, while the intensity and spatial occupation is almost unaffected by wall oscillation.

2. Can the plate motion phase be related to the coherent structure number, size and intensity?

   (a) What kind of relationships can be established between the phase of the plate motion and number, intensity and size of the coherent structures?

   (b) Is it possible to set-up a descriptive/mathematical model describing the changes in coherent structure number, intensity and size as a function of the plate motion phase?

   Closer analysing the coherent structure characteristics in the cycle of oscillation, a clear phase dependence is found. Results show, that the most favourable differences (decreased occupation, smaller length scales) are found for both, streaks and sweep/ejection events in the $IS^-$ phase. This is the phase immediately after the $HS$ (high speed) phase of the plate motion. From this a descriptive model is derived with the hypothesis that the autogeneration mechanism is attenuated through staggering in the $HS$ phase of the plate motion leading to smaller hairpin packet numbers. As these processes are time dependent, the largest effect of suppressing hairpin autogeneration is present with a lag just after the $HS$ phase where clearly hairpin packet numbers are decreased.

## 7.2. Recommendations

The PIV set-up has shown to be a challenge as it was operated at the edge of acceptable illumination intensity and therefore also SNR. One way to obtain higher SNR values and higher spatial resolution could be to limit the VOV to a wall-normal distance of y = 0 to 3 [mm] as this region has shown to have the most impact due to spanwise wall oscillation. Furthermore, a multi-pass laser set-up could help to amplify the intensity in the VOV. Also, synchronizing the motor to the PIV system could make the stroboscopic sampling superfluous. This would enlarge the VOV, as the current acquisition contain an optical indication of the phase which makes this region of the images unsuitable for particle reconstruction.

The coherent structure detection analysis showed that the intensity of the structures is constant. Here it shall be noted that the detection function and the threshold are user dependent choices. This implies that deriving conclusions from the results is only valid if the design of the method is respected. Therefore, changing the algorithm can reveal more insights.

Finally, as the vortical processes in TBLs are three dimensional and unsteady, a time dependent tomographic PIV measurement campaign could give more input towards a finer phase dependent analysis and therefore a better basis to refine the proposed model.

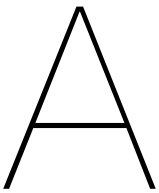

# Appendix A

# A.1. Stationary pointwise statistics

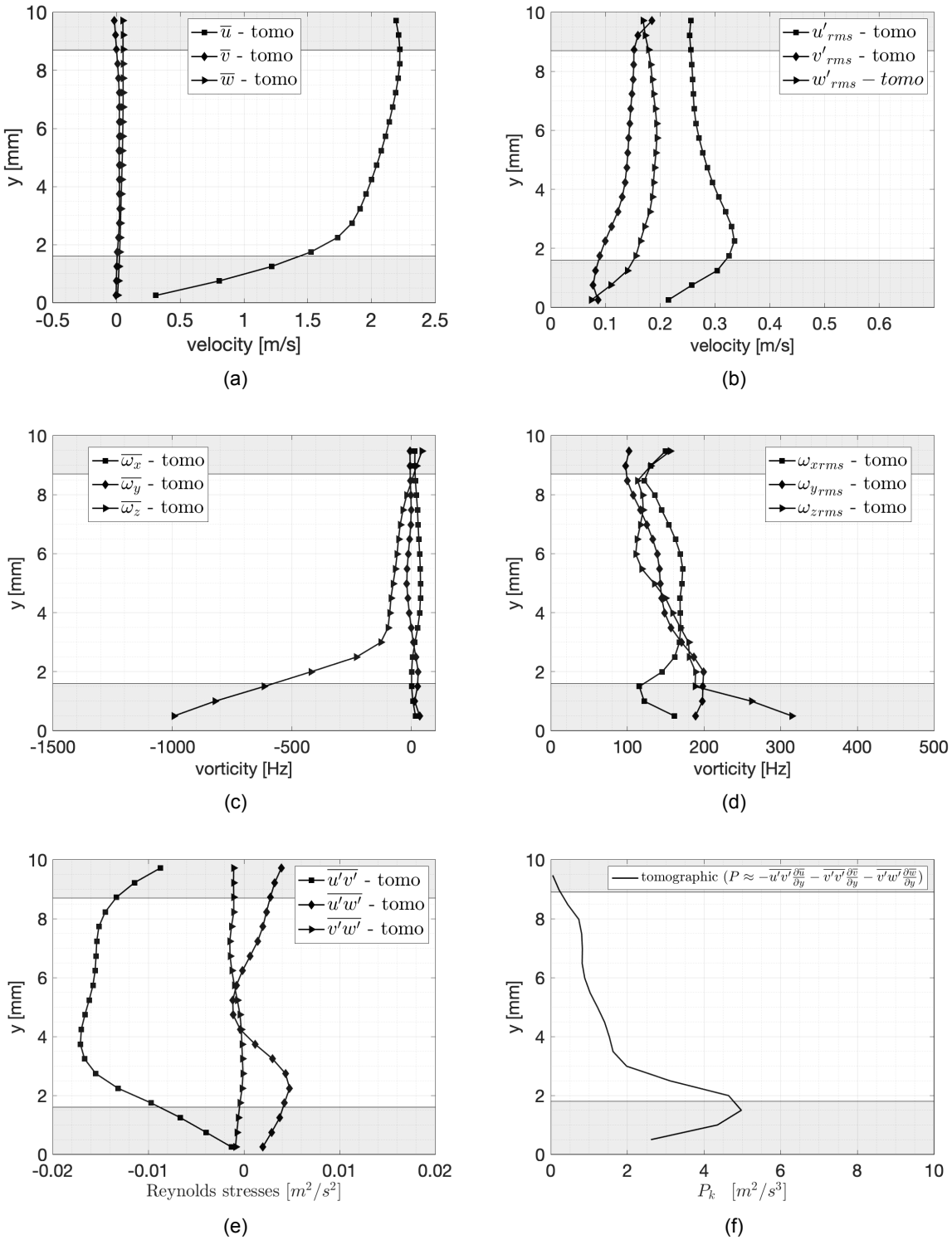


Figure A.1: Full set of pointwise statistics of the **stationary** case (N=5,000): (a) mean velocities, (b) velocity fluctuations, (c) mean vorticity, (d) vorticity fluctuations, (e) Reynolds stresses, (f) TKE production ($P \approx -\overline{u'v'}\frac{\partial \overline{u}}{\partial y} - \overline{v'v'}\frac{\partial \overline{v}}{\partial y} - \overline{v'w'}\frac{\partial \overline{w}}{\partial y}$)

## A.2. Oscillated pointwise statistics

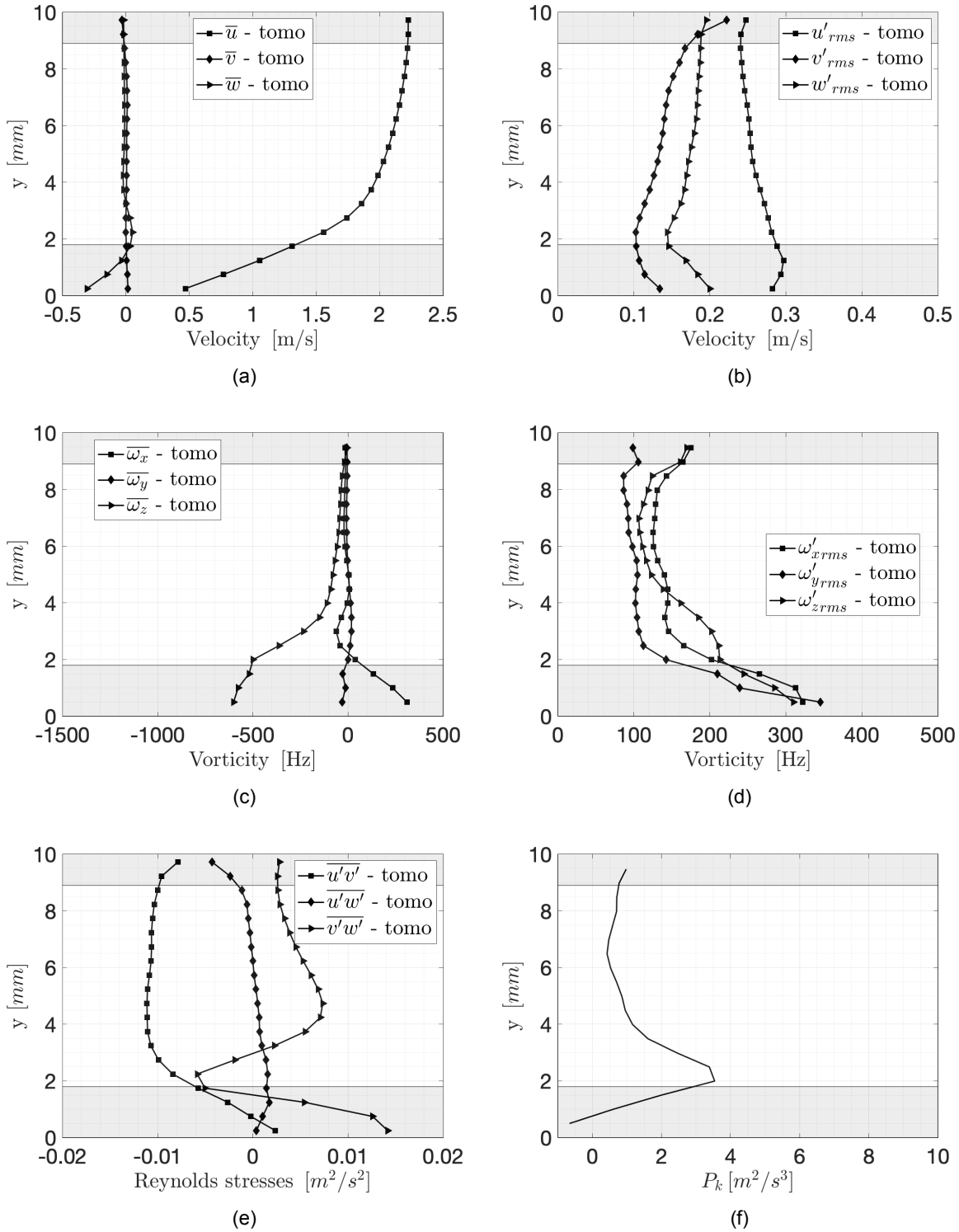


Figure A.2: Full set of pointwise statistics of the **HS-phase** (N=5,000): (a) mean velocities, (b) velocity fluctuations, (c) mean vorticity, (d) vorticity fluctuations, (e) Reynolds stresses, (f) TKE production ($P \approx -\overline{u'v'}\frac{\partial \overline{u}}{\partial y} - \overline{v'v'}\frac{\partial \overline{v}}{\partial y} - \overline{v'w'}\frac{\partial \overline{w}}{\partial y}$)

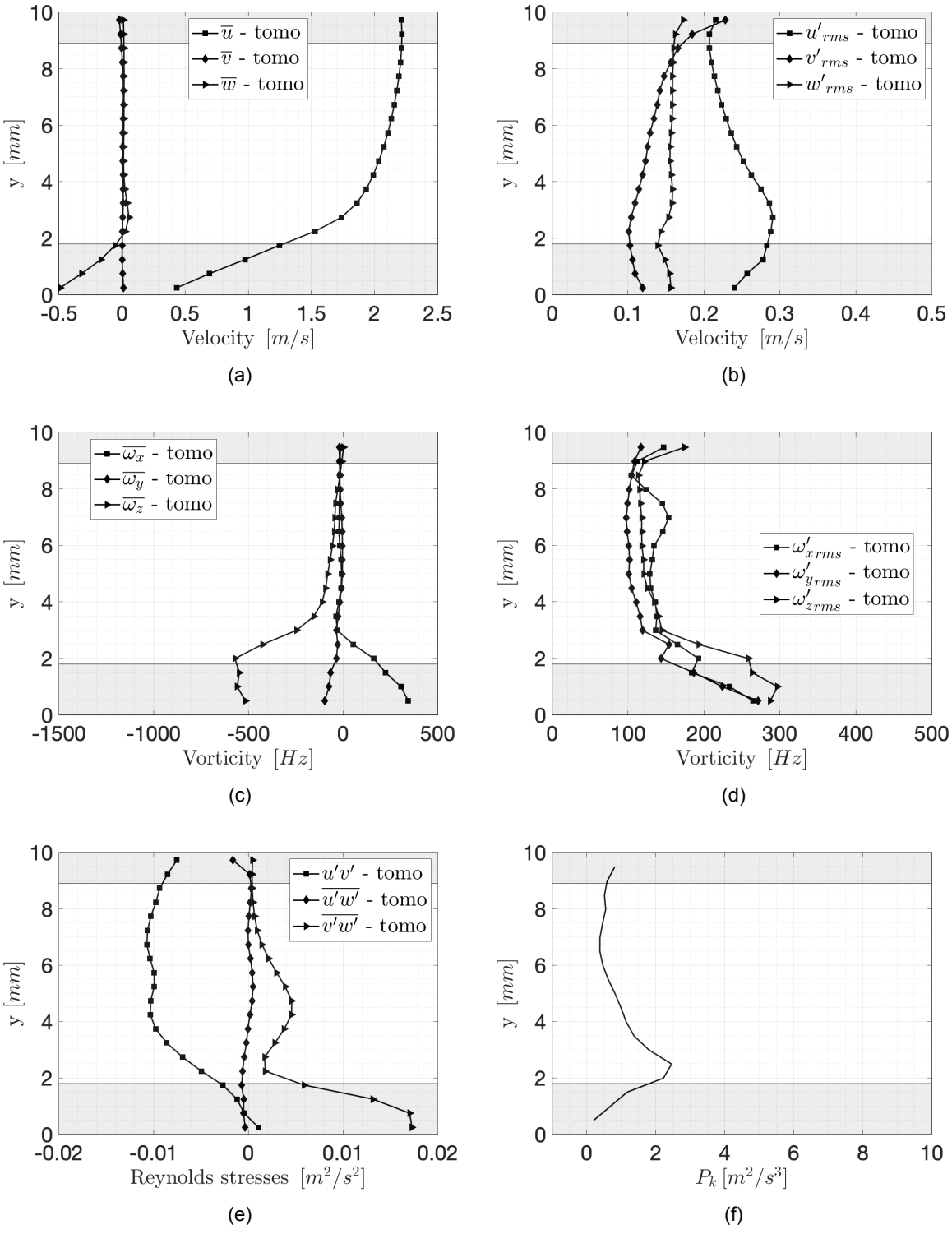


Figure A.3: Full set of pointwise statistics of the **IS⁻-phase** (N=5,000): (a) mean velocities, (b) velocity fluctuations, (c) mean vorticity, (d) vorticity fluctuations, (e) Reynolds stresses, (f) TKE production ($P \approx -\overline{u'v'}\frac{\partial \overline{u}}{\partial y} - \overline{v'v'}\frac{\partial \overline{v}}{\partial y} - \overline{v'w'}\frac{\partial \overline{w}}{\partial y}$)

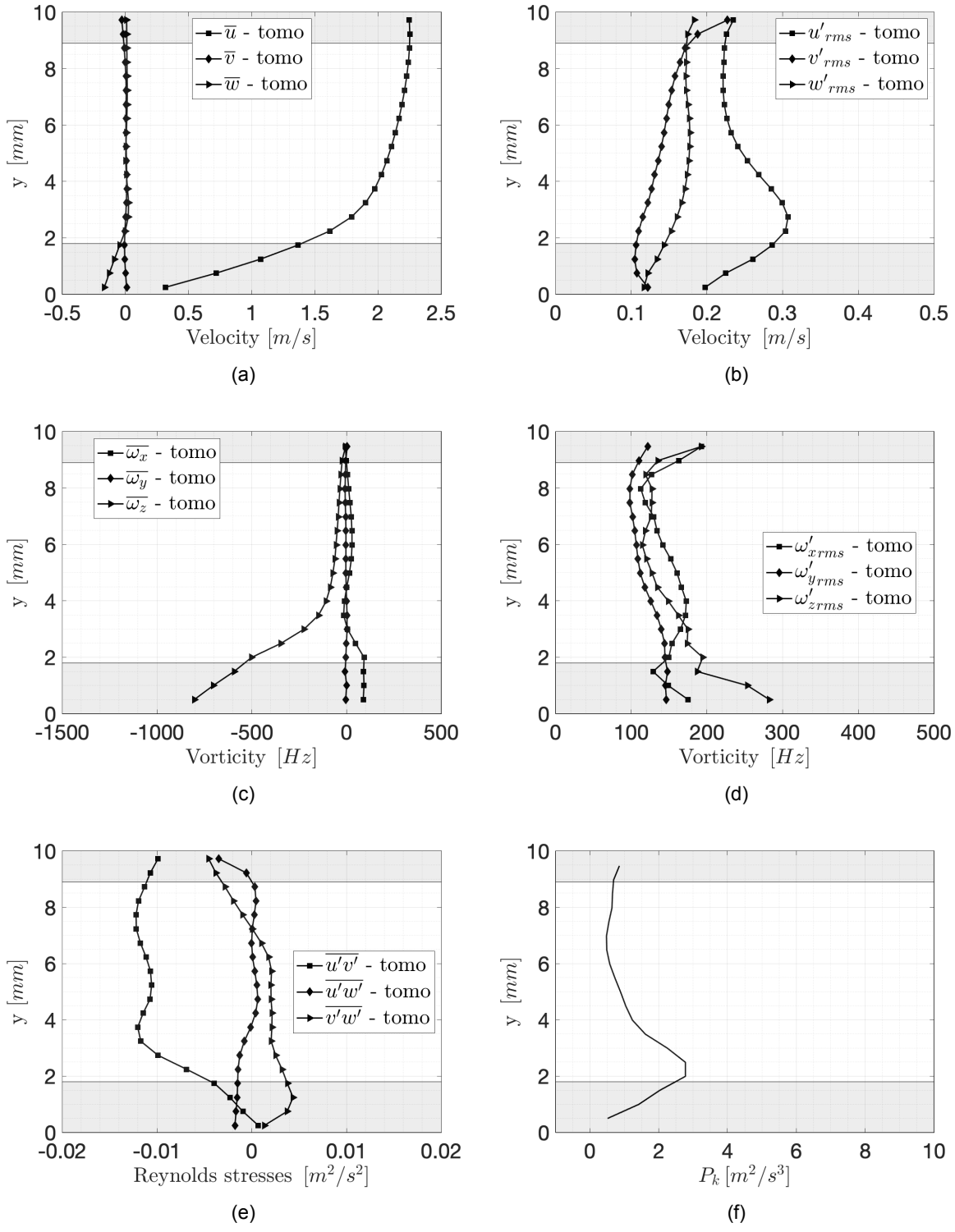


Figure A.4: Full set of pointwise statistics of the **LS-phase** (N=5,000): (a) mean velocities, (b) velocity fluctuations, (c) mean vorticity, (d) vorticity fluctuations, (e) Reynolds stresses, (f) TKE production ($P \approx -\overline{u'v'}\frac{\partial \overline{u}}{\partial y} - \overline{v'v'}\frac{\partial \overline{v}}{\partial y} - \overline{v'w'}\frac{\partial \overline{w}}{\partial y}$)

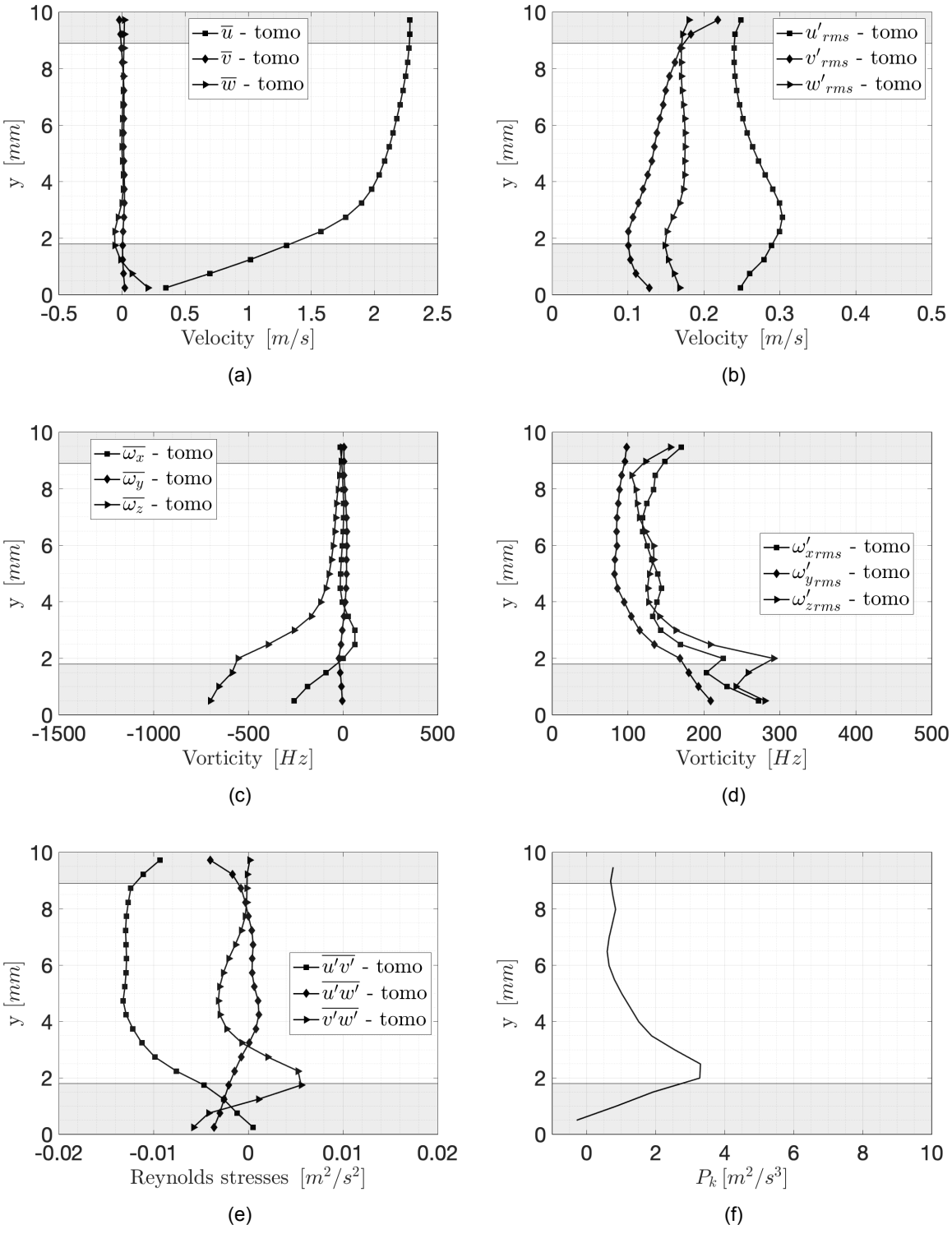


Figure A.5: Full set of pointwise statistics of the **IS$^+$-phase** (N=5,000): (a) mean velocities, (b) velocity fluctuations, (c) mean vorticity, (d) vorticity fluctuations, (e) Reynolds stresses, (f) TKE production ($P \approx -\overline{u'v'}\frac{\partial \overline{u}}{\partial y} - \overline{v'v'}\frac{\partial \overline{v}}{\partial y} - \overline{v'w'}\frac{\partial \overline{w}}{\partial y}$)

## A.3. Detection function plots streaks and sweeps/ejections

.

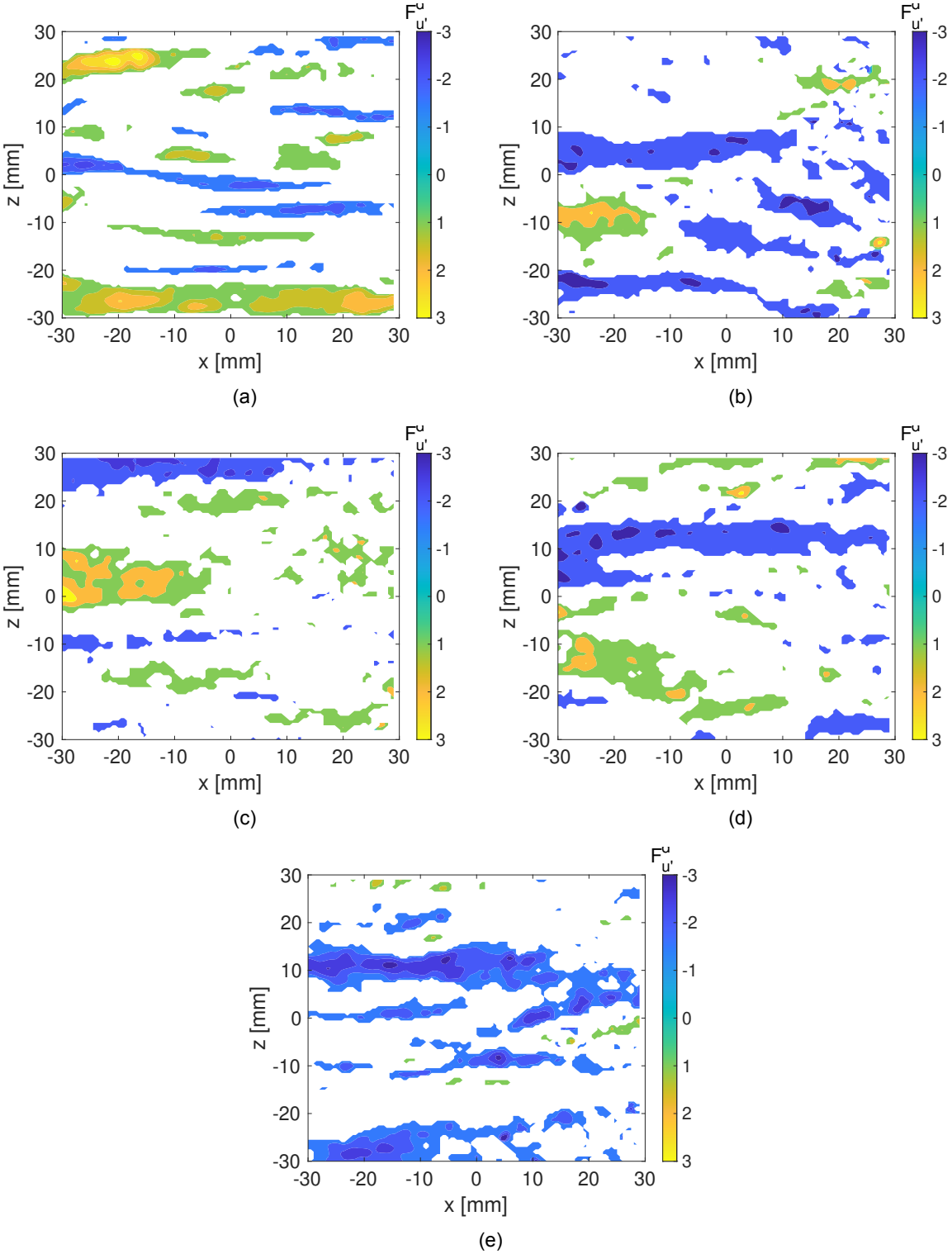


Figure A.6: Representative surface plots of extracted streaks: (a) stationary, (b) $HS$, (c) $IS^{-}$, (d) $LS$ and (e) $IS^{+}$at 17 $y^{+}$, flow is from left to right

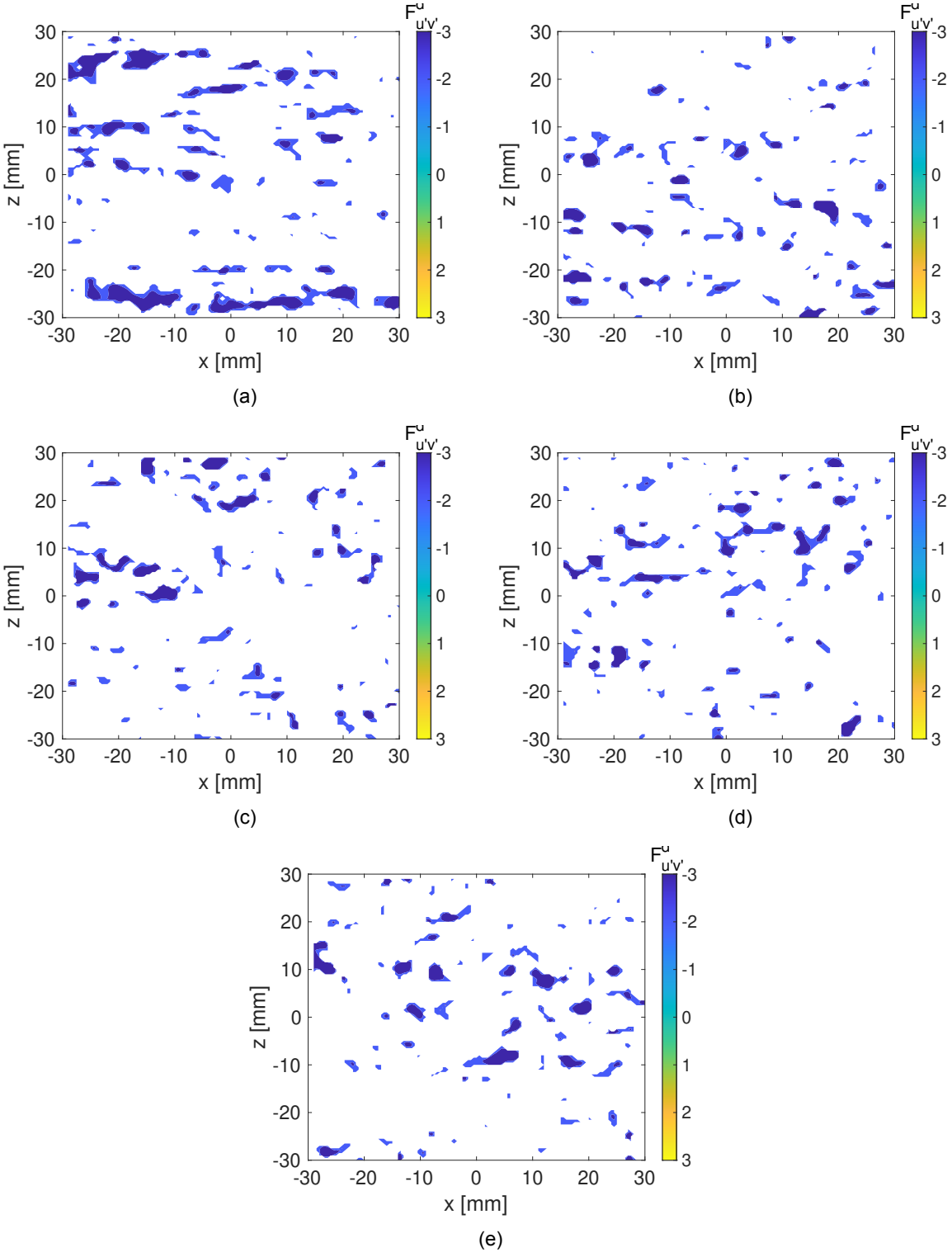


Figure A.7: Representative surface plots of extracted sweeps: (a) stationary, (b) $HS$, (c) $IS^{-}$, (d) $LS$ and (e) $IS^{+}$at 17 $y^{+}$, flow is from left to right, similar instantaneous fields used as in fig. A.6

# Bibliography


[1] Meinahrt C.D. Tomkins C.D. Adrian, R.J. Vortex organizations in the outer region of the turbulent boundary layer. *Journal of Fluid Mechanics*, 422:1–54, 2000. doi: 10.1017/S0022112000001580.

[2] R.J. Adrien. Hairpin vortex organization in wall turbulence. *Physics of fluids*, 19(4):041301, 2007. doi: 10.1063/1.2717527.

[3] M. Albers, P. S. Meysonnat, and W. Schröder. Drag reduction via transversal wave motions of structured surfaces. *10th International Symposium on Turbulence and Shear Flow Phenomena (TFSP10)*, 4:"10B–6", 2017.

[4] B. Arturo and M. Quadrio. Turbulent drag reduction by spanwise wall oscillations. *Applied Scientific Research*, 55(4):311–326, 1995. doi: 10.1007/BF00856638.

[5] ATAG. Reducing emissions from aviation, 2018. URL https://www.atag.org/facts-figures.html.

[6] C. Atkinson, S. Coudert, Foucaut. J-M., M. Stanislas, and J. Soria. The accuracy of tomographic particle image velocimetry for measurements of a turbulent boundary layer. *Experiments in Fluids*, 50(4):1031–1056, 2011. doi: 10.1007/s00348-010-1004-z.

[7] C. Chin, R. Örlü, J. Monty, N. Hutchins, A. Ooi, and P. Schlatter. Simulation of a large-eddy-break-up device (lebu) in a moderate reynolds number turbulent boundary layer. *Flow, Turbulence and Combustion*, 98(2):445–460, 2017. doi: 10.1007/s10494-016-9757-y.

[8] H. Choi, P. Moin, and J. Kim. Active turbulence control for drag reduction in wall-bounded flows. *Journal of Fluid Mechanics*, 262(A):75–110, 1994. doi: 10.1017/S0022112094000431.

[9] K.-S. Choi. Smart flow control with riblets. *Advanced Materials Research*, 745:27–40, 2013. doi: 10.4028/www.scientific.net/AMR.745.27.

[10] K.-S. Choi, J.-R. DeBisschop, and B. R. Clayton. Turbulent boundary-layer control by means of spanwise wall oscillation. *AIAA Journal*, 36(7):1157–1163, 1998. doi: 10.2514/2.526.

[11] K-S. Choi, T. Jukes, and R. Whalley. Turbulent boundary-layer control with plasma actuators. *Philosophical Transactions of the Royal Society*, 369(1940):1443–1458, 2011. doi: 10.1098/rsta.2010.0362.

[12] Dimple Technologies. Fly greener, further, and faster with our novel drag-reducing surface, 2020. URL https://dimple-technologies.com/#section-turbulence.

[13] G.E. Elsinga, F. Scarano, B. Wieneke, and B.W. van Oudheusden. Tomographic particle image velocimetry. *Experiments in Fluids*, 41(6):933–947, 2006. doi: 10.1007/s00348-006-0212-z.

[14] EU Council. Facts & figures, 2012. URL https://ec.europa.eu/clima/policies/transport/aviation_en.

[15] European Council. International agreements on climate action, 2018. URL https://www.consilium.europa.eu/en/policies/climate-change/international-agreements-climate-action/.

[16] Federal Foreign Office of Germany. The kyoto protocol - currently the most important global environmental agreement, 2020. URL https://www.auswaertiges-amt.de/en/aussenpolitik/themen/klima/-/243944.

[17] K. Fukagata, K. Iwamoto, and N. Kasagi. Contribution of reynolds stress distribution to the skin friction in wall-bounded flows. *Physics of Fluids*, 14(11):73–76, 2002. doi: https://doi.org/10.1063/1.1516779.

[18] S. Ghaemi and F Scarano. Multi-pass light amplification for tomographic particle image velocimetry applications. *Measurement Science and Technology*, 21(12):127002, 2010. doi: 10.1088/0957-0233/21/12/127002.

[19] K. Gouder, P. Mark, and J. F. Morrison. Turbulent friction drag reduction using electroactive polymer and electromagnetically driven surfaces. *Experiments in Fluids*, 54(1):1441, 2013. doi: 10.1007/s00348-012-1441-y.

[20] M.R. Head and P. Bandyopadhyay. New aspects of turbulent boundary layer structure. *Journal of Fluid Mechanics*, 107(11):297–338, 1981. doi: 10.1017/S0022112081001791.

[21] G.T. Herman and A. Lent. Iterative reconstruction algorithms. *Computers in Biology and Medicine*, 6(4):273–294, 1976. doi: 10.1016/0010-4825(76)90066-4.

[22] S. Hulshoff and S. Hickel. Ae 4137 cfdiii: Large eddy simulation slides. *TU Delft*, 2018.

[23] Innovation Quarter. Tu delft and klm collaborate on sustainable aviation, present flying scale-model flying-v, 2020. URL https://www.investinrotterdamthehaguearea.org/portfolio-item/tu-delft-and-klm-collaborate-on-sustainable-aviation-present-flying\-scale-model-flying-v/.

[24] W.J. Jung, N. Mangiavacchi, and R. Akhavan. Suppression of turbulence in wall-bounded flows by high-frequency spanwise oscillations. *Physics of Fluids A: Fluid Dynamics*, 4(8):1065–1607, 1992. doi: 10.1063/1.858381.

[25] K. Kempaiah. *Spanwise wall oscillation as a drag reduction technique*. MSc thesis, Delft University of Technology, 2019.

[26] K. U. Kempaiah, F. Scarano, G. E. Elsinga, van Oudheusden B. W., and L. Bermel. 3-dimensional particle image velocimetry based evaluation of turbulent skin-friction reduction by spanwise wall oscillation. *Physics of Fluids*, To be published, 2020.

[27] S. J. Kline, W. C. Reynolds, Schraub F. A., and P. W. Runstadler. The structure of turbulent boundary layers. *Journal of Fluid Mechanics*, 30(4):741–773, 1967. doi: 10.1017/S0022112067001740.

[28] S. Klumpp, M. Meinke, and W. Schröder. Friction drag variation via spanwise transversal surface waves. *Flow Turbulence Combust*, 87(1):33–53, 2011. doi: 10.1007/s10494-011-9326-3.

[29] S. R. Koh, P. Meysonnat, V. Statnikov, M Meinke, and W. Schröder. Dependence of turbulent wall-shear stress on the amplitude of spanwise transversal surface waves. *Computers and Fluids*, 119:261–275, 2015. doi: http://dx.doi.org/10.1016/j.compfluid.2015.06.021.

[30] V. I. Kornilov and A. V. Boiko. Towards improving the efficiency of blowing through a permeable wall and prospects of its use for a flow control. *AIP Conference Proceedings*, 1770:040006, 2016. doi: https://doi.org/10.1063/1.4964075.

[31] F. Laadhari, L. Skandaji, and R. Morel. Turbulence reduction in a boundary layer by a local spanwise oscillating surface. *Physics of Fluids*, 6(10):3218–3220, 1994. doi: https://doi.org/10.1063/1.868052.

[32] LaVision. 3d calibration plate, 2019. URL https://www.Lavision.de.

[33] C Liu, Y. Yan, and P. Lu. Physics of turbulence generation and sustenance in a boundary layer. *Computers and Fluids*, 102:353–384, 2014. doi: 10.1016/j.compfluid.2014.06.032.

[34] T. B. Lynn, D. W. Bechert, and D. A. Gerich. Direct drag measurements in a turbulent flat-plate boundary layer with turbulence manipulators. *Experiments in Fluids*, 19(6):405–416, 1995. doi: 10.1007/BF00190258.

[35] J.-P. Marec. *Aerodynamic drag reduction technologies*. Springer, 2000.

[36] F.J.W.A. Martins, J.M. Foucaut, M. Stanislas, and L. F. A. Azevedo. Characterization of near-wall structures in the log-region of a turbulent boundary layer by means of conditional statistics of tomographic piv data. *Experimental Thermal and Fluid Science*, 105:191 – 205, 2019. doi: 10.1016/j.expthermflusci.2019.03.020.

[37] S. Masatoshi and H. Naomichi. Turbulent boundary layers with injection and suction through a slit. *Bulleting of JSME*, 28(239):807–814, 1985.

[38] M. Novara, K. J. Batenburg, and F. Scarano. Motion tracking-enhanced mart for tomographic piv. *Measurement Science and Technology*, 21(3):035401, 2010. doi: 10.1088/0957-0233/21/3/035401.

[39] B.-G. Paik, Y.-S. Pyun, K.-Y. Kim, C.-M. Jung, and C.-G. Kim. Study on the micro-dimpled surface in terms of drag performance. *Experimental Thermal and Fluid Science*, 68:247–256, 2015. doi: 10.1016/j.expthermflusci.2015.04.021.

[40] S-H. Park, I. Lee, and H. J. Sung. Effect of local forcing on a turbulent boundary layer. *Experiments in Fluids*, 31(4):384–393, 2001. doi: 10.1007/s00348-003-0604-2.

[41] PLautridou. Find clusteres, 2016. URL https://www.mathworks.com/matlabcentral/fileexchange/57669-find-clusters.

[42] M. Qaudrio, P. Ricco, and C. Viotti. Streamwise-travelling waves of spanwise wall velocity for turbulent drag reduction. *Journal of Fluid Mechanics*, 627:161–178, 2009. doi: 10.1017/S0022112009006077.

[43] M. Raffel, C.E. Willert, F. Scarano, C. J. Kähler, S. T. Wereley, and J. Kompenhans. *Particle Image Velocimetry*. Springer, 2018.

[44] M. Reggente. *Statistical Gas Distribution Modelling for Mobile Robot Applications*. PhD dissertation, Örebro University, 2014.

[45] J. Reneaux. Overview on drag reduction technologies for civil transport aircraft. *European Congress on Computational Methods in Applied Sciences and Engineering*, 18p, 2004.

[46] P. Ricco and W. Shengli. On the effects of lateral wall oscillations on a turbulent boundary layer. *Experimental and Fluid Science*, 29(1):41–52, 2004. doi: 10.1016/j.expthermflusci.2004.01.010.

[47] S. Robinson. Coherent motions in the turbulent boundary layer. *Annual Review of Fluid Mechanics*, 23(1):601–639, 1991. doi: 10.1146/annurev.fl.23.010191.003125.

[48] D. Roggenkamp, W. Jessen, W. Li, M. Klaas, and W. Schröder. Experimental investigation of turbulent boundary layers over transversal moving surfaces. *CEAS Aeronaut Journal*, 6(3):471–484, 2015. doi: 10.1007/s13272-015-0155-2.

[49] A. Sahlin, Johansson A. V., and P. H. Alfredsson. The possibility of drag reduction by outer layer manipulators in turbulent boundary layers. *Phsysics of Fluids*, 31(10):2814–2820, 1988. doi: 10.1063/1.866989.

[50] F. Scarano and C. Poelma. Three-dimensional vorticity patterns of cylinder wakes. *Experiments in Fluids*, 47(1):69–83, 2009. doi: 10.10007//s00348-009-0629-2.

[51] C.R. Smith. A synthesized model of the near-wall behavior in turbulent boundary layers. *Proceedings of Eighth symposium on turbulence*, 1984.

[52] C.R. Smith and S.P. Metzler. The characteristics of low-speed streaks in the near-wall region of a turbulent boundary layer. *Journal of Fluid Mechanics*, 129:27–54, 1983. doi: 10.1017/S0022112083000634.

[53] Stanford University. Chapter 9 - visocus flow along a wall, 2020. URL https://web.stanford.edu/~cantwell/AA200_Course_Material/Ch09_Viscous_Flow_Along_a_Wall.pdf.

[54] V. Stenzel, Y. Wilke, and W. Hage. Drag-reducing paints for reduction of fuel consumption in aviation and shipping. *Progress in Organic Coatings*, 70(4):224–229, 2011. doi: 10.1017/jfm.2011.219.

[55] K. M. Swift. *An experimental analysis of the laminar separation bubble at low Reynolds numbers*. MSc thesis, University of Tennessee, 2009.

[56] The World Bank. Air transport, freight, 2019. URL https://data.worldbank.org/indicator/IS.AIR.GOOD.MT.K1?end=2018&start=1970&view=chart.

[57] The World Bank. Air transport, passengers carried, 2019. URL https://data.worldbank.org/indicator/IS.AIR.PSGR?end=2018&start=1970&view=chart.

[58] T. Theodorsen. Mechanism of turbulence. *Proceedings of the Midwestern Conference on Fluid Mechanics*, 1952.

[59] S. Tokgoz, G. E. Elsinga, R. Delfos, and J. Westerweel. Spatial resolution and dissipation rate estimation in taylor-couette flow for tomographic piv. *Experiments in Fluids*, 53(3):561–583, 2012. doi: DOI10.1007/s00348-012-1311-7.

[60] TU Delft. Flow stability & flow control, 2020. URL https://www.tudelft.nl/en/ae/organisation/departments/aerodynamics-wind-energy-flight-performance-and-propulsion/aerodynamics/research/flow-stability-flow-control/.

[61] TU Delft. W-tunnel, 2020. URL https://www.tudelft.nl/lr/organisatie/afdelingen/aerodynamics-wind-energy-flight-performance-and-propulsion/facilities/low-speed-wind-tunnels/w-tunnel/.

[62] Utah State University. Supersonic wings with skin friction: A primer on boundary layers and skin friction, 2019. URL http://mae-nas.eng.usu.edu/MAE_5420_Web/section8/section8.1.pdf.

[63] B. van Oudheusden. Ae 4120: Viscous flows slides. *TU Delft*, 2019.

[64] L.L.M. Veldhuis. Ae 4130: Aircraft aerodynamics. *TU Delft*, 2018.

[65] West. Thomas edison: Champion of renewable energy, 2000. URL https://www.thoughtco.com/thomas-edison-champion-of-renewable-energy-1204180.

[66] R. D. Whalley and K-S. Choi. Turbulent boundary-layer control with plasma spanwise travelling waves. *Experiments in Fluids*, 55(8):1796, 2014. doi: 10.1007/s00348-014-1796-3.

[67] B. Wieneke. Volume self-calibration for 3d particle image velocimetry. *Experiments in Fluids*, 45(4):549–556, 2008. doi: 10.1007/s0038-008-0521-5.

[68] K. Yousefi and R. Saleh. Three-dimensional suction flow control and suction jet length optimization of naca 0012 wing. *Meccanica*, 50(6):1481–1494, 2015.

[69] J. Zhou, C.D. Meinahrd, S. Balachandar, and R. J. Adrian. Formation of coherent hairpin packets in wall turbulence. *Advances in Fluid Mechanics*, 15:109–134, 1997.